INSTITUT DE FÍSICA
D'ALTES ENERGIES

UNIVERSITAT AUTÒNOMA
DE BARCELONA

Search for the Production of Gluinos and Squarks with the CDF II Experiment at the Tevatron Collider

Ph.D. Dissertation

Gianluca De Lorenzo
IFAE
Edifici Cn, UAB
08193 Bellaterra (Barcelona), Spain
gdl@ifae.es

May 19, 2010

supervised by:

Mario Martinez-Perez
ICREA Research Professor
IFAE & UAB
Edifici Cn, UAB
08193 Bellaterra (Barcelona), Spain
mmp@ifae.es

Tomé la estrella de la noche fría
y suavemente
la eché sobre las aguas.

Y no me sorprendió
que se alejara
como un pez insoluble
moviendo
en la noche del río
su cuerpo de diamante.

Contents

Introduction

According to the theory of Supersymmetry, squarks and gluinos are the supersymmetric partners of the Standard Model quarks and gluons. In the phenomenological framework assumed for this Thesis, squarks and gluinos are produced in pairs and ultimately decay into multiple partons and neutralinos, the lightest of the supersymmetric particles. The neutral and weakly interacting neutralinos escape the detector undetected. As a result, the final state is characterized by multiple jets of hadrons and large missing transverse energy.

This Thesis reports on two searches for the production of gluinos and squarks in $p\bar{p}$ collisions at a center of mass energy of $\sqrt{s} = 1.96$ GeV with the CDF Run II experiment at the Tevatron collider. The first of the two analyses is an inclusive search for gluinos and squarks while the second one is dedicated to the search for direct pair production of sbottom squarks. The Thesis is organized as follows: Chapter 1 presents a brief introduction to Supersymmetry; Chapter 2 describes the Tevatron collider and the CDF II experiment; Chapter 3 and 4 are dedicated to the inclusive search for squarks and gluinos, and the exclusive search for sbottom squarks, respectively. Finally, Chapter 5 is devoted to conclusions.

The results of this Thesis have led to the following publications:

- *Inclusive Search for Squark and Gluino Production in $p\bar{p}$ Collisions at $\sqrt{s} = 1.96$ TeV*, T. Aaltonen et al. (CDF Collaboration), Phys. Rev. Lett. 102, 121801 (2009).
- *Search for the Production of Scalar Bottom Quarks in $p\bar{p}$ Collisions at $\sqrt{s} = 1.96$ TeV*. T. Aaltonen et al. (CDF Collaboration), Submitted to Phys. Rev. Lett. (May 2010) [hep-ex/0041311].

Chapter 1

Theoretical Overview

The Standard Model (SM) is a gauge theory describing the electroweak and strong interactions in a common quantum field structure. The SM, complemented by massive neutrinos, provides a remarkably successful description of all known phenomena at the current energy frontier. Nevertheless, the SM presents some limitations and needs to be extended to describe physics at arbitrarily high energies. Probably the most famous among all the proposed extensions of the SM is the theory of Supersymmetry (SUSY) [1]. In particular, SUSY can provide an elegant solution to one of the main theoretical difficulties of the SM, known as *hierarchy problem* [2]. The introduction of SUSY has also other benefits. For example, it is a convenient framework for the unification of forces and it includes a dark matter candidate.

In the following Sections, after a brief illustration of the hierarchy problem, the basic properties of SUSY are presented, followed by a description of the minimal viable supersymmetric extension of the SM: the MSSM. The phenomenological models of interest for this Thesis are discussed in dedicated Sections. Finally, the end of the Chapter is devoted to details on the Monte Carlo (MC) simulation of complex final states at hadron colliders.

1.1 The Hierarchy Problem

The SM gauge bosons acquire their masses via the spontaneous electroweak symmetry breaking, known as the Higgs mechanism [3]. It implies the introduction of a scalar potential that is added to the electroweak Lagrangian to generate the vector-boson (and fermion) masses in a gauge invariant way. A remnant scalar field, the Higgs boson H_{SM}, becomes part of the physical spectrum. Direct searches at LEP [4] led to the conclusion that it must be heavier than 114.4 GeV/c^2 at 95% confidence level (CL). From precision electroweak measurements [5], the Higgs mass is expected to be lower than 182 GeV/c^2 at 95% CL. The latest combined results from Tevatron [6] further reduced the available range excluding SM Higgs masses between 160 and 170 GeV at 95% CL.

The new Large Hadron Collider (LHC) at CERN is believed to have the best chances to find the Higgs in the next years. However, even in the case of a discovery, the finding of the Higgs particle will hardly be the final word. In fact, the Higgs mechanism, though providing a theoretical framework to include massive gauge bosons, originates the so called hierarchy problem. In the SM, there is no mechanism to prevent scalar particles from acquiring large masses through radiative corrections. Therefore, the Higgs mass m_H^2 receives enormous quan-

tum corrections from every particle which couples to the Higgs field (see one-loop diagrams in Figure 1.1):

$$m^2_{H_{SM}} = (m^2_H)_0 + \Delta M^2_H \tag{1.1}$$

where $(m^2_H)_0$ is the bare Higgs mass and ΔM^2_H is the correction given by terms like

$$\Delta M^2_H = -\frac{\lambda^2_f}{16\pi^2}\left[2\Lambda^2 + \mathcal{O}\left(m^2_f \ln\left(\frac{\Lambda}{m_f}\right)\right)\right] \tag{1.2}$$

where λ_f is the Yukawa coupling of a fermion f and Λ is an energy cutoff which is interpreted as the energy scale up to which SM is valid. If SM needs to describe nature until the Planck scale, then the quantum correction ΔM^2_H is about 30 orders of magnitude larger than the bare Higgs mass square. A cancellation of these corrections at all orders would call for an incredible *fine tuning* which seems very unlikely [7]. In a model with spontaneous electroweak symmetry breaking, the problem affects not only the Higgs mass but also all the particles whose masses are obtained through this mechanism: Ws, Zs, quarks, and charged leptons.

1.2 Supersymmetry as a Solution to the Hierarchy Problem

SUSY is a symmetry relating bosons and fermions via the anti-commuting spinor Q that generates the transformation of fermions into bosons and vice versa:

$$Q|Boson\rangle = |Fermion\rangle \qquad Q|Fermion\rangle = |Boson\rangle. \tag{1.3}$$

Therefore, every fermion f has a scalar partner S. Both fermions and bosons couple to the Higgs contributing with similar mass corrections. While fermions contribute with terms like the one in Equation 1.2, the bosonic correction is:

$$\Delta M^2_H = \frac{\lambda^2_S}{16\pi^2}\left[2\Lambda^2 + \mathcal{O}\left(m^2_S \ln\left(\frac{\Lambda}{m_S}\right)\right)\right] \tag{1.4}$$

with $\lambda_f = \lambda_S$ and opposite sign due to the the Fermi statistics. In this way, all the mass corrections cancel each other out, with remaining terms of the form:

$$\Delta M^2_H = \frac{\lambda^2}{16\pi^2}\left|m^2_S - m^2_f\right| \tag{1.5}$$

plus some negligible contributions. This solves the hierarchy problem with the price of doubling the number of particles of the SM. The energy scale Λ where the SM is no longer valid and should be substituted by its supersymmetric extension can be determined by considering that the remaining corrections in Equation 1.5 have to be smaller than $m_{H_{SM}}$ to avoid an *unnatural* fine tuning [8]:

$$\Lambda \sim \left|m^2_S - m^2_f\right| \lesssim 1 \ \text{TeV}^2 \ . \tag{1.6}$$

In any case, this is only a qualitative argument and does not help predicting exactly at which energy new particles should appear.

1.3 The Minimal Supersymmetric Standard Model

Similarly to the SM construction, conceived to be the minimal group viable to explain the electroweak sector, the MSSM [9] is the minimal viable supersymmetric extension of the SM itself. As for the SM, the MSSM is also based on the $\mathrm{SU}(3)_C \otimes \mathrm{SU}(2)_L \otimes \mathrm{U}(1)_Y$ gauge symmetry group, where C denotes color, L chirality, and Y hypercharge. Every group is characterized by the correspondent coupling constant: g_S (related with α_s) for the strong interactions, g (related with the Fermi constant G_F) for the weak interactions, and g' (related with the electron charge e) for the electromagnetic interactions.

As already mentioned, the MSSM doubles the number of SM particles introducing, for each of them, a superpartner which differs by half a unit of spin. Superpartners are conveniently labeled in close correspondence to the notation for bosons and fermions used in the SM, with the same letters of their partners and a tilde ($\tilde{}$) over them. Superfields have a *hat* ($\hat{}$) instead. In addition, the bosonic partners of the fermions are named starting with an extra s (e.g. the squark sbottom is the superpartner of the quark bottom) and the names of the fermionic partners of the bosons end with the suffix *ino* (e.g. the gluino is the superpartner of the gluon).

For simplicity and to avoid unnecessary repetitions, consider the case of only one generation of quarks, leptons, and their superpartners. One can define $\hat{Q}$ as the superfield containing an $\mathrm{SU}(2)_L$ doublet of quarks:

$$Q = \begin{pmatrix} u_L \\ d_L \end{pmatrix} \tag{1.7}$$

and their scalar partners which are also in an $\mathrm{SU}(2)_L$ doublet,

$$\tilde{Q} = \begin{pmatrix} \tilde{u}_L \\ \tilde{d}_L \end{pmatrix} \tag{1.8}$$

In an analogous form, the superfield $\hat{U}^c$ ($\hat{D}^c$) contains the right-handed up (down) anti-quark, $\bar{u}_R$ ($\bar{d}_R$), and its scalar partner, $\tilde{u}^*_R$ ($\tilde{d}^*_R$). Following the same pattern, leptons are contained in the $SU(2)_L$ doublet superfield $\hat{L}$ which contains the left-handed fermions,

$$L = \begin{pmatrix} \nu_L \\ e_L \end{pmatrix} \tag{1.9}$$

and their scalar partners,

$$\tilde{L} = \begin{pmatrix} \tilde{\nu}_L \\ \tilde{e}_L \end{pmatrix} \quad . \tag{1.10}$$

Finally, the superfield $\hat{E}^c$ contains the right-handed anti-electron, $\bar{e}_R$, and its scalar partner, $\tilde{e}^*_R$. Similarly, for every gauge boson it exists a Majorana fermion (gaugino). $\hat{G}^a$ is defined as a superfield that contains all the gluons, g^a, and their fermion partners the gluinos, $\tilde{g}^a$; $\hat{W}_i$ contains the $SU(2)_L$ gauge bosons, W_i, and their fermion partners, $\tilde{\omega}_i$ (winos); and $\hat{B}$ contains the $U(1)$ gauge field, B, and its fermion partner, $\tilde{B}$ (bino).

In the MSSM, the Higgs sector is enlarged to avoid triangle gauge anomalies [10]. Gauge theories cannot have anomalies and this is simply achieved by requiring that the sum of all fermion charges vanishes. The Higgs scalar doublet acquires a SUSY partner which is an $\mathrm{SU}(2)_L$ doublet of Majorana fermion fields, $\tilde{h}_1$ (Higgsinos), which will contribute to the triangle $\mathrm{SU}(2)_L$ and $\mathrm{U}(1)_Y$ gauge anomalies. Since fermions in SM have exactly the right quantum

Names		**2HDM particle**		**SUSY partner**		$SU(3)_C$, $SU(2)_L$, $U(1)_Y$
squarks, quarks (x 3 families)	$\hat{Q}$	$(u_L\ d_L)$	$\frac{1}{2}$	$(\tilde{u}_L\ \tilde{d}_L)$	0	$(3, 2, \frac{1}{3})$
	$\hat{U}$	$u_R^\dagger$	$\frac{1}{2}$	$\tilde{u}_R^*$	0	$(\bar{3}, 1, -\frac{4}{3})$
	$\hat{D}$	$d_R^\dagger$	$\frac{1}{2}$	$\tilde{d}_R^*$	0	$(\bar{3}, 1, \frac{2}{3})$
sleptons, leptons (x 3 families)	$\hat{L}$	$(\nu\ e_L)$	$\frac{1}{2}$	$(\tilde{\nu}\ \tilde{e}_L)$	0	$(1, 2, -1)$
	$\hat{E}$	$e_R^\dagger$	$\frac{1}{2}$	$\tilde{e}_R^*$	0	$(1, 1, 2)$
Electroweak bosons	$\hat{W}$	$W^1\ W^2\ W^3$	1	$\tilde{W}^1\ \tilde{W}^2\ \tilde{W}^3$	$\frac{1}{2}$	(1, 3, 0)
	$\hat{B}$	B	1	$\tilde{B}$	$\frac{1}{2}$	(1, 1, 0)
Strong bosons	$\hat{G}_a$	g_a	1	$\tilde{g}_a$	$\frac{1}{2}$	(8, 1, 0)
Higgs, Higgsinos	$\hat{H}_u$	$(H_u^+\ H_u^0)$	0	$(\tilde{H}_u^+\ \tilde{H}_u^0)$	$\frac{1}{2}$	$(1, 2, 1)$
	$\hat{H}_d$	$(H_d^0\ H_d^-)$	0	$(\tilde{H}_d^0\ \tilde{H}_d^-)$	$\frac{1}{2}$	$(1, 2, -1)$

Table 1.1: superfields and particle content of the MSSM. Symbols for each of the chiral supermultiplets as a whole are indicated in the second column.

numbers to cancel these anomalies, it follows that the contribution from the fermionic partner of the Higgs doublet remains uncancelled. The easiest solution is to require a second Higgs doublet with precisely the opposite $\mathrm{U}(1)_Y$ quantum number with respect to the first Higgs doublet. Furthermore, the SM Higgs doublet (and its complex conjugate) can couple to the $T_3 = +\frac{1}{2}$ ($T_3 = -\frac{1}{2}$) fermions and give mass to all the spectrum of fermions. Since in a supersymmetric theory any doublet can give mass either to a $T_3 = +\frac{1}{2}$ or a $T_3 = -\frac{1}{2}$ fermion but not to both, two Higgs doublets are needed in order to generate both up-like and down-like quark masses. As result, one could think of the SM becoming a two Higgs doublet model (2HDM) [11] prior to introduce the supersymmetric sector. In Table 1.1 the spectrum of the MSSM fields is summarized. With two SU(2) doublets, the theory has eight real scalar fields and three massless gauge bosons, which accounts for fourteen degrees of freedom.

If supersymmetry was an exact symmetry, particles and their supersymmetric partners would have equal masses and the SUSY gauge bosons would be massless. Since this is not the case in nature, at low energies supersymmetry must be a broken symmetry. After SUSY breaking, the three gauge bosons acquire masses (nine degrees of freedom), which means that there should exist five spin-zero Higgs fields in the spectrum: three neutral scalars (h, H, A) and two charged pairs (H^+, H^-).
The parameters of the supersymmetry-conserving sector consist of:

- Gauge couplings: g_s, g, and g', corresponding to the Standard Model gauge group $\mathrm{SU}(3)_C \otimes \mathrm{SU}(2)_L \otimes \mathrm{U}(1)_\mathrm{Y}$, respectively.
- Higgs mass parameter, μ.
- Higgs-fermion Yukawa coupling constants: λ_u, λ_d, and λ_e, corresponding to the coupling of quarks or leptons and their superpartners to the Higgs bosons and Higgsinos.

The supersymmetry-breaking sector contains the following set of parameters:

- Gaugino Majorana masses M_3, M_2, and M_1, associated with the $\mathrm{SU}(3)_C$, $\mathrm{SU}(2)_L$, and $\mathrm{U}(1)_\mathrm{Y}$ subgroups, respectively. These masses may be connected in some cases as will be seen later.

2HDM particle		**spin**	**SUSY particle**		**spin**
quarks:	q	$\frac{1}{2}$	squarks:	$\tilde{q}_1,\ \tilde{q}_2$	0
leptons:	l	$\frac{1}{2}$	sleptons:	$\tilde{l}_1,\ \tilde{l}_2$	0
gluons:	g_a	1	gluinos:	$\tilde{g}_a$	$\frac{1}{2}$
gauge bosons:	$W^{\pm},\ Z^0,\ \gamma$	1	neutralinos:	$\tilde{\chi}_1^0,\ \tilde{\chi}_2^0,\ \tilde{\chi}_3^0,\ \tilde{\chi}_4^0$	$\frac{1}{2}$
Higgs bosons:	$h^0,\ H^0,\ A^0,\ H^{\pm}$	0	charginos:	$\tilde{\chi}_1^{\pm},\ \tilde{\chi}_2^{\pm}$	$\frac{1}{2}$

Table 1.2: particle content of the MSSM.

- Five scalar squared-mass parameters for the squarks and sleptons: $M_{\tilde{Q}}^2$, $M_{\tilde{U}}^2$, $M_{\tilde{D}}^2$, $M_{\tilde{L}}^2$, and $M_{\tilde{E}}^2$, corresponding to the five electroweak gauge multiplets.

- Trilinear interaction terms of the form Higgs-squark-squark and Higgs-slepton-slepton, with coefficients A_u, A_d, and A_e.

- Three scalar Higgs squared-mass parameters, two of which (m_1^2 and m_2^2) contribute to the diagonal Higgs squared-masses and a third which corresponds to the off-diagonal terms $m_{12}^2 \equiv \mu B$. These three parameters can be re-expressed in terms of the two Higgs vacuum expectation values ($v_d = \langle H_d^0 \rangle$ and $v_u = \langle H_u^0 \rangle$)[1], usually taken through the ratio

$$\tan\beta \equiv \frac{v_u}{v_d}\ , \tag{1.11}$$

  and one physical Higgs mass[2].

The gluino is the color octet Majorana (there is no distinct antigluon) fermion partner of the gluon. It has 16 degrees of freedom since there are 8 massless gluons (2 spin degrees of freedom, each). The supersymmetric partners of the electroweak gauge and Higgs bosons (gauginos and Higgsinos) can mix. As a result, the physical mass eigenstates are model-dependent linear combinations of these states, called *charginos* and *neutralinos*, which are obtained by diagonalising the corresponding mass matrices. There are two charginos ($\tilde{\chi}_i^{\pm}$) and four neutralinos ($\tilde{\chi}_i^0$), which are by convention ordered in masses ($\tilde{\chi}_1^{\pm}$ is the lowest chargino and $\tilde{\chi}_1^0$ is the lowest neutralino). Depending whether the chargino or neutralino eigenstate approximates a particular gaugino or Higgsino state, they can become more photino-like, bino-like, and so on, and result in strikingly different phenomenology.

The supersymmetric partners of the quarks and leptons are spin-zero bosons, squarks, and sleptons whose mass eigenstates (denoted by the indices 1,2) arise as a result of the mixing of their left- and right-handed components. This mixing is proportional to the mass of the SM partner, quark or lepton, and to $\tan\beta$, and it can lead to an important splitting in the mass spectrum of heavy squarks, specially at large $\tan\beta$, while the first two families can be always considered degenerate in mass with good approximation. All physical particles of the MSSM are given in Table 1.2.

[1]Notation v_u (v_d) is used to distinguish vacuum expectation values of the Higgs field which couples exclusively to up-type (down-type) quarks.

[2]Note that $v_d^2 + v_u^2 = 4M_W^2/g^2 = (246\ \mathrm{GeV/c^2})^2$ is fixed by the W mass and the gauge coupling, but $\tan\beta$ is a free parameter of the model.

1.3.1 MSSM Lagrangian and R-parity

The MSSM Lagrangian $\mathcal{L}_{\text{MSSM}}$ is constructed using the already defined particle content and by analogy with the $\mathcal{L}_{\text{SM}}$. Following a similar notation as in the SM, the kinetic term of the Lagrangian can be written as:

$$\begin{aligned}\mathcal{L}_{KE} = &\sum_i \left\{ (D_\mu S_i)^\dagger (D^\mu S_i) + \frac{i}{2}\bar{\psi}_i \gamma^\mu D_\mu \psi_i \right\} \\ &+ \sum_A \left\{ -\frac{1}{4} F^A_{\mu\nu} F^{\mu\nu A} + \frac{i}{2}\bar{\lambda}_A D \lambda_A \right\} \ .\end{aligned} \tag{1.12}$$

Here, S_i (ψ_i) is the scalar (fermion) component of the i^{th} chiral superfield, D is the $SU(3) \times SU(2)_L \times U(1)$ gauge invariant derivative, $F^A_{\mu\nu}$ is the Yang-Mills gauge field, and λ_A is the gaugino superpartner of the corresponding gauge boson. It is worth noticing that the sum $\sum_i$ runs over all fermion fields of the SM, their scalar partners, and the 2 Higgs doublets with their fermion partners. On the other hand, $\sum_A$ is over the $SU(3)_c$, $SU(2)_L$, and $U(1)_Y$ gauge fields, and their fermion partners, the gauginos.

The interactions between bosons and fermions are completely determined by the gauge symmetries and by the supersymmetry:

$$\begin{aligned}\mathcal{L}_{int} = &-\sqrt{2}\sum_{i,A} g_A \left[S_i^* T^A \bar{\psi}_{iL} \lambda_A + \text{h.c.} \right] \\ &- \frac{1}{2}\sum_A \left(\sum_i g_A S_i^* T^A S_i \right)^2 \qquad ,\end{aligned} \tag{1.13}$$

where $\psi_L \equiv \frac{1}{2}(1-\gamma_5)\,\psi$, T^A is the matrix of the group generators, and g_A the gauge coupling constants. It can be seen that there are no adjustable parameters, hence, all interaction strengths are completely fixed in terms of SM coupling constants.

Once the superfields and the gauge symmetries are chosen, the only freedom in constructing $\mathcal{L}_{MSSM}$ is contained in a function called *superpotential*, $\mathcal{W}$. This is an analytic form of the chiral superfields, $\hat{S}$, that has the form:

$$\mathcal{W} = \epsilon_{ij}\mu \hat{H}_u^i \hat{H}_d^j + \epsilon_{ij}\left[\lambda_L \hat{H}_d^i \bar{\hat{L}}^j \bar{\hat{E}} + \lambda_D \hat{H}_d^i \hat{Q} \bar{\hat{D}} + \lambda_U \hat{H}_u^j \hat{Q}^i \bar{\hat{U}} \right] + W_{RP} \tag{1.14}$$

where i and j are $SU(2)_L$ doublet indices and $\epsilon_{ij} = -\epsilon ji$ (with $\epsilon_{12} = 1$) contracts the $SU(2)_L$ doublet fields. No derivative interactions are allowed in order that $\mathcal{W}$ be an analytical function. The term $\mu \hat{H}_u^i \hat{H}_d^j$ gives mass terms for the Higgs bosons and so μ is often called the Higgs mass parameter. The terms in the square brackets proportional to λ_L, λ_D, and λ_U give the usual Yukawa interactions of the fermions with the Higgs bosons. Hence, unlike the SM case, these coefficients are determined in terms of the fermion masses and the vacuum expectation values of the neutral members of the scalar components, and are not arbitrary couplings.

In the most general superpotential one can add more terms which are grouped under W_{RP} in Equation 1.14. These terms are of the form:

$$W_{RP} = \lambda_{\alpha\beta\gamma} \hat{L}^\alpha \hat{L}^\beta \bar{\hat{E}}^\gamma + \lambda'_{\alpha\beta\gamma} \hat{L}^\alpha \hat{Q}^\beta \bar{\hat{D}}^\gamma + \lambda''_{\alpha\beta\gamma} \bar{\hat{U}}^\alpha \bar{\hat{D}}^\beta \bar{\hat{D}}^\gamma + \mu' \hat{L}\hat{H} \tag{1.15}$$

where the indices α, β, and γ label the 3 generations of quarks and leptons. These terms constitute a problem in the sense that the first two contribute to lepton number violation interactions and the third one to baryon number violation interactions[3]. The combination of lepton and baryon violation terms can contribute to the proton decay at tree level through the exchange of the scalar partner of the down quark. Since this process is experimentally restricted [13][14] it put into question the validity of the model. It's certainly licit to assume that the parameters are small enough to avoid experimental limits, but this solution would imply the introduction of an artificial tuning. A more elegant solution is to introduce a new symmetry called R-parity (R_p) [15]. R_p is a multiplicative quantum number defined as:

$$R_p = (-1)^{3(B-L)+2s} \ , \tag{1.16}$$

where B and L are the baryon and lepton quantum numbers and s is the spin of the particle. Following this definition all SM particles have $R_p = +1$ while their SUSY partners have $R_p = -1$. The assumption of such a symmetry prevents lepton and baryon number violating terms but has also dramatic phenomenological consequences: there can be no mixing between the $R_p = -1$ sparticles and the $R_p = 1$ particles. SUSY particles can only be pair-produced in the collisions of SM particles and undergo a chain of decays until the lightest SUSY particle (LSP) is produced. Then, this LSP cannot decay further and constitutes a cold dark matter candidate [16][17].

At this point, the MSSM Lagrangian does not provide mass terms for all the particles (fermions, scalars, gauge fields), and extra SUSY breaking terms are grouped in the so-called *soft Lagrangian*:

$$\mathcal{L} = \mathcal{L}_{\text{MSSM}} + \mathcal{L}_{\text{soft}}. \tag{1.17}$$

where

$$\begin{aligned} -\mathcal{L}_{soft} = & \frac{1}{2}\left[M_3\hat{g}\hat{g} + M_2\hat{W}\hat{W} + M_1\hat{B}\hat{B}\right] \\ & + \epsilon_{\alpha\beta}\left[-bH_d^{\alpha}H_u^{\beta} - H_u^{\alpha}\hat{Q}_i^{\beta}\hat{A}_{u_{ij}}\bar{\hat{U}}_j + H_d^{\alpha}\hat{Q}_i^{\beta}\hat{A}_{d_{ij}}\bar{\hat{D}}_j + H_d^{\alpha}\hat{L}_i^{\beta}\hat{A}_{e_{ij}}\bar{\hat{E}}_j + \text{h.}c.\right] \\ & + m_{H_d}^2|H_d|^2 + m_{H_u}^2|H_u|^2 + \hat{Q}_i^{\alpha}m_{Q_{ij}}^2\hat{Q}_j^{\alpha *} \\ & + \hat{L}_i^{\alpha}m_{L_{ij}}^2\hat{L}_j^{\alpha *} + \bar{\hat{U}}_i^{*}m_{U_{ij}}^2\bar{\hat{U}}_j + \bar{\hat{D}}_i^{*}m_{D_{ij}}^2\bar{\hat{D}}_j + \bar{\hat{E}}_i^{*}m_{E_{ij}}^2\bar{\hat{E}}_j \ , \end{aligned} \tag{1.18}$$

where i and j are the $SU(2)_L$ doublet indices. How supersymmetry breaking is transmitted to the superpartners is encoded in the parameters of $\mathcal{L}_{soft}$. The Lagrangian in Equation 1.18 contains first order terms only, it has arbitrary masses for the scalars and gauginos and also arbitrary bi-linear and trilinear mixing terms. The scalar and gaugino mass terms have the desired effect of breaking the mass degeneracy between the particles and their SUSY partners. The trilinear A terms affect primarily the particles of the third generation. The μB term mixes the scalar components of the two Higgs doublets. In the most general case, all of the mass and interaction terms of Equation (1.18) are matrices involving all three generators although the origin of all these terms is left unspecified. All of the quantities in $\mathcal{L}_{soft}$ receive radiative corrections and thus are scale-dependent, satisfying known Renormalization Group Equations (RGEs).

[3]The fourth term can be ignored since one can implement a rotation in the lepton field $\hat{L}$ such that this term vanishes [12].

From a phenomenological point of view, the MSSM is a very simple framework with few extra assumptions with respect to the SM (the presence of supersymmetric particles, the R_p, the gauge and Poincaré invariance), but it introduces a large number of free input parameters. The MSSM includes at least 105 new degrees of freedom that added to the 19 of the SM increases the total number of free parameters to 124. Although only a subset of these parameters is relevant in the characterization of most of the physical processes, and some phenomenological constraints can be usually applied, the number is too large for any practical purpose. However, unlike in the SM case, now there is the possibility to establish a top-down approach by which the MSSM parameters are predicted within the context of an underlying theory, often as functions of fewer basic parameters. The fundamental question is how the spontaneous supersymmetry breaking encoded in the $\mathcal{L}_{soft}$ arises in a more fundamental theory. Since this is not known, several models have been constructed, most of them making the assumption that the theory can be split into at least two sectors with no direct renormalizable couplings between them. The *observable* or *visible* sector contains the SM fields and their superpartners, while in the *hidden* sector the supersymmetry is spontaneously broken by a dynamical mechanism. Within this framework, SUSY breaking is communicated from the hidden sector where it originates to the observable sector via suppressed interactions involving a third set of fields: the *mediator* or *messenger* fields. The existence of a hidden sector constrains the fundamental scale of supersymmetry breaking μ_s to be hierarchically larger than the TeV scale [18]. Depending on the model this μ_s can be postulated to be at the Grand Unified Theory (GUT) scale $M_X \sim 10^{16}$ GeV/c^2, at the Majorana neutrino mass scale, or in the extra-dimensional braneworld. Therefore, different models account for specific mechanisms of how supersymmetry breaking is mediated between the hidden and observable sectors and involve specific energy scales at which the soft terms are generated. These values are then used to derive all the observables at the TeV scale, using the energy dependence of the $\mathcal{L}_{soft}$ parameters as dictated by their RGEs.

1.4 Constraining the MSSM: mSUGRA Model

The observation that the measured coupling constants tend to meet at a point when evolved to high energy scales inspired many SUSY GUT models. In these models, the value of the couplings at the GUT scale plays a central role [12]:

$$\sqrt{\frac{5}{3}} g_1(M_X) = g_2(M_X) = g_s(M_X) \equiv g^* \ . \tag{1.19}$$

Since gravitational interactions are shared by all the particles, it is quite natural to imagine gravity to be the only interaction shared by both the hidden and the observable sectors. Furthermore, at some point gravity must be present in a complete particle field theory. Here, supergravity would be responsible for promoting global supersymmetry to local supersymmetry. This is what inspired the mSUGRA model [19]. In this model, along with the coupling constants, the following set of assumptions emerges:

1. Common gaugino mass $m_{1/2}$: the gaugino mass terms, M_i, are assumed to unify:

$$M_i(M_X) \equiv m_{1/2} \ , \tag{1.20}$$

2. Common scalar mass m_0. The soft SUSY-breaking scalar mass terms contributing to the squark, slepton and Higgs boson masses are equal to m_0 at M_X:

$$\begin{aligned} m_{\hat{Q}^2}(M_X) &= m^2_{\tilde{u}}(M_X) = \cdots \\ &= m^2_{H_d}(M_X) = m^2_{H_u}(M_X) \equiv m_0^2 \ . \end{aligned} \tag{1.21}$$

3. Common trilinear scalar coupling A_0. The soft trilinear SUSY-breaking terms are all equal to A_0 at M_X,

$$A_t(M_X) = A_b(M_X) = A_\tau(M_X) = \cdots \equiv A_0 \ . \tag{1.22}$$

Through RGEs the gaugino masses in Equation 1.20 scale in the same way as the corresponding coupling constants:

$$M_i(M_W) = m_{1/2}\frac{g_i^2(M_W)}{g^{*2}} \ , \tag{1.23}$$

yielding,

$$\begin{aligned} M_2 &= \frac{g^2}{g_s^2}M_3 \approx 0.3 m_{\tilde{g}} \\ M_1 &= \frac{5}{3}\frac{g'^2}{g^2}M_2 = \frac{5}{3}\tan^2\theta_W M_2 \approx 0.5 M_2 \ , \end{aligned} \tag{1.24}$$

where every term is evaluated at M_W scale and $m_{\tilde{g}}$ is the gluino mass.

The gluino mass is therefore always the heaviest of the gaugino masses. Equation 1.20 and Equation 1.21, in conjunction with SUSY and the gauge structure, lead to the following expressions for the masses of the sfermions (except for the third generation) at the electroweak scale [20]:

$$\begin{aligned} m^2_{\tilde{f}_{L,R}} &= m_f^2 + m_0^2 + b_{\tilde{f}_{L,R}} m^2_{1/2} \\ &\quad \pm m_Z^2 \cos 2\beta \left[T_3^{\tilde{f}_{L,R}} - Q_{\tilde{f}_{L,R}} \sin^2\theta_W \right] \ , \end{aligned} \tag{1.25}$$

where $\tilde{f}_{L,R}$ is the corresponding left (right) sfermion, $T_3^{\tilde{f}_{L,R}}$ and $Q_{\tilde{f}_{L,R}}$ are the third component of the weak isospin and the electric charge of the corresponding fermion f, and the coefficients b are derived from the RGEs and can take different values. In particular, $b \approx 6$ for squarks, ≈ 0.5 for left sleptons and ≈ 0.15 for right sleptons. An approximate view of the running masses obtained via the RGEs can be seen in Figure 1.2.

Since the supersymmetry is broken via gravitational interaction, a new massless Goldstone particle (the Goldstino) need to be present. This new particle will be eaten by the gravitino (the spin 3/2 partner of the spin 2 graviton), such that it becomes massive, determining the SUSY breaking scale, μ_S:

$$m_{\tilde{G}} \sim \frac{\mu_S^2}{M_{Pl}} \ . \tag{1.26}$$

Therefore, in mSUGRA the hidden sector is postulated at the Planck mass and, in order to obtain the new SUSY masses at the desired TeV scale to prevent Higgs mass divergence and to obtain coupling unification at the GUT scale, the SUSY breaking scale (following Equation 1.26) should be around $10^{11} - 10^{12}$ GeV.

With the assumptions in Equations 1.20 - 1.22, the SUSY sector in mSUGRA is completely described by 5 input parameters at the GUT scale [21]: m_0, $m_{1/2}$, A_0, μ, and B, where μ is the Higgs mass parameter and B the Higgs mixing parameter. The requirement that the Z boson obtains its measured value when the parameters are evaluated at low energy can be used to restrict $|\mu B|$, leaving the sign of μ as a free parameter. In addition one can also change the B parameter for $\tan\beta$ and use the usual set of parameters for the model:

$$m_0,\ m_{1/2},\ A_0,\ \tan\beta,\ \mathrm{sign}(\mu)\ . \tag{1.27}$$

This model is a simplistic scenario that serves as a good benchmark model since it is extremely predictive with the entire low energy spectrum depending on just five input parameters. Of course, one needs to bear in mind that changing the input parameters at M_X (for example assuming non-universal scalar masses) changes the phenomenology at the weak scale and experimental analyses should be focused as much as possible on model independent approaches.

1.4.1 Squarks and Gluinos in mSUGRA

Squarks are the spin-0 boson superpartners of the left- and right-handed quarks. These particles are part of the supersymmetric QCD (SUSY-QCD) framework, which is based on the colored particles of the MSSM with their masses coming form a mixture of the chiral states, with different contributions defined by the set of RGEs that run in the mSUGRA framework. Squark mass parameters have a strong dependence on the common gaugino mass $M_{1/2}$ because of the color. For the first and second generation squarks, the left- and right-handed soft SUSY-breaking parameters at electroweak scale are given approximately by:

$$m^2_{\tilde{Q}_{1,2}} \approx m_0^2 + 6.3 m_{1/2}^2 \quad ; \quad m^2_{\bar{\tilde{u}}_{1,2}} \approx m^2_{\bar{\tilde{d}}_{1,2}} \approx m_0^2 + 5.8 m_{1/2}^2\ . \tag{1.28}$$

In general, squarks are heavier than the sleptons and the lightest neutralino and chargino because of the strong interactions. More concretely, the mass parameters of the first two generations are roughly degenerate while the third generation masses are typically reduced by a factor of up to 3. The concrete spectrum can vary depending on the tanβ value [22] with large tanβ usually lowering $\tilde{b}_1$ and $\tilde{t}_1$ masses compared to those of the other sparticles. An example of the mSUGRA mass spectrum is in Figure 1.3 where a model with $\mathrm{M}_0 << \mathrm{M}_{1/2}$ is assumed.

The gluino is the color octet fermion and it cannot mix with any other particle in the MSSM. In mSUGRA the gluino mass parameter M_3 is related to the bino and wino masses as follows:

$$M_3 : M_2 : M_1 \approx 3.3 : 1 : 0.5\ . \tag{1.29}$$

Therefore, the gluino should be much heavier than the lightest neutralino or chargino. Radiative corrections to the gluino mass can be relatively large due to the strong interaction

with all squark-quark pairs and its color octet nature. A general prediction for mSUGRA is that

$$m_{\tilde{Q}} \geq 0.85 m_{\tilde{g}} \tag{1.30}$$

which holds for the five lightest squarks and small or moderate[4] tanβ.

1.4.2 Squark and Gluino Production Processes

The hadroproduction of squarks and gluinos at the Tevatron in an R_p conserving mSUGRA scenario proceeds through the following partonic reactions:

$$\tilde{q}\bar{\tilde{q}} \text{ production:} \quad q_i + \bar{q}_j \longrightarrow \tilde{q}_k + \bar{\tilde{q}}_l \tag{1.31}$$

$$g + g \longrightarrow \tilde{q}_i + \bar{\tilde{q}}_i \tag{1.32}$$

$$\tilde{q}\tilde{q} \text{ production:} \quad q_i + q_j \longrightarrow \tilde{q}_i + \tilde{q}_j \text{ and } c.c. \tag{1.33}$$

$$\tilde{g}\tilde{g} \text{ production:} \quad q_i + \bar{q}_i \longrightarrow \tilde{g} + \tilde{g} \tag{1.34}$$

$$g + g \longrightarrow \tilde{g} + \tilde{g} \tag{1.35}$$

$$\tilde{q}\tilde{g} \text{ production:} \quad q_i + g \longrightarrow \tilde{q}_i + \tilde{g} \text{ and } c.c. \tag{1.36}$$

Here, the chiralities of the squarks are not noted explicitly, $\tilde{q} = (\tilde{q}_L, \tilde{q}_R)$ and the indices $i - l$ indicate the flavors of the quarks and squarks involved. Charge-conjugate processes (*c.c.*) are understood for $\tilde{q}\tilde{q}$ and $\tilde{q}\tilde{g}$ production. The corresponding Feynman diagrams are displayed in Figure 1.4.

The relative yields of $\tilde{q}\bar{\tilde{q}}$, $\tilde{q}\tilde{q}$, $\tilde{g}\tilde{g}$, and $\tilde{q}\tilde{g}$ final states at the Tevatron are shown for a set of mass parameters in Figure 1.5. They depend strongly on the relative mass difference between squarks and gluinos. If squarks are lighter than gluinos, the valence partons give the dominant yield of squark-antisquark or squark-squark pairs. If the gluinos are the lightest of the two species, their production is the most copious.

1.4.3 Squark and Gluino Decays

In an mSUGRA scenario with R_p conservation, signatures produced by sparticles in the detector are characterized by the presence of the LSP (the lightest neutralino, $\tilde{\chi}_1^0$) usually produced after a chain of successive decays of different complexity. The preferred decay modes for squarks are:

$$\tilde{q} \to q\tilde{g} \qquad \tilde{q} \to q\tilde{\chi}_i^0 \qquad \tilde{q} \to q'\tilde{\chi}_i^{\pm} \tag{1.37}$$

The preference for one decay or the other depend on the available phase space. In the case of the gluino, affected by strong interactions only, its decay proceeds through on-shell or virtual squarks:

$$\tilde{g} \to \bar{q}\tilde{q}_{L,R} \;\; (\tilde{g} \to q\bar{\tilde{q}}_{L,R}) \qquad \tilde{g} \to qq'\tilde{\chi}_i^0 \qquad \tilde{g} \to qq'\tilde{\chi}_i^{\pm} \tag{1.38}$$

The decay of charginos and neutralinos is quite complex since there are several possibilities and the final-state branching fractions are small and quite sensitive to the model. In general there is a strong correlation between the number of partons in the final state and the mass difference between squarks and gluinos. If squarks are significantly lighter than gluinos, $\tilde{q}\bar{q}$

[4] Small tanβ usually means tan$\beta < 10$, depending on the situation under study.

production is enhanced: squarks tend to decay according to $\tilde{q} \rightarrow q\tilde{\chi}_1^0$, and a topology with two partons and two neutralinos in the final state is favored. If gluinos are lighter than squarks, the $\tilde{g}\tilde{g}$ production dominates: gluinos decay via $\tilde{g} \rightarrow q\bar{q}\chi_1^0$, leading to topologies containing a larger number of partons (≥ 4). Finally, for $M_{\tilde{g}} \simeq M_{\tilde{q}}$, a intermediate topology is expected.

1.4.4 Heavy Flavor Squarks

As already mentioned, squark masses in mSUGRA originate from a mixture of their chiral states, with different contributions defined by the RGEs. This mixture is not particularly significant in the first two generations, while it becomes important for the stop and, at large tanβ, also for the sbottom. For this reason, the inclusive search for squark and gluino production is performed in a low tanβ scenario. The production of $\tilde{t}$ is neglected and the remaining squarks can be considered degenerate in mass with good approximation.

Searches for third generation squarks are usually addressed in dedicated analyses assuming specific SUSY models where their production is predominant. An example is the constraint MSSM scenario employed in the search for direct sbottom production described in Chapter 4. In this case, no particular model for SUSY breaking is assumed. The R-parity conservation leads to the production of the sbottom in pairs. As it has been the case in previous analyses [24][25], and to avoid model dependence of the decay branching fractions, the analysis is performed in the framework of the exclusive decay $\tilde{b}_1 \rightarrow b\tilde{\chi}_1^0$. The complete decay chain is

$$p\bar{p} \longrightarrow \tilde{b}_1\bar{\tilde{b}}_1 \longrightarrow (\tilde{b}_1\tilde{\chi}_1^0)(\bar{\tilde{b}}_1\tilde{\chi}_1^0) \tag{1.39}$$

leading to a final state with two b quarks and two neutralinos. With this assumptions, the region of the MSSM phase space where $M_{\tilde{\chi}_1^0} + M_b > M_{\tilde{b}_1}$ is kinematically forbidden. In the allowed region, kinematics of the events are strongly correlated to the mass difference $\Delta M = M_{\tilde{b}_1} - M_{\tilde{\chi}_1^0}$ between the sbottom and the neutralino.

1.5 Monte Carlo Simulation

In the analyses described in this Thesis, simulated event samples are used to determine detector acceptance and reconstruction efficiency, estimate part of the SM background contributions, and compute the number of expected SUSY events. This Section illustrates how the different physic processes occurring in a $p\bar{p}$ collision are taken into account. A review of the used MC generator programs is provided, together with the description of the techniques for the simulation of specific SM and SUSY processes.

Short description of a $p\bar{p}$ collisions:

In a typical high energy proton-antiproton collision, several physics processes occur. Although the theory does not allow to completely separate the different processes, the following steps implemented in MC models, sketched in Figure 1.6, provide an effective approach to simulate the resulting events.

- Initially two beam particles are coming in toward each other. Each particle is characterized by a set of parton distribution functions (PDF), which define the partonic substructure in terms of flavor composition and energy sharing.

- One shower initiator parton from each beam starts off a sequence of gluon radiation, such as $q \to qg$, which build up an initial-state shower (ISR).
- One incoming parton from each of the two showers is involved in the hard scattering process, a 2-to-2 process, that can be calculated by a perturbative approach, typically to first-order.
- The resulting partons start a parton cascade producing a multiple jets final state and following Altarelli-Parisi collinear approach in each branch.
- In the MC models employed in this Thesis, initial and final state radiation (ISR and FSR) are developed independently and interferences are not taken into account.
- Further semi-hard interactions may occur between the other partons of the two incoming hadrons.
- The remnants have internal structure and a net color charge that relates them to the rest of the final state.
- The QCD confinement ensures that no color is observed in the final state and phenomenological models are employed to produce hadrons.
- Many of the produced hadrons are unstable and decay further.

PDF parameterizations:

The parton structure of the incoming proton and antiproton is expressed in terms of parton density $f(Q^2, x)$ where the Q^2 evolution is determined by the DGLAP (Dokshitzer-Gribov-Lipatov-Altarelli-Parisi) evolution equations. The parameterization of the PDFs at a certain scale Q_0^2 is carried out through a χ^2 minimization over data from different processes such as deep-inelastic e, μ, or ν scattering, Drell-Yan production, W-asymmetry in $p\bar{p}$ collisions, and prompt photon production $pN \to \gamma X$. Different groups perform such parameterizations. In particular, the work presented here employs the parameterizations obtained by the *Coordinated Theoretical-Experimental Project on QCD* (CTEQ). The most recent set from the CTEQ Collaboration is the CTEQ6 where the following form has been chosen [26]:

$$xf(x, Q_0^2) = A_0 \cdot x^{A_1}(1-x)^{A_2} e^{A_3 x}(1 + e^{A_4} x)^{A_5} \ , \tag{1.40}$$

where A_i are the parameters to be fitted and f are the parton distribution functions. An example of these PDF's can be seen in Figure 1.7 at two different scales ($Q = 2$ GeV and $Q = 100$ GeV).

The limited knowledge of the PDFs constitutes an important source of uncertainty on the production cross sections. The evaluation of the uncertainties due the particular choice of PDFs is obtained with a Hessian method [27] based on the up and down variation of the parameters in the PDFs fits. This method determines the behavior of the χ^2 in the neighborhood of the minimum. Variations on the set of PDF parameters lead to new fits with certain χ^2. A parameter called tolerance, T, is defined and the new fits are considered acceptable if $\chi^2 - \chi_0^2 < T^2$, where χ_0^2 is the best fit to the global data set. CTEQ chooses $T^2 \sim 100$ which is interpreted to be a 90% CL uncertainty. In Figure 1.8, the uncertainties on

gluon and u-quark distributions are shown at a scale $Q^2 = 10$ GeV^2. The u-quark distribution is tightly constrained for $x \leq 0.8$. The gluon uncertainty is of order $\pm 15\%$ for $x \leq 0.3$ and then it increases rapidly for large x. These uncertainties also increase at higher energy scales when applying the DGLAP evolution equations. This constitutes one of the main sources of systematic uncertainty in the analyses presented here.

Initial- and Final-State Radiation (ISR/FSR):

Higher-order QCD processes are approximately implemented in the MC via initial- and final-state parton showers (PS) [28]. To describe them, both processes are set to be independent. In a hard process with virtuality Q^2, initial-state radiation is modelled by a sequence of emissions that, starting from the hadrons, increase the virtuality in each emission until it matches the Q^2 of the hard process. Similarly, the final-state radiation is constituted by a sequence of emissions that decreases the virtuality of the partons until a $Q_0^2 \sim \Lambda_{QCD}^2$ is reached. The parton shower is characterized by a strong angular ordering of the different emissions, dominated by the collinear component. Although the first branch in the parton shower is approximately performed according to the matrix elements, the collinear approximation is less accurate in reproducing the hardness of subsequent emissions.

Hadronization:

After the parton shower has finished, the final state consists of a set of partons with virtualities of the order of the cutoff scale $Q_0^2 \sim \Lambda_{QCD}^2$. QCD becomes strongly interacting at long distances (low momentum-transfer) and non-perturbative effects cannot be neglected. In this confinement regime, the colored partons are transformed into colorless hadrons in a process called hadronization or fragmentation. The tight cone of particles created by the hadronization of a single quark is called *jet* and it is observed at collider detectors as clustered energy depositions in the calorimeter. Since this process is still not understood from first principles, some phenomenological models have been constructed to describe it.

The *String Fragmentation Model* [29] assumes a linear confinement, i.e. the energy stored in the color dipole field between a q and a $\bar{q}$ is assumed to increase linearly with the separation between charges. This is a characteristic of QCD interactions due to the presence of a triple-gluon vertex. The physical picture is that of a color flux vortex line being stretched between a q and a $\bar{q}$ which are moving apart from their common vertex. The transverse dimensions of the tube are of typical hadronic sizes (~ 1 fm) and the tube is assumed to be uniform along its length. This automatically leads to a confinement picture with a linearly rising potential. As the q and $\bar{q}$ move apart, the potential energy stored in the string increases and may break producing a new $q'\bar{q}'$ pair. Hence the system is split in two color-singlet systems $q\bar{q}'$ and $q'\bar{q}$ from which, depending on their invariant mass, new breaking can occur. In the Lund string model, the string break-up proceeds until only on-mass-shell hadrons remain, each hadron corresponding to a small piece of string. Charm and heavier quarks are not expected to be produced in soft fragmentation, but only in perturbative parton-shower branchings $g \to q\bar{q}$. If more than two partons are moving apart the string structure becomes more complicated. For a $q\bar{q}g$ event, a string is stretched from the q end via the gluon (g) to the $\bar{q}$ end. To first approximation, there are two fragmenting string pieces hold by the gluon. But additional string regions may appear during the time evolution of the system and complicate the process. Figure 1.9 shows a schematic diagram of string fragmentation.

The *Cluster Fragmentation Model* [30]. is based on an important property of the branching processes which is the *color preconfinement* [31]. This property relies on the fact that the separation of the color charges forming a singlet are inhibited. After the perturbative parton branching process, remaining gluons are split into light $q\bar{q}$ pairs. Then, neighboring quarks and antiquarks can be combined into color singlets. These singlets have masses distribution and spatial size which peak at low values and are asymptotically independent of the hard subprocess scale. Most clusters have masses of up to few GeV and it is reasonable to consider them as superpositions of resonances. Clusters decay into hadrons according to two-body phase space. Figure 1.9 shows a schematic diagram of cluster fragmentation.

1.5.1 MC Generators

This Section briefly describes the characteristics of two broadly used event generators, Pythia and Alpgen, that are particularly relevant for the analyses presented in this Thesis. A description of other MC programs also used in this work (Isajet, Isasusy, MadEvent) is provided elsewhere [34, 39].

Pythia

Pythia [32] is a multipurpose event generator for ee, ep, and pp collisions broadly used in high energy physics (HEP) experiments. It uses LO matrix element (ME) calculations to generate hard interactions between partons and it is optimized for $2 \longrightarrow 1$ and $2 \longrightarrow 2$ processes. Pythia employs PS to generate higher multiplicity partonic states which can then be converted into the observed hadrons by the hadronization mechanism. The hadronization in Pythia is based on the string fragmentation model.

Given the LO character of the employed ME and the collinear approximation assumed for the PS, the program is expected to give a reasonable description of the jet structure, but has a limited predictive power in the description of large-angle parton emission and well separated multijet production (> 4 jets final state). To improve the description with large jet multiplicity, Pythia can be matched to other event generators that employ first order ME for multipartons final states, as in $2 \longrightarrow 3$ and $2 \longrightarrow 4$ processes. A typical example is the use of Pythia for the PS in combination with the Alpgen program described below.

Finally, Pythia uses several models to describe soft-gluon radiation, multiple parton interaction, and beam-beam remnants that constitute the so called *underlying events*. A number of parameters in Pythia control the amount and proportion of underlying events and can be tuned to reproduce data [35]. Pythia tune A is the default setting at CDF, optimized to reproduce specific measurements performed by the CDF experiment during the Run I of the Tevatron. Tune A settings mainly affect the initial state showers from the incoming hadrons, where the scale Q^2 is increased and the lower cut-off decreased to allow more radiation. The probability that the multiple parton interaction produces two gluons with color connections to their nearest neighbors is also increased. An alternative parametrization to tune A is tune BW, meant to describe accurately the distribution of the transverse momentum of the Z/γ^* boson at very low values of the transverse momentum $P_T < 5$ GeV/c.

Alpgen

Alpgen [33] program is dedicated to the study of multiparton hard processes in hadronic collisions with emphasis on configurations with large jet multiplicities. The code performs, at the leading order in QCD and EW interactions, the calculation of the exact matrix elements for a large set of parton-level processes. The evaluation of matrix elements gives a better description for processes with high jet multiplicities and large transverse momenta than the pure PS approach, where additional jets (with respect to the initial $2 \longrightarrow 2$ process) are generated only during the shower evolution. Alpgen generates only the hard process and does not include any form of hadronization. Thus, the output consists of bare quarks and gluons only. The showering and hadronization has to be done in a separate step with routines as they are implemented in general-purpose generators like Pythia. Interfacing the Alpgen output to an external showering package involves the risk that the same parton which was already generated in the matrix element calculation is added once again during the shower evolution. A solution for this problem is obtained with a matching procedure for matrix elements and parton showers to remove events which occur twice. The approach to remove double counted jet configurations is called MLM matching [33], and will be briefly described in the following Section.

1.5.2 Simulation of SM Processes

The big challenge of searches for Supersymmetric particles in events with energetic jets and large $\not\!\!E_T$ is the reduction of the SM background. This is very hard to achieve because the production cross sections of most of the SM processes are remarkably larger than the SUSY ones, regardless of the particular model assumed. As shown in Figure 1.10, there could be as many as 8 orders of magnitude between the production cross sections of typical SUSY events and the most frequent SM processes. It is clear that, to face the need of such a huge background reduction, the signal regions of typical SUSY searches are defined in the very tail of the kinematic distributions where SUSY and SM yields become comparable. Therefore, whenever a MC technique is employed in the estimation of a SM background, it is required an exceptional prediction power and a very high grade of accuracy. To fulfill these needs, the simulation methods used in our work vary according to the different SM processes they address and are briefly described in the following.

QCD multi-jet processes: All the QCD MC samples used in the analyses described in this Thesis are generated using Pythia tune A. As previously described, the partonic interactions are generated using leading-order QCD ME, including initial and final-states PS. CTEQ5L PDFs are used for the proton and antiproton. Different MC samples with different thresholds on $\mathrm{p_T}$ were produced to ensure enough MC statistics across the region of the $\mathrm{p_T}$ spectrum where the analyses are sensitive. In particular a minimum threshold at 60 GeV/c is applied. Special care was taken to avoid any bias coming from the presence of the different $\mathrm{p_T}$ thresholds in the MC. Once merged, the QCD samples are normalized to the observed cross sections by comparing MC to data in a low $\not\!\!E_T$ region.

$t\bar{t}$ processes: $t\bar{t}$ MC samples are generated with Pythia (tune A), fixing the top mass to 172 GeV/$\mathrm{c^2}$, closer to most recent top mass measurement results. The $t\bar{t}$ samples are then normalized to the corresponding NLO theoretical cross section [38], $\sigma_{\mathrm{t\bar{t}}} = 7.3$ pb.

single top processes: The two dominant single top production channels at the Tevatron are the tb production (s-channel) with a SM cross section of 0.88 pb, and the tqb pro-

duction (t-channel) with a cross section of 1.98 pb. Single top MC for both t and s channels are produced with the MadEvent [39] software interfaced with Pythia.

diboson processes: Generated with Pythia, all the diboson samples ($WW/WZ/ZZ$) are normalized with LO-to-NLO k-factors determined by the *Monte Carlo for FeMtobarn* program (MCFM) [40], a parton-level MC program which gives NLO predictions for a large range of processes at hadron colliders.

***W/Z* + jets processes:** W/Z boson+jets samples (all lepton modes) are generated using Alpgen interfaced with parton shower from Pythia (tune BW) as previously described. Final-state partons and shower-generated jets are matched using the MLM prescription, which allows to construct samples of arbitrary jet multiplicity, without double counting. The jets produced in the showering routine are matched to the partons obtained from the matrix element calculation. For this purpose, a jet clustering algorithm is applied to the final-state particles. The event is kept if each hard parton in the event can be matched to a jet otherwise it is rejected. The parton-level configuration for the samples is generated for a particular number of hard jets (exclusive samples). Only for the sample with the highest jet multiplicity, extra jets which do not match to hard partons are allowed to be present after the showering is performed (inclusive sample). In both the inclusive and the exclusive searches described in this Thesis, samples with zero to three partons in the final state, labelled as +0p, +1p .. +3p, are generated in exclusive mode: events which fail the matching criteria (N jets $\neq$ N partons) are rejected. Higher parton multiplicities (4 or more) are generated inclusively, using 4-partons matrix elements where events passing the matching criteria and having extra jets due to parton shower are accepted. For each distribution, the different samples, after MLM matching, are combined according to the following relative weights:

$$\mathrm{w_i} = \frac{\sigma_\mathrm{i}}{\sigma_\mathrm{TOT}}, \quad \mathrm{i} = 0 - 4, \tag{1.41}$$

where σ_i denotes the resulting cross section (after MLM matching) for the i-th contribution and $\sigma_\mathrm{TOT} = \sum \sigma_i$ is the sum of the cross sections. The whole Boson+jets sample is then normalized to the inclusive W/Z cross section taken from the data[37], where measurement results are:

$$\sigma_W \times Br(p\bar{p} \to W \to l\nu) = 2.775 \pm 0.010(stat) \pm 0.053(syst)nb$$

and

$$\sigma_{\gamma^*/Z} \times Br(p\bar{p} \to \gamma^*/Z \to ll) = 254.9 \pm 3.3(stat) \pm 4.6(syst)pb$$

When needed, exclusive samples with a given number of heavy-flavor partons (b/c quarks) in the final state can be produced with the same technique and then merged to the inclusive samples previously described to enhance the statistic of the heavy-flavor events. In performing this merging between inclusive samples and heavy-flavor exclusive samples special care is needed to avoid any possible double counting of events with the same parton configuration in the final state. The matching strategy employed in the exclusive search for sbottom production is described in Chapter 4.

1.5.3 Simulation of SUSY Processes

The SUSY processes relevant for this Thesis are generated with the Isasusy [34] implementation of Pythia (tune A), to combine LO ME with PS as previously described. The cross

sections for the production of squarks and gluinos in hadron collisions were calculated at the Born level in 1992 [41]. The LO predictions suffer from large uncertainties on the absolute normalization due to a large dependence on the scale. Therefore, NLO predictions are employed to normalize the four different processes described in Section 1.4.2: gluino-gluino (gg), squark-gluino (sg), squark-squark (ss), and squark-antisquark (sb). There is up to a factor of 2 between the NLO and LO cross sections depending on the particular process and the masses involved. The values of the NLO cross sections for squark and gluino productions employed in the present study are based on PROSPINO [43] calculations. In the inclusive search for squarks and gluinos, the PROSPINO cross sections are computed using CTEQ61M PDFs, and renormalization and factorization scale set to the average mass of the supersymmetric particles produced in the final state:

- gluino-gluino (gg): $\mu = \mathrm{M}_{\tilde{\mathrm{g}}}$
- squark-gluino (sg): $\mu = 0.5[\mathrm{M}_{\tilde{\mathrm{g}}} + \overline{\mathrm{M}}_{\tilde{\mathrm{q}}}]$
- squark-squark (ss): $\mu = \overline{\mathrm{M}}_{\tilde{\mathrm{q}}}$ (in this subprocess we also find antisquark-antisquark production)
- squark-antisquark (sb): $\mu = \overline{\mathrm{M}}_{\tilde{\mathrm{q}}}$

where $\overline{\mathrm{M}}_{\tilde{q}}$ is the average mass of the squarks considered. In the last version of the software (PROSPINO2), stop and sbottom productions can be treated separately from the production of the other mass-degenerate squarks and cross sections for $\tilde{b}\tilde{b}$ or $\tilde{t}\tilde{t}$ processes alone can be computed. In the exclusive search for direct sbottom pair production, the NLO cross sections are computed with PROSPINO2 using CTEQ6.6 PDFs, and the renormalization and factorization scale set to the mass of the sbottom $\mu = M_{\tilde{b}_1}$.

Figure 1.1: one-loop quantum corrections to $m^2_{H_{SM}}$.

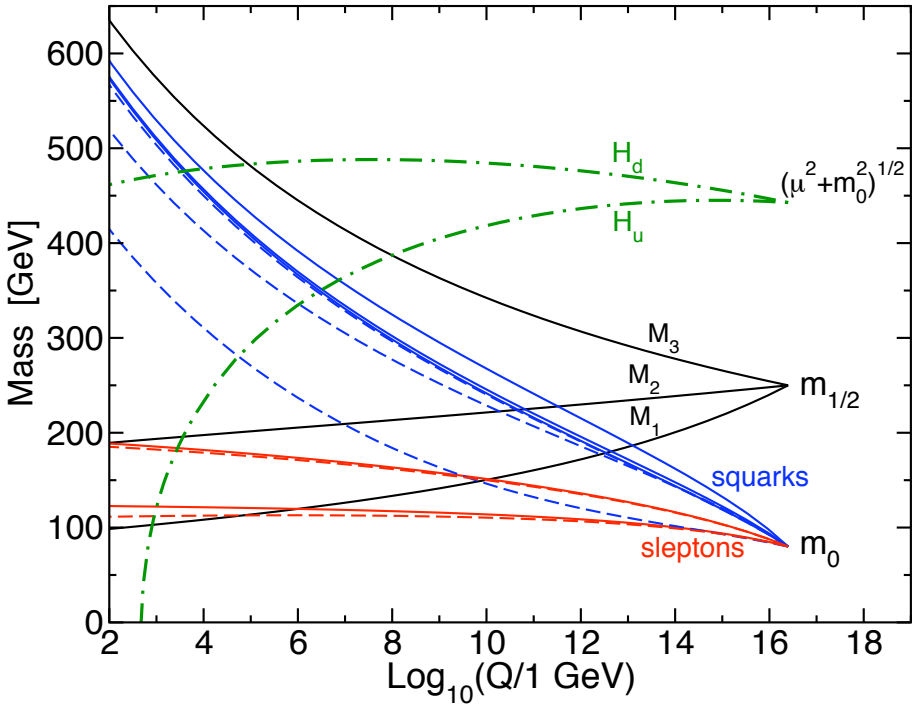

Figure 1.2: running of sparticle masses from the GUT scale to the electroweak scale, for a representative set of input parameters.

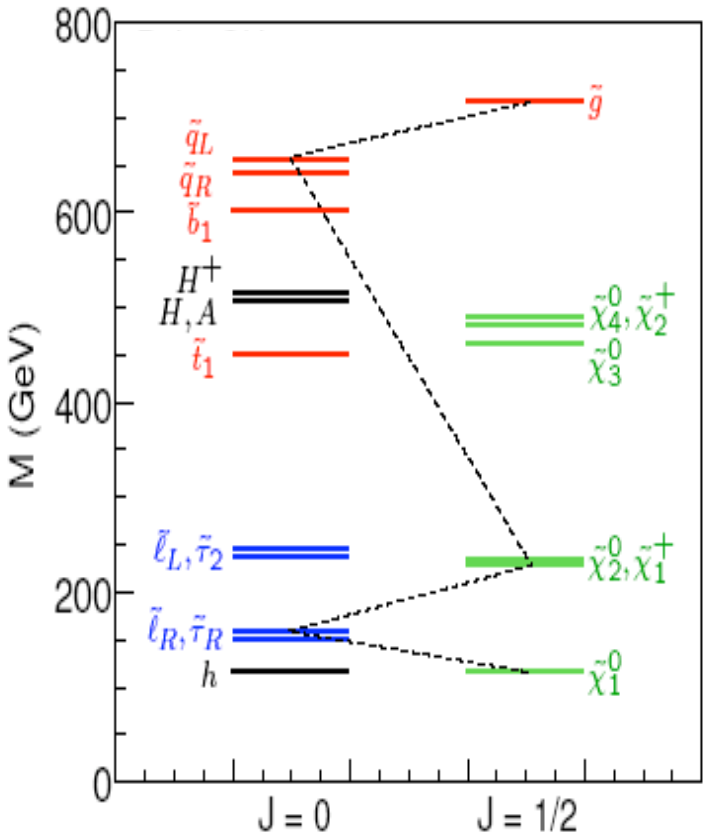

Figure 1.3: example of a typical mSUGRA mass spectrum. The dashed line indicates the usual gluino decay chain all the way to the LSP neutralino ($\tilde{\chi}_1^0$).

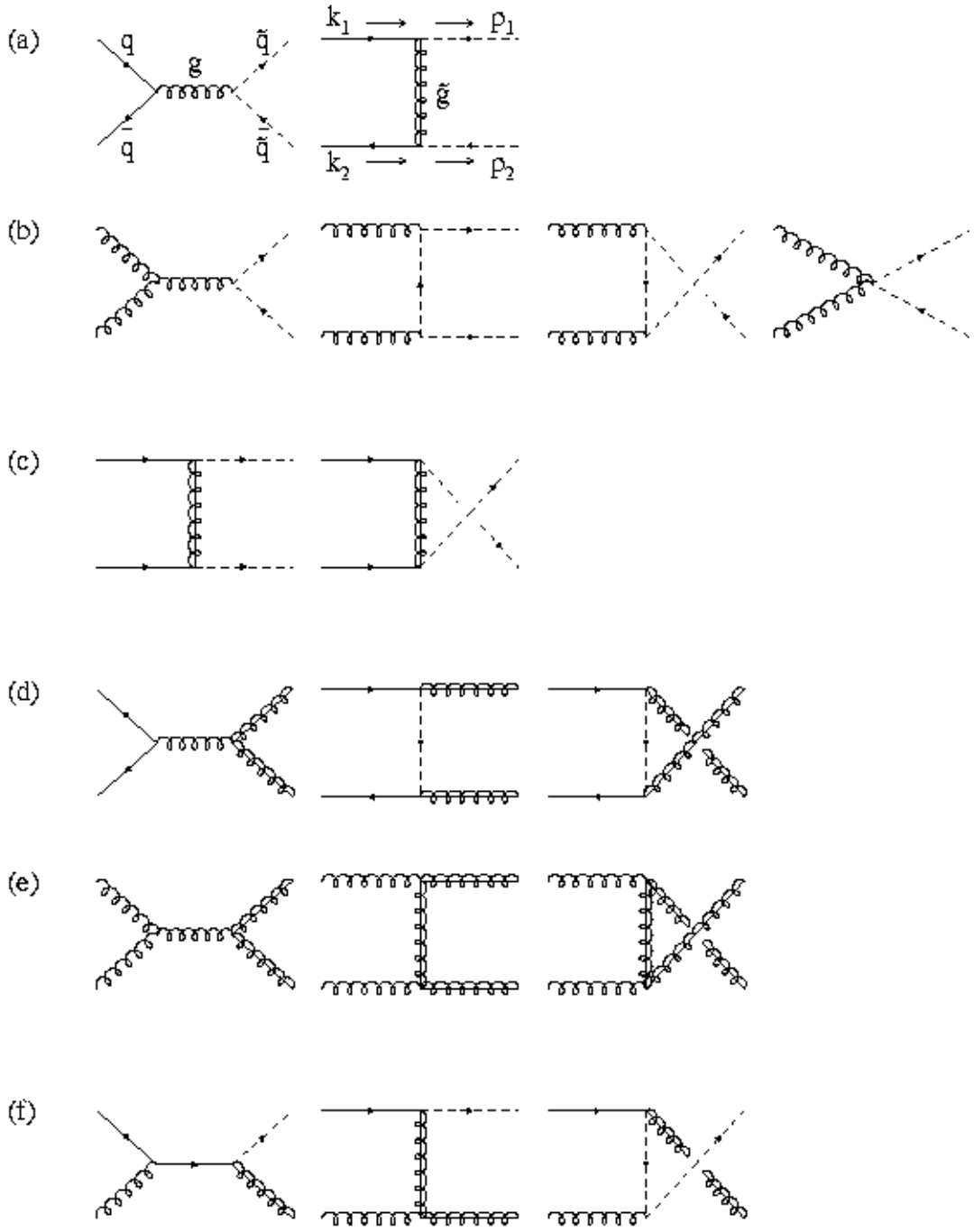

Figure 1.4: Feynman diagrams for the production of squarks and gluinos at the leading order. The diagrams in (c) and the last diagram in (d) are result of the Majorana nature of gluinos. Some of the above diagrams contribute only for specific flavors and chiralities of the squarks [23].

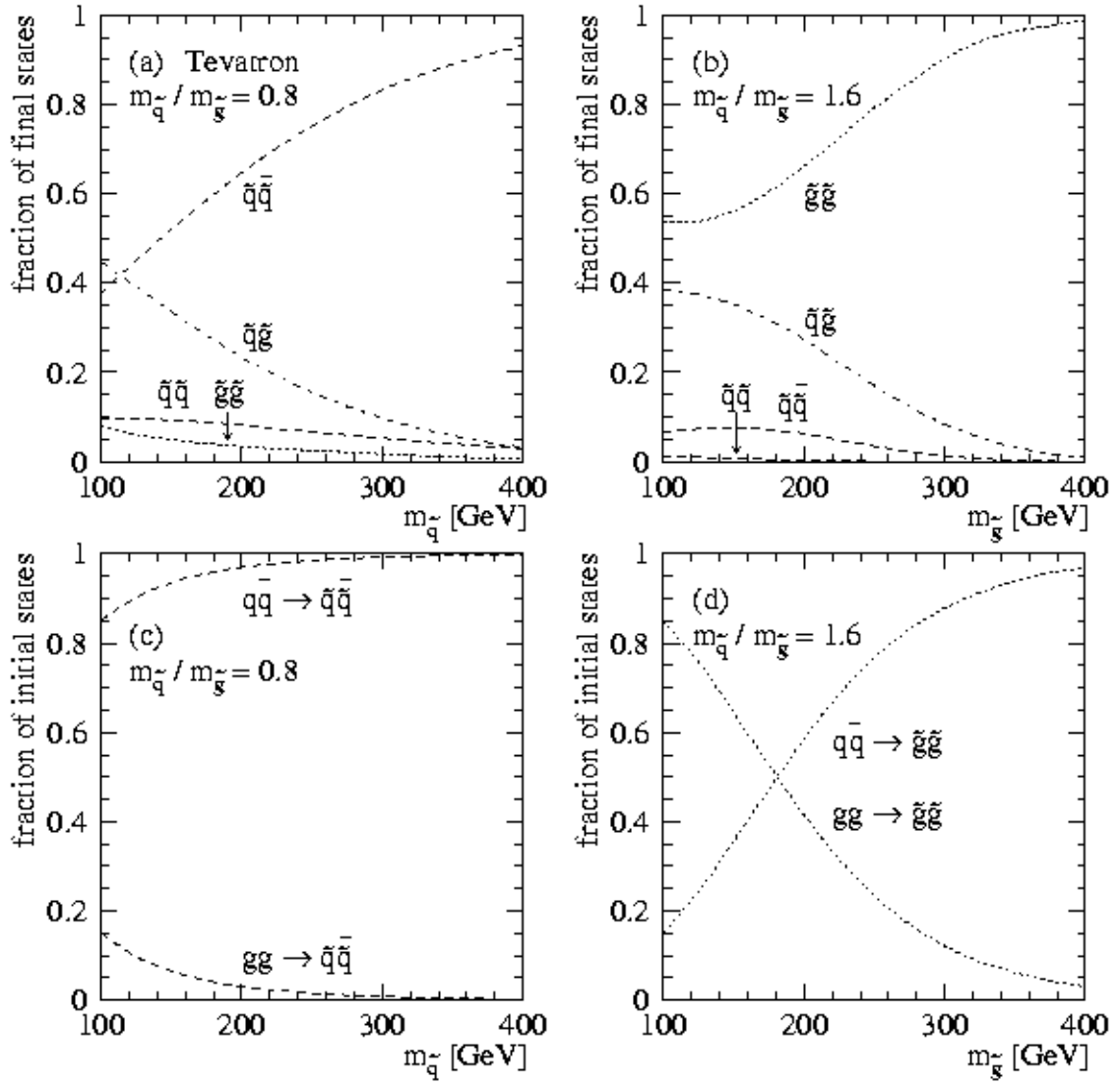

Figure 1.5: relative yields of the squarks/gluinos production sub-processes at the Tevatron. The mass ratio $M_{\tilde{q}}/M_{\tilde{g}}$ is chosen to be (a) 0.8 and (b) 1.6. Also shown are the leading parton contributions for (c) $\tilde{q}\bar{\tilde{q}}$ and (d) $\tilde{g}\tilde{g}$ final states.

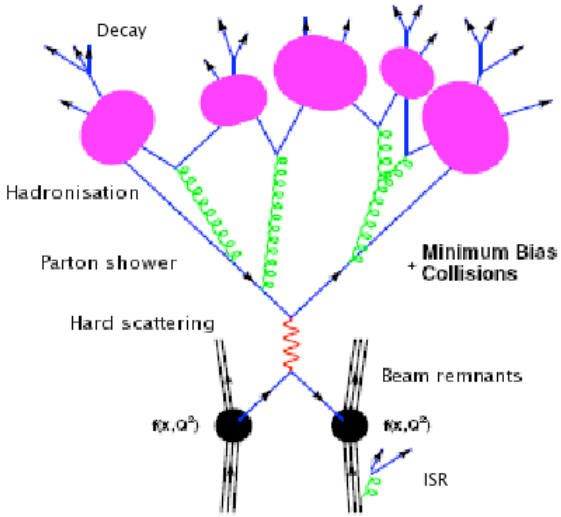

Figure 1.6: an example of the different processes occurring at a $p\bar{p}$ collision.

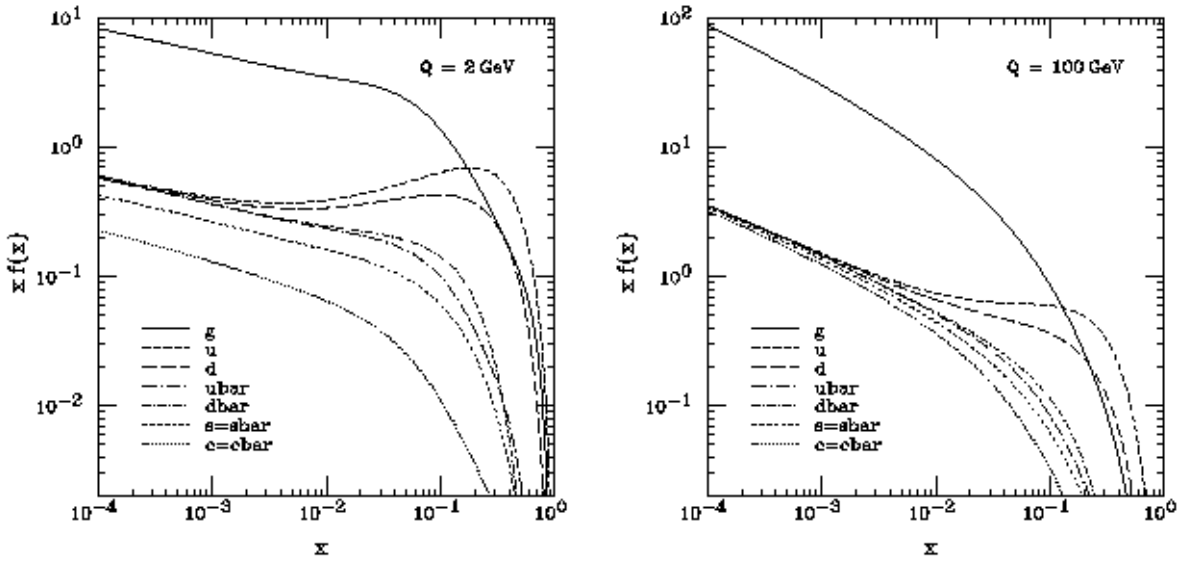

Figure 1.7: CTEQ6 parton distribution functions at $Q = 2$ GeV and $Q = 100$ GeV.

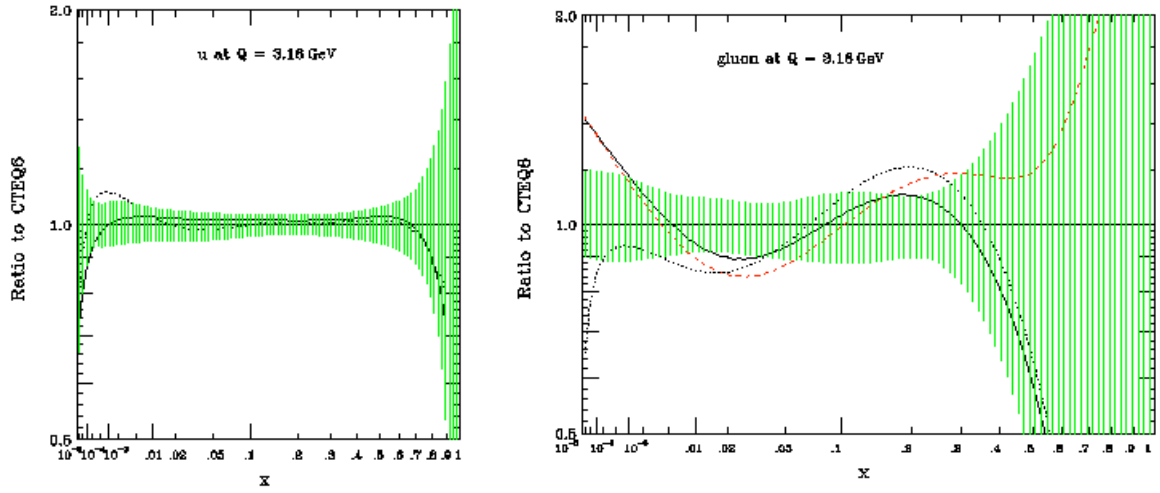

Figure 1.8: uncertainty bands for the u-quark (left) or gluon (right) distribution functions at $Q^2 = 10$ GeV^2. The other lines are from different type of parameterizations not discussed here.

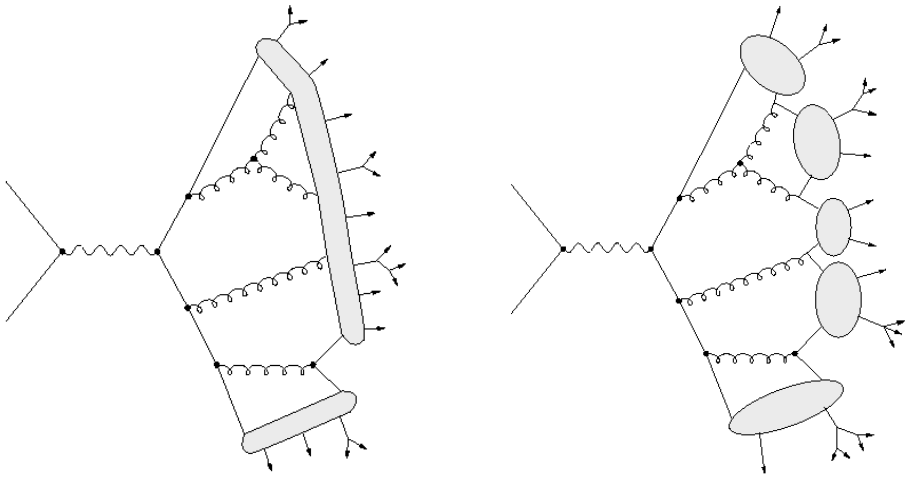

Figure 1.9: a representation of the string (left) and cluster (right) fragmentation models.

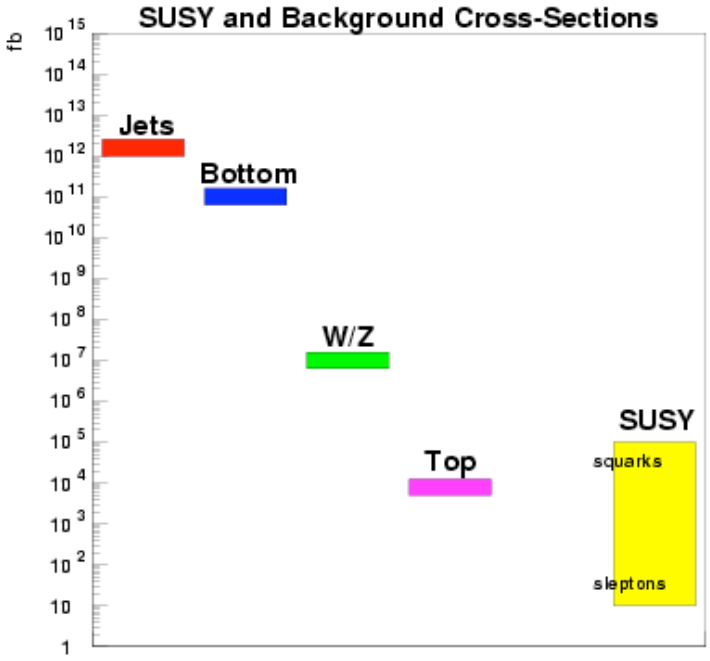

Figure 1.10: comparison between SUSY cross sections and the cross sections of typical SM processes.

Chapter 2

Experimental Apparatus

With its 6,800-acre site located just 35 miles west of Chicago, Illinois, the Fermi National Accelerator Laboratory (Fermilab) is one of the largest and most important particle physics facilities in the world. It currently hosts the Tevatron, the second highest energy particle accelerator after the Large Hadron Collider (LHC) in Geneva. Commissioned by the Department of Energy in the late 1960's, in the past 40 years the Fermilab hosted numerous experiments whose results have made crucial contributions to the understanding of SM. In 1977, the E288 experiment observed the new Upsilon particle, giving the first evidence for the existence of the bottom quark. In 1995 the CDF and DØ experiments at the Tevatron completed the quark sector with the observation of the top quark. Finally, in July 2000, DONUT announced the first direct observation of the tau neutrino, filling the final slot in the lepton sector.

After the completion of an ambitious program of upgrades, the Run II of the Tevatron Collider started in March 2001 and had the first physics run in February 2002. In this Chapter, we briefly describe the Tevatron accelerator and the CDF experiment in the Run II.

2.1 The Tevatron Collider

The Fermilab accelerator complex shown in Figure 2.1 is composed of five different accelerators: the Cockroft-Walton, the Linac [44], the Booster [44], the Main Injector [45], and the Tevatron. They work in cascade and accelerate 36 proton on 36 antiproton bunches at a center-of-mass energy of $\sqrt{s} = 1.96$ TeV with a bunch spacing of 396 ns. Data from the Tevatron are collected by the CDF II and DØ experiments located along the accelerator ring in two different points where the proton and antiproton beams collide.

The Tevatron was originally designed to produce collisions at 2×10^{32} cm^{-2}s^{-1} instantaneous luminosity, which was reached in the end of 2006. In the following years, new luminosity records have been continuously broken with peaks over 3.5×10^{32} cm^{-2}s^{-1} as displayed in Figure 2.2. With the good performance of the accelerator, each experiment has collected almost 8 fb^{-1} of data since the beginning of Run II. Figure 2.3 shows the integrated luminosity delivered by the Tevatron and the total luminosity recorded by the CDF experiment. With the machine scheduled to continue running until the end of 2010, both CDF and DØ are expected to collect up to 9 fb^{-1}. An additional year of running in 2011 has been approved with

the potential of adding approximately another 2 fb^{-1} of data before the end of operations.

2.2 The CDF II Experiment

The Collider Detector at Fermilab Run II (CDF II) [46] is designed to detect and measure properties of particles produced in $p\bar{p}$ collisions. It is a multipurpose detector combining precision charged particle tracking with fast projective calorimetry and fine grained muon detection. The layout is standard for detectors of this type. From the inside-out there are: tracking system, time of flight detector, electromagnetic calorimeter, hadronic calorimeter, and muon chambers on the far outside. The tracking system is immersed in a 1.4 T magnetic field, parallel to the beam axis and generated by a superconducting solenoid of 4.8 m length and 1.5 m radius. The solenoid is located between the tracking system and the calorimeters. The superconductor is made of Al-stabilized NbTi and operate at liquid helium temperature. The magnetic field is uniform with an accuracy of 0.1% throughout the entire tracking volume.

A brief description of each sub-detector is provided in the following sections, with special emphasis on those apparatuses, tracking system and calorimeters, that play an important role in the analyses described in this Thesis.

2.2.1 The CDF Coordinate System

Due to its azimuthal and forward-backward symmetry, the CDF II detector is conveniently described with a polar coordinate system (r, θ, ϕ) sketched in Figure 2.4 with the detector geometric center as its origin. The direction of a particle in the detector can be expressed in terms of its rapidity $y = \frac{1}{2}\ln[\frac{E+p_z}{E-p_z}]$, with the advantage that intervals of y are invariant under Lorentz boosts along the z-axis. The rapidity has a convenient ultra-relativistic massless approximation $\eta = -\ln(\tan[\frac{\theta}{2}])$ called pseudo-rapidity, with a direct geometrical interpretation in terms of the angle θ. Figure 2.6 shows the different η coverage for some of the components of the CDF detector.

2.2.2 The Tracking System

At CDF II there are two main tracking systems, the silicon detector and the Central Outer Tracker, both briefly described below.

The silicon detector: the Run II silicon detector [47] consists of three sub-systems, Layer 00 (L00), Silicon Vertex Detector (SVX), and Intermediate Silicon Layers (ISL), arranged in a barrel geometry that extends from the radius $r = 1.35$ cm to $r = 28$ cm, and covers the tracking in the range $|\eta| < 2$. Built in three cylindrical barrels each 29 cm long, the SVX system is the most important among the silicon components. Each of the three barrels supports five layers of double sided silicon micro-strip detectors which can combine $r - \phi$ measurements with information from stereo angles for three-dimensional tracking. The SVX alone is capable of measuring the impact parameter d_0[1] and the z_0 with a resolution of 40 μm and 70 μm, respectively. The two other subsystems, L00 and ISL, are meant to broaden the physics reach of SVX. The L00 is the innermost subsystem located around the beam vacuum pipe at a minimum radius of 1.35 cm. It improves the measurement of d_0

[1] d_0 is the track impact parameter whose absolute value corresponds to the distance of the closest approach of a track to the beam-line

making possible resolutions as small as 25 μm. Finally, the ISL consists of three separate silicon layers and serves as a link between the inner silicon tracking region and the outer wire tracker.

The Central Outer Tracker: the Central Outer Tracker (COT) [48] is a drift chamber with 96 sense wire layers which are radially grouped into eight *super-layers* as inferred from the end-plate section in Figure 2.7. Each super-layer is divided in ϕ into *super-cells*. Each super-cell has 12 sense wires and a maximum drift distance that is approximately the same for all super-layers. Therefore, the number of super-cells in a given super-layer scales approximately with the radius of the super-layer. The entire chamber contains 30,240 sense wires. Approximately half the wires are parallel to the z-axis (*axial wires*), while the other half are strung at a small angle with respect to the z direction (*stereo wires*). With its inner radius of $r = 43.3$ cm, the COT surrounds the ISL and extends to an outer radius of $r = 132.3$ cm. It is 310 cm long and particles with $|\eta| < 1$ pass through all eight super-layers as shown in Figure 2.8. Particles with $|\eta| < 1.3$ pass through 4 or more super-layers. The COT has a maximum acceptance of $|\eta| < 2$.

The proportional drift chamber is filled with Ar:C2H6 (50:50) mixture with a small admixture of isopropyl alcohol and oxygen to prevent aging. This mixture is chosen to achieve a uniform gain ($\approx 2 \cdot 10^4$) and drift field with relatively high velocities (≈ 100 μm/ns) for all the sense wire drift cells. The maximum drift distance in a cell is 0.88 cm which allows for a maximum drift time of 100 ns, well enough inside the bunch crossing time window of 396 ns. The COT single-hit resolution has been measured *in situ* using Z boson decays into muon pairs, $Z \to \mu\mu$, to be about 140 μm. The momentum resolution has been measured to be $\sigma_{p_T}/p_T^2 \approx 1.5 \times 10^{-3}[\text{ GeV/c}]^{-1}$ using muon cosmic rays.

2.2.3 The Time Of Flight

The Time Of Flight (TOF) detector [49] expands CDF's particle identification capability in the low p_T region. TOF measures arrival time t of a particle with respect to the collision time t_0. The mass m of the particle is then determined using the path length L and the momentum p measured by the tracking system via relationship

$$m = \frac{p}{c}\sqrt{\frac{(ct)^2}{L^2} - 1}. \tag{2.1}$$

The TOF consists of 216 scintillator bars installed between the outer shell of the COT and the superconducting solenoid. The timing resolution of the TOF system is currently about 110 ps for particles crossing the bar exactly in front of one of the photomultiplier tubes.

2.2.4 The Calorimeters

The CDF calorimetry system, located immediately outside the solenoid, measures the energy of neutral and charged particles. A schematic view is shown in Figure 2.9. The CDF calorimeter is organized into two subsystems: the inner electromagnetic and the outer hadronic sections, optimized to detect electromagnetic and hadronic showers respectively. These scintillator-based sampling calorimeters are segmented in projective towers pointing to the center of the detector. Each tower consists of layers of passive material alternated with scintillator tiles. Particles, gradually absorbed by the passive material, leave a signal in the

scintillator which is read by wavelength shifters (WLS) and carried through light guide to photo-multiplier tubes.

The calorimeter system instruments two regions: a central calorimeter with a pseudo rapidity coverage of $|\eta_{\rm det}| < 1.1$, and a forward calorimeter with $1.1 < |\eta_{\rm det}| < 3.6$. The towers of the central electromagnetic calorimeter (CEM) [50] interleave plastic scintillators tiles with lead, while in the central and end-wall hadronic calorimeters (CHA, WHA) [51] the passive layers are made of steel. Each tower covers approximately 0.1 unit in pseudo-rapidity and 15 in azimuthal angle. The CEM thickness is 18 radiation lengths[2] (X_0) and the CHA-WHA thickness is 4.7 interaction lengths[3] (λ_I). The energy resolution for each section was measured with test beams and can be parametrized as

$$\left(\frac{\sigma}{E}\right)^2 = \left(\frac{\sigma_1}{\sqrt{E}}\right)^2 + (\sigma_2)^2 \ , \tag{2.2}$$

where the first term comes from sampling fluctuations and the photo-statistics of PMTs and the second term comes from the non-uniform response of the calorimeter. In the CEM, the energy resolution for high energy electrons and photons at normal incidence is $\frac{\sigma}{E_T} = \frac{13.5\%}{\sqrt{E_T}} \oplus 2\%$, where the energy is expressed in GeV. In CHA and WHA detectors, charged pions were used to obtain the energy resolution and it was found to be $\frac{\sigma}{E_T} = \frac{50\%}{\sqrt{E_T}} \oplus 3\%$ and $\frac{\sigma}{E_T} = \frac{75\%}{\sqrt{E_T}} \oplus 4\%$, respectively. The average energy loss per Minimum Ionizing Particle (MIP) in the calorimeter is around 0.5 (1.6) GeV for electromagnetic (hadronic) parts.

The forward or *plug* calorimeters [52] employ iron instead of steel as passive material in the hadronic section. The η coverage of the towers vary depending on the pseudo-rapidity region[4] from 0.1 to 0.6 and the ϕ coverage vary from 7.5 in the region $1.1 < |\eta| < 2.1$ to 15 in the region $2.1 < |\eta| < 3.6$. Towers in the plug electromagnetic section (PEM) match those of the hadronic section (PHA), except for the lowest η PEM tower which does not have a corresponding PHA tower. The PEM thickness is $23X_0$ and the PHA thickness is $6.8\lambda_I$. The energy resolution for the plugs was determined to be $\frac{\sigma}{E} = \frac{16\%}{\sqrt{E}} \oplus 1\%$ for PEM and $\frac{\sigma}{E} = \frac{80\%}{\sqrt{E}} \oplus 5\%$ for PHA where the resolution is given as a function of the total energy. Table 2.1 summarizes the most significant characteristics of the CDF calorimetry.

It is worth mentioning that there are two main uninstrumented regions in the calorimeter system: the *chimney* and the *cracks*. The former is located in the CEM and occupy the place of one azimuthal wedge module to allow the passage to the CDF cryo system pipes of the superconducting solenoid. The cracks are instead the junctions between the two symmetrical central modules and between the WHA and the PHA at $\eta = 0$ and $|\eta| = 1.1$, respectively.

The central and forward parts of the calorimeter have their own shower profile detector positioned at the expected maximum of the lateral shower profile (approximately at $6X_0$). The Central Electromagnetic Showermax (CES) [53] and the Plug Electromagnetic Showermax (PES) [54] are designed to measure the position of electron and photon showers and to help on separating single electrons and photons from the photons produced in $\pi^0 \to \gamma\gamma$ decays. The Central Pre-Radiator (CPR) [55] is located at the inner face of the central calorimeter

[2]The radiation length X_0 describes the characteristic amount of matter traversed for high energy electrons in order to lose all but 1/e of its energy by bremsstrahlung.

[3]An interaction length is the average distance a particle will travel before interacting with a nucleus.

[4]The segmentation optimize $e^{\pm}$ identification in $b/\bar{b}$ jets ($b \to e + X$ processes) [46].

Calorimeter	CEM	CHA	WHA	PEM	PHA
Absorber	Lead	Steel	Steel	Lead	Iron
Segmentation ($\eta \times \phi$)	0.1×15	0.1×15	0.1×15	$(0.1-0.6)\times$ $(7.5-15)$	$(0.1-0.6)\times$ $(7.5-15)$
Num. Towers ($\eta \times \phi$)	20×24	9×24	6×24	$12 \times 24(48)$	$11 \times 24(48)$
Thickness	$18X_0,\ 1\lambda_I$	$4.7\lambda_I$	$4.7\lambda_I$	$23X_0,\ 1\lambda_I$	$6.8\lambda_I$
Resolution (%)	$14/\sqrt{\mathrm{E_T}} \oplus 2$	$50/\sqrt{\mathrm{E_T}} \oplus 3$	$75/\sqrt{\mathrm{E_T}} \oplus 4$	$16/\sqrt{E} \oplus 1$	$80/\sqrt{E} \oplus 5$

Table 2.1: summary of the main characteristics of the CDF II calorimeter system.

and consists of several multi-wire proportional chambers which sample the electromagnetic shower that begins in the solenoid magnetic material (approximately $1X_0$) in front of them. The Plug Pre-Radiator (PPR) [56] serves a similar purpose but it is located in front of the plug calorimeters.

2.2.5 The Muon Detectors

The muon system [57] is the outermost layer of the CDF II detector. It consists of four sub-detectors with similar functioning: the central muon chambers (CMU), the central muon upgrade chambers (CMP), the central muon extension (CMX), and the intermediate muon system (IMU). The systems consists on drift cells and scintillation counters which are used to reconstruct the tracks from minimum ionizing particles. These tracks are matched using dedicated algorithms with the COT information in order to reconstruct the full trajectory of the muons.

2.2.6 CLC and Luminosity Measurement

The luminosity ($\mathcal{L}$) at CDF is determined from the rate of inelastic $p\bar{p}$ interactions in the Cherenkov Luminosity Counters (CLC) [58] detector. The CLC occupies the conical holes ($3.75 < |\eta| < 4.75$) between the plug calorimeters and the beam pipe as shown in Figure 2.10. The CLC is designed to measure the average number of inelastic interactions per bunch crossing, μ, within a few percent, up to the high luminosity regimes expected for the Tevatron. Then, the luminosity is extracted using:

$$\mu \cdot f_{BC} = \sigma_i \cdot \mathcal{L} \ , \tag{2.3}$$

where σ_i is the inelastic proton-antiproton scattering cross section[5] and f_{BC} is the frequency of bunch crossing, which is on average 2.5 MHz for 36×36 bunch operations. Since the number of interactions n per bunch crossing follows Poisson statistics with mean μ, one can have a good estimator for μ measuring the probability of empty bunch crossings $n = 0$:

$$\mathcal{P}(0) = e^{-\mu} \ . \tag{2.4}$$

An empty bunch crossing is observed when there are less than two tubes with signals above threshold in either module of the CLC. The measured fraction of empty bunch crossings is

[5]The proton-antiproton inelastic cross section at the Tevatron is $\sigma_i = 59.3$ mb.

corrected for the CLC acceptance and the value of μ is calculated. The total systematic uncertainty on the luminosity [59] is about 6%, which originates from uncertainties in the acceptance (4.4%) and from the inelastic cross section normalization (4%).

2.2.7 The Trigger System

With a collision rate of roughly 2.5 MHz and an average size of 100 kB per event, storing the data from all the $p\bar{p}$ collisions would require an impossible mass storage and throughput capability of 25 TB/s (1.5×10^7 TB a week!). However, only a small fraction of events contains interesting information for the physics analyses and the role of the CDF II trigger is to select those events of interest and reduce data rates and volumes to manageable levels. The trigger decision is staged in three levels as shown in Figure 2.11. Each level provides a rate reduction sufficient to allow for processing in the next level with minimal dead time.

Level 1 (L1) uses designed hardware to make decisions based on simple physics quantities in the events and using a subset of the detector information. As shown in Figure 2.12, three different streams of information allow L1 to make a decision: calorimeter objects that may be further reconstructed into electrons, photons, or jets; track segments in the muon detector and tracking data to identify tracks which can be linked to objects in the calorimeter or muon detector. The L1 trigger decision takes place 5.5 μs after a collision and it works in parallel through a pipeline that can store up to 14 bunch crossings. This buffered data is needed in order to accommodate the average input rate of 2.5 MHz, determined by the Tevatron bunch configuration. After L1, the event rate is reduced to less than 50 kHz.

The level 2 (L2) is a combination of hardware and software triggers that perform limited event reconstruction using programmable processors. These events are stored in one of four asynchronous buffers and the decision whether they are accepted or not is based on calorimeter cluster algorithms, shower information from Showermax detectors and combined tracking information from L1 and from SVX II, which is crucial in order to trigger on different tracking features like the impact parameter d_0. This level of decision takes approximately 25 μs and further reduces the event rate to approximately 300 Hz.

The level 3 (L3) consists of two components: an *event builder* and a Linux PC farm. As shown in Figure 2.13 the detector readout from the L2 buffers is received via an Asynchronous Transfer Mode (ATM) switch and distributed to 16 PC nodes. The main task of these nodes is to assemble all the pieces of the same event as they are delivered from different sub-detectors through the ATM switch. The event is then passed to a processor node consisting on a separate dual-processor PC. There are about 150 processor nodes and each of the two CPUs processes a single event at a time. The L3 decision is based on a near-final quality reconstruction which, if it passes certain criteria, it is sent to the Consumer Server / Data Logger (CS/DL) system for storage first on disk and then on tape. This level of decision reduces the event rate to approximately 75 Hz.

2.2.8 Data Quality Monitoring

Collected events undertake some quality controls to ensure that the different sub-systems were in good conditions at the moment of the data-taking. These series of controls involve statistical tests of different levels of complexity for some of the most sensitive kinematic variables. These tests are implemented on-line, to resolve possible problems *on the fly*, and

offline, when a careful reconstruction of the whole event is performed with the final calibrations. Data is validated in *runs* and grouped in several lists (*GoodRunLists*) according to specific quality criteria that make the data suitable for different kind of analyses.

2.3 Physics Objects and Analysis Tools

2.3.1 Jets and Jet Energy Scale

Jets are the experimental signatures of the production of high-momentum gluons and quarks, which hadronize into a large number of collimated particles that deposit a cluster of energy in EM and HAD calorimeter towers.

In this Thesis, jets are reconstructed using the CDF JETCLU cone algorithm [60]. As a first step, electromagnetic and hadronic calorimeter towers are combined into *physics towers* whose transverse energies is defined as $E_{Ti} = E_i^{em} sin\theta_i^{em} + E_i^{had} sin\theta_i^{had}$ where $\theta^{em(had)}$ is the azimuthal angle of the electromagnetic (hadronic) compartment of the tower with respect to the z-position of the primary vertex. Every physics tower with a transverse energy $E_{Ti} > 1$ GeV (*seed tower*) initiates the algorithm. For each seed tower, all the towers with $E_{Ti} > 100$ MeV within a radius of size R are gathered into *clusters*. The cone aperture is defined in the $\eta - \phi$ plane as $R = \sqrt{(\eta^{tower} - \eta^{jet})^2 + (\phi^{tower} - \phi^{jet})^2}$. A cone of a radius R=0.7 is chosen for the inclusive analysis in Chapter 3, while a cone of R=0.4 is employed for the sbottom search in Chapter 4. Once an initial list of clusters is found, the transverse energy and the location (centroid) of each cluster is calculated using the Snowmass definitions:

$$E_T(\text{jet}) = \sum_{i=0}^{N_{tow}} E_{Ti} \tag{2.5}$$

$$\phi(\text{jet}) = \sum_{i=0}^{N_{tow}} \frac{E_{Ti}^{em}\phi_i^{em} + E_{Ti}^{had}\phi_i^{had}}{E_T(\text{jet})} \tag{2.6}$$

$$\eta(\text{jet}) = \sum_{i=0}^{N_{tow}} \frac{E_{Ti}^{em}\eta_i^{em} + E_{Ti}^{had}\eta_i^{had}}{E_T(\text{jet})} \tag{2.7}$$

where N_{tow} is the number of towers inside the cluster. This procedure is repeated iteratively, with a new list of towers around the new centroid determined at each iteration. The jet transverse energy E_T(jet) and direction are recalculated until the list of towers assigned to the clusters is stable. The last step of the algorithm deals with overlapping jets: if the transverse energy common to two clusters amounts to more than 75% of the smaller cluster, the two clusters are merged into a single jet; otherwise overlapping towers are assigned to the nearest jet. Finally, the kinematics of the jet is computed using the jet constituent and a 4-vector sum leading to massive jets.

Ideally, to each jet corresponds a single parent parton from which the jet originates. However, the reconstructed energy of a jet is only an approximation of the original parton energy. The measured jet transverse momentum is corrected for detector effect back to the

hadron level[6] to remove all dependencies on the detector device:

$$p_T^{particle} = (p_T^{jet} \times C_\eta - C_{MI}) \times C_{Abs} \tag{2.8}$$

where

- $p_T^{particle}$ is the transverse momentum of the particle jet, that is, a jet corrected by all instrumental effects which corresponds to the sum of the momenta of the hadrons, leptons, and photons within the jet cone.
- p_T^{jet} is the transverse momentum measured in the calorimeter jet.
- C_η, "η-dependent" correction, ensures homogeneous response over the entire angular range, and refers the rest of the corrections to a well-understood region of the detector.
- C_{MI}, "Multiple Interaction" correction, is the energy to subtract from the jet due to pile-up of multiple $p\bar{p}$ interactions in the same bunch crossing. The number of reconstructed z-vertices (N_{Vz}) is the best estimate of the number of interactions in a bunch crossing. Therefore, C_{MI} is defined as $\delta^{P_T}(N_{Vz} - 1)$ where δ^{P_T} is the extra energy falling into the jet cone per additional interaction.
- C_{Abs}, "Absolute" correction, is the correction of the calorimeter response to the momentum of the particle jet.

Particle jets can be compared directly to data from other experiments or theoretical predictions. Further corrections can be applied with the aim to reconstruct the original parton moment:

$$p_T^{parton} = p_T^{particle} - C_{UE} + C_{OOC} \tag{2.9}$$

where

- C_{UE} and C_{OOC}, the "Underlying Event" and "Out-Of-Cone" corrections, correct for parton radiation and hadronization effects due to the finite size of the jet cone algorithm that is used.

However, the C_{UE} and C_{OOC} corrections are difficult to define and strongly depend on the physics and the model of the parton cascade and hadronization in the MC programs.

In the analyses presented here, the jets are corrected back to the hadron level employing the η-dependent C_η, the multiple interaction C_{MI}, and the absolute C_{Abs} corrections. These corrections increase the measured transverse energies by 10% to 30% depending on the rapidity region. The energy resolution is 15% at low jet transverse momentum and improves with increasing P_T(jet). The systematic uncertainty on the jet energy response is around 3% (1σ value) [61], depending on the transverse momentum of the jet. Figure 2.14 shows the uncertainties on the individual corrections and the total systematic uncertainty as a function of jet P_T in the central region of the calorimeter, $0.2 < |\eta| < 0.6$. For $p_T > 60$ GeV/c, the dominant contribution arises from the uncertainty on the absolute jet energy scale defined as the sum in quadrature of the different components displayed in Figure 2.15. Among them,

[6] The hadron level in the Monte Carlo generators is defined using all final-state particles with lifetime above $10^{-11}s$

the largest effect is due to the difference between data and simulation in the calorimeter response to single hadrons, varying from 1.3% to 2.5% with increasing P_T(jet). The difference in the response to electromagnetic particles (electrons and photons) gives rise to a smaller uncertainty, around 0.5% and uniform across the P_T(jet) spectrum. Uncertainties related to the particle momentum spectrum in a jet (∼1%) originate from the modeling of hadronization effects using PYTHIA and HERWIG as well as from the estimate of track reconstruction efficiencies in data and detector simulation. Finally, a 0.5% uncertainty is considered as the maximum variation of the calorimeter response across the whole data taking period.

2.3.2 Missing Transverse Energy

The missing transverse energy $\not\!\!E_T$ is defined as the norm of

$$-\sum_i E_T^i \cdot \vec{n}_i,$$

where $\vec{n}_i$ is the unit vector in the azimuthal plane that points from the beam line to the i-th calorimeter tower. Only calorimeter towers with energy above 100 MeV enter the sum. The $\not\!\!E_T$ is then corrected for the 3D primary vertex position. A further correction is applied by using the average-corrected jet transverse energies:

$$\vec{\not\!\!E}_{\rm T} = \vec{\not\!\!E}_{\rm T}^{\rm raw} - \sum_{i=1}^{N_{\rm jets}} E_{T_i}^{\rm uncorr} \cdot \vec{n}_i + \sum_{i=1}^{N_{\rm jets}} E_{T_i}^{\rm corr} \cdot \vec{n}_i$$

where $\rm N_{jets}$ is defined as the number of jets with transverse energy above 10 GeV.

Due to conservation of the transverse momentum, if the energies of all the particles produced in a collision could be collected, their projection on the transverse plane would be perfectly balanced. Significant $\not\!\!E_T$ would then arise when some particles escape the detector undetected or when their energy is mis-reconstructed. In data, only a small portion of the observed $\not\!\!E_T$ is associated with undetected particles and most of the energy unbalance is due to mismeasurement of jet energies. As previously discussed, this is caused by calorimeter non-linearities and losses in cracks and dead zones. Thus a deep understanding of the detector is necessary for a correct assessment of the $\not\!\!E_T$. Moreover, data-MC agreement on $\not\!\!E_T$ spectrum and resolution requires proper modeling of the underlying event and jet fragmentation. Several studies have been performed to assess the $\not\!\!E_T$ resolution in Run II, using minimum bias data and $Z \to \ell^+\ell^-$ data. In these samples no intrinsic $\not\!\!E_T$ is expected and the distribution of the missing transverse energy provides direct information about its resolution. This is found to be dependent on the total scalar transverse energy ΣE_T in the event, defined as

$$\sum E_T = \sum_{towers} E_i sin\theta_i$$

where the sums runs over the same calorimeter towers as for the $\not\!\!E_T$ calculation. Following the results of the studies in [62], $\not\!\!E_T$ resolution is determined to be $\simeq (0.646 \pm 0.016)\sqrt{\sum E_T}$.

2.3.3 b-Tagging Algorithms: the SecVtx Tagger

The identification of b-jets (jets whose originating parton is a b quark) is fundamental in the study of many interesting physics processes at high energy hadron colliders. In particular, it

plays a crucial role in the search for sbottom pair production described in Chapter 4 because of the heavy flavour nature of the sbottom decays. Other examples are the measurement of the top quark properties, the search for Higgs bosons, and the precision tests of QCD. The b-jets can be identified in several ways, making use of the distinguishing characteristics of B hadrons with respect to hadrons containing only lighter quarks: their long lifetime ($\sim 1.5\ ps$), large mass ($\sim 5\ \mathrm{GeV/c^2}$), and large decay fraction into leptons ($\sim 20\%$). The main b-tagging algorithms used at CDF are: the Secondary Vertex algorithm (SecVtx), the Jet Probability algorithm (JetProbability), the Soft Muon Tagger, the Soft Electron taggers, and taggers based on Neural Network technology. The b-tagging in the sbottom search is based on SecVtx and a brief description of the algorithm is provided in the following.

SecVtx looks for track vertices inside a jet displaced from the primary vertex position, making use of the long lifetime of B hadrons. Tracks lying inside the jet cone are considered: they are required to have both COT and silicon hits associated to them, and to satisfy various quality requirements. Tracks must lie within 2 cm of the primary vertex in z (to remove tracks from possible multiple interactions), and have an impact parameter significance of at least 2.5 (to remove tracks produced at the primary vertex). In order to reduce the effects of particle interactions in the detector material, tracks with an impact parameter greater than 0.15 cm are rejected. Tracks identified as coming from K_S, Λ decays, or from photon conversions are also rejected. The remaining tracks are then used to search for a vertex. Since to make a vertex at least two tracks are needed, a jet is considered *taggable* if a minimum number of two good tracks are found. The resolution on the separation of the primary and secondary vertex is typically 190 μm. The secondary vertex is required to lie on the *correct* side of the primary vertex with respect to the jet axis. Figure 2.16 shows the SecVtx reconstruction of a secondary vertex on the *right* and *wrong* side where L_{2D} is the signed 2D displacement of the vector separating the secondary and primary vertices.

Two different tunings of the SecVtx algorithm are in use, tight and loose, which have been optimized separately for high purity (tight) and high b-tagging efficiency (loose). Figure 2.18 displays the tagging efficiency for b-jets from MC events as a function of the jet energy (left) and the jet pseudorapidity (right) for both tight and loose SecVtx configurations. For tight-tag, the tag efficiency varies within 30% and 40%, depending on the jet transverse energy. The loose tagger is typically ∼20% more efficient for identifying b-jets but at the expense of a ∼200% increase in light flavor tags. In the search for direct sbottom production, the loose algorithm is used only for cross-checking the mistag estimation. More details can be found in [63].

2.3.4 Mistags

With the tracking and vertexing resolution of the CDF detector, the lifetime distribution of light flavor partons should be consistent with zero. However tracks within a light flavor jet can still have large impact parameters and hence satisfy the secondary vertex requirements. Sources of such spurious large impact parameter tracks include:

- limited detector resolution
- long-lived light particle decays (Λ, K_S)
- material interactions

Mistags due to limited detector resolution are expected to be symmetric in L_{2D}. One can then use the ensemble of negatively tagged jets ($L_{2D} < 0$) as a prediction of the light flavor jet contribution to the positive tag sample. However not all mistags are from resolution effects alone. Simply assuming that all mistagged jets are symmetric about the origin in L_{2D} will underestimate the true rate of false positive tags. The contribution from long-lived particle decays and material interactions are at strictly positive L_{2D} values, thus introducing a light flavor mistag asymmetry. Figure 2.17 shows an example of an L_{2D} distribution taken from $t\bar{t}$ MC samples. Positive values of L_{2D} are dominant for b- or c- jets while light flavor jets present both negative and positive values, with a non-negligible excess in the positive side. The probability for a given jet to be a mistag is determined from the probability that the jet is a negative tag, corrected for the negative-positive asymmetry. The number of positive and negative tags is extracted from inclusive jet samples and parametrized as a function of six kinematic variables: the transverse energy of the jet E_T, the number of good tracks matched to the jet according to the SecVtx tight-tag requirements N_{trk}, the total amount of transverse energy in the event ΣE_T, the pseudo-rapidity of the jet $|\eta(\text{jet})|$, the number of vertices per event N_{Vz}, and the primary vertex displacement along the z-axis V_Z. The parametrization coefficients obtained are collected in a multi-dimensional matrix whose binning is summarized in Table 2.2 . Figure 2.19 shows the negative and positive tag-rates

$E_T[GeV]$	N_{trk}	$\Sigma E_T[GeV]$	$\lvert\eta\rvert$	N_{Vz}	$V_Z[cm]$
0	2	0	0	1	-25
15	3	80	0.4	2	-10
22	4	140	0.8	3	10
30	5	220	1.1	4	25
40	6			6	
60	7				
90	8				
130	10				
	13				

Table 2.2: mistag matrix parametrization. The parametrization involves 6 variables: the transverse energy of the jet (E_T), the pseudo-rapidity of the jet ($|\eta|$), the SecVtx track multiplicity (N_{trk}), the number of Z vertexes (N_{Vz}), the primary vertex z-position (V_Z), and the sum of the transverse energy of all jets in the event (ΣE_T).

as a function of E_T(jet) for events selected with a JET100 trigger, the same trigger employed in the direct search for sbottom pair production and described in Chapter 4. Both tight-tag and loose-tag selection are displayed and the validity of the parameterization is tested by comparing the tag rates predicted using the mistag matrix with those observed in the data. In order to avoid statistical overlaps in the testing samples, the mistag matrix is calculated using only events with even event numbers, and then applied only to events with odd event numbers. For tight-tag, the mistag rates increases with the jet energy and reaches a plateau slightly below 1.5% for $E_T(\text{jet}) > 50$ GeV; the plateau for loose-tag is above 3%.

Several sources of uncertainties can affect the mistag rate prediction including the statistical limitation of the jet sample used to calculate the mistag matrix (1%), the dependence on the particular sample employed (6%), the effect of the trigger selection (4%), and the bias

due to the use of $\sum E_T$ for events where not all the event energy is in jets (4%). On average, the total systematic uncertainty on the estimation of the mistag rate per jet is around 8%.

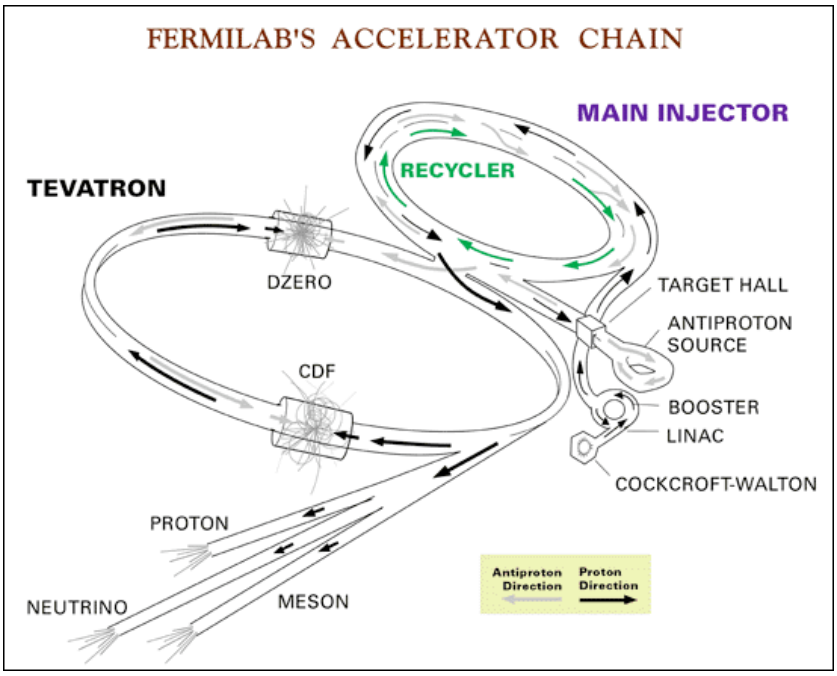

Figure 2.1: layout of the Fermilab accelerator complex.

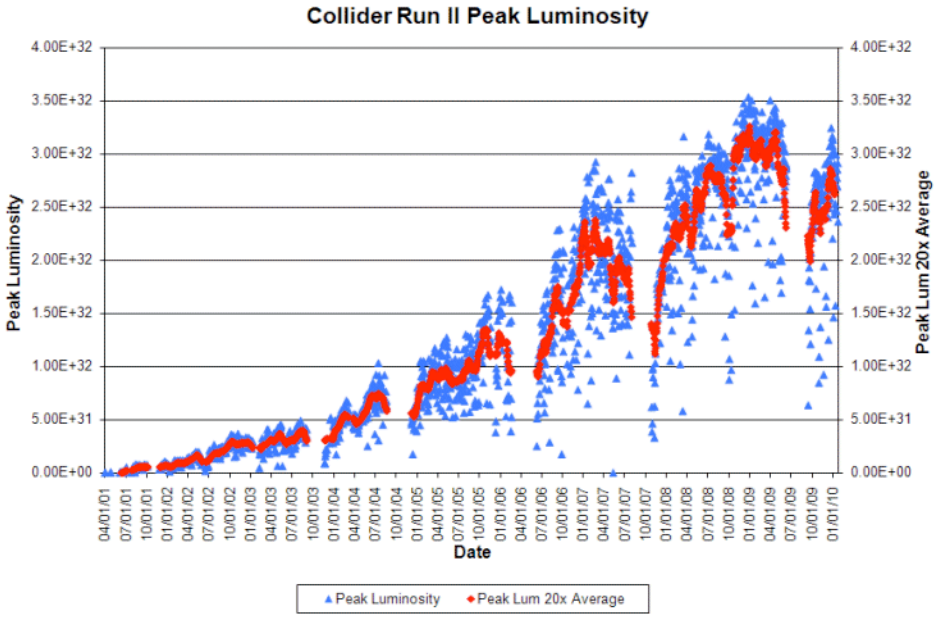

Figure 2.2: Tevatron Run II peak luminosity.

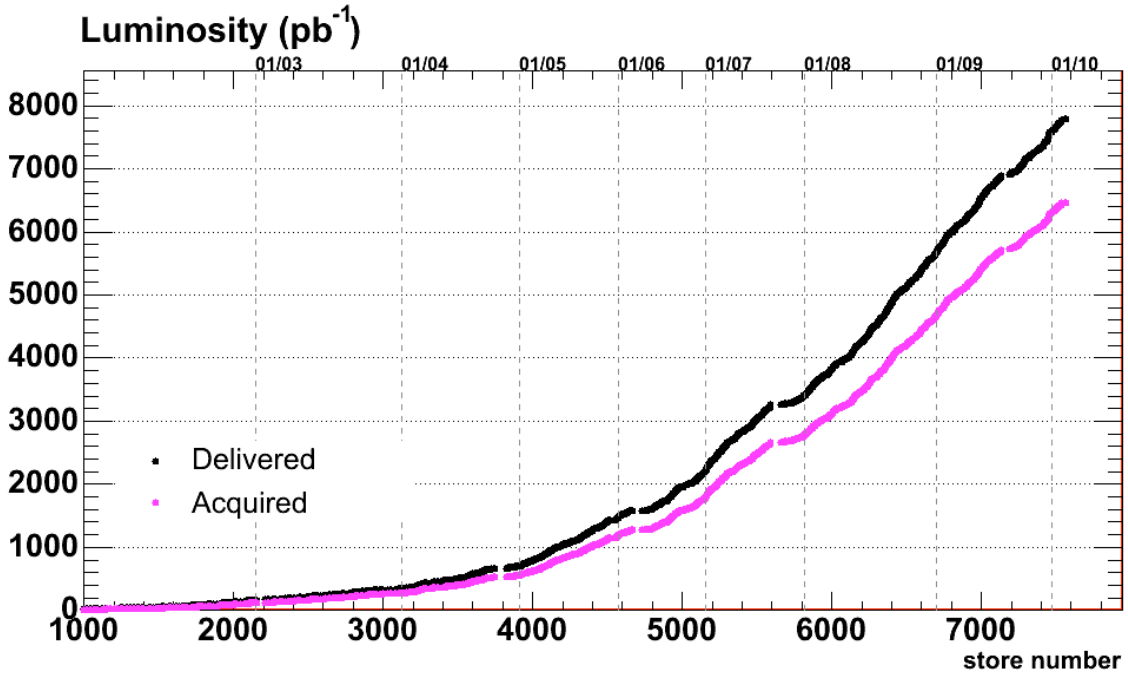

Figure 2.3: total integrated luminosity delivered by the Tevatron during Run II (black line) and correspondent total integrated luminosity recorded by the CDF experiment (purple line).

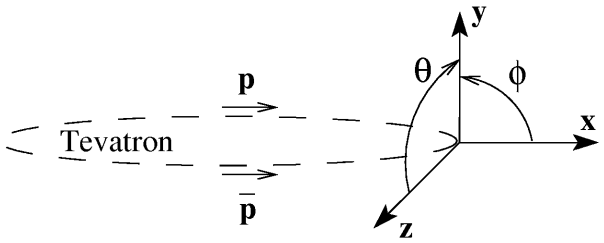

Figure 2.4: the CDF II coordinate system.

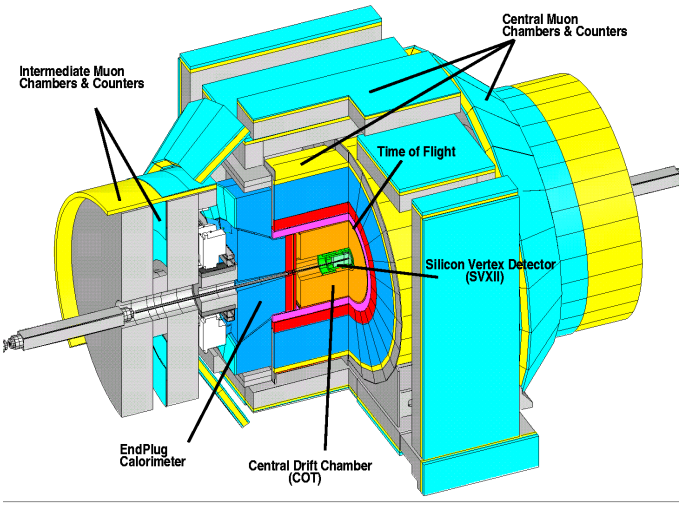

Figure 2.5: isometric view of the CDF Run II detector.

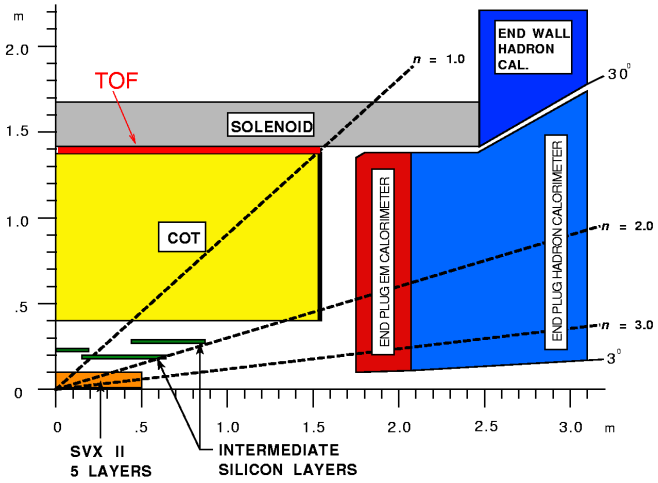

Figure 2.6: η coverage of the CDF II tracking system and calorimeters.

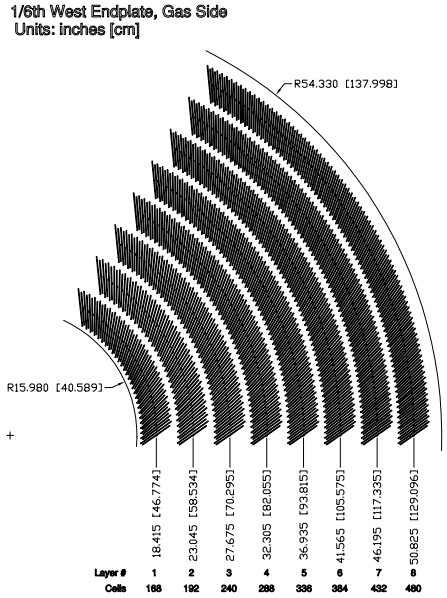

Figure 2.7: layout of wire planes on a COT end-plate.

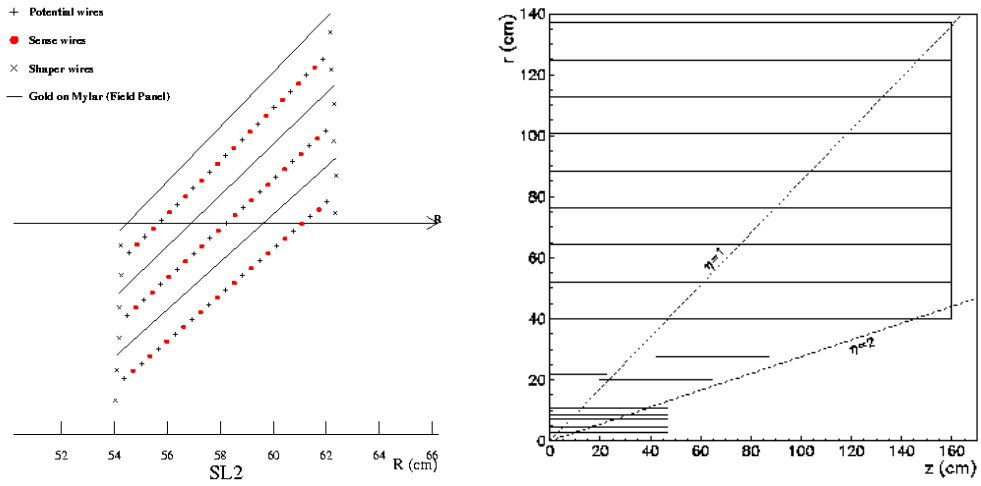

Figure 2.8: wire layout in a COT super-cell of SL2 (left) and schematic $r-z$ view of the η coverage of the inner and outer tracker, SVX II, ISL, and COT (right).

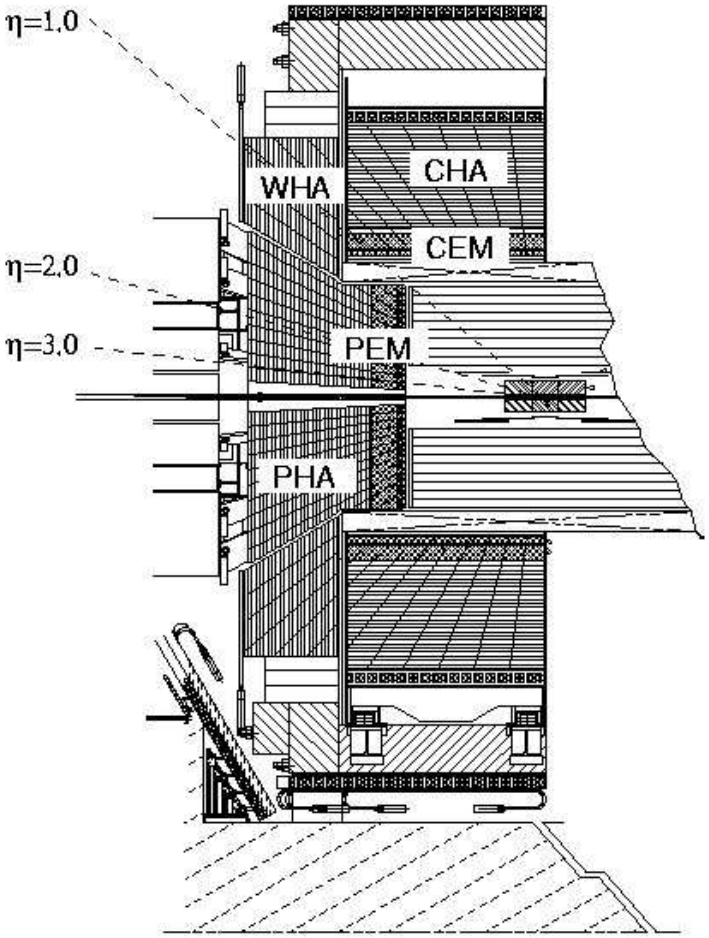

Figure 2.9: elevation view of one half of the CDF detector displaying the different components of the CDF calorimeter.

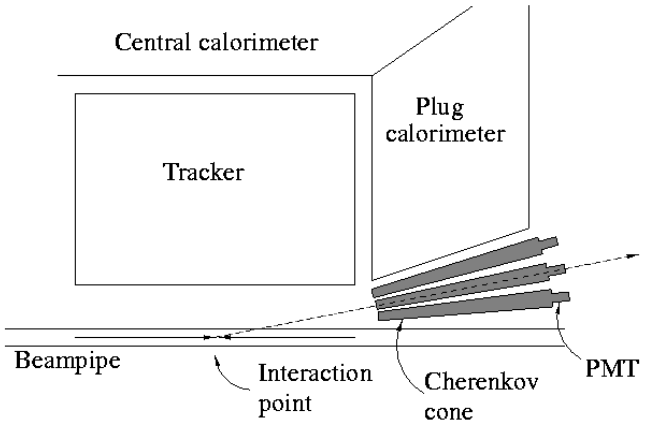

Figure 2.10: schematic view of the luminosity monitor inside a quadrant of CDF. It is located at $|\theta| < 3$.

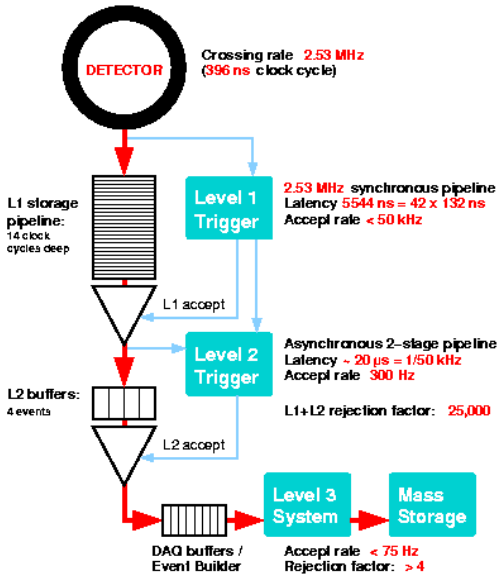

Figure 2.11: scheme of the CDF Run II Trigger and Data Acquisition System.

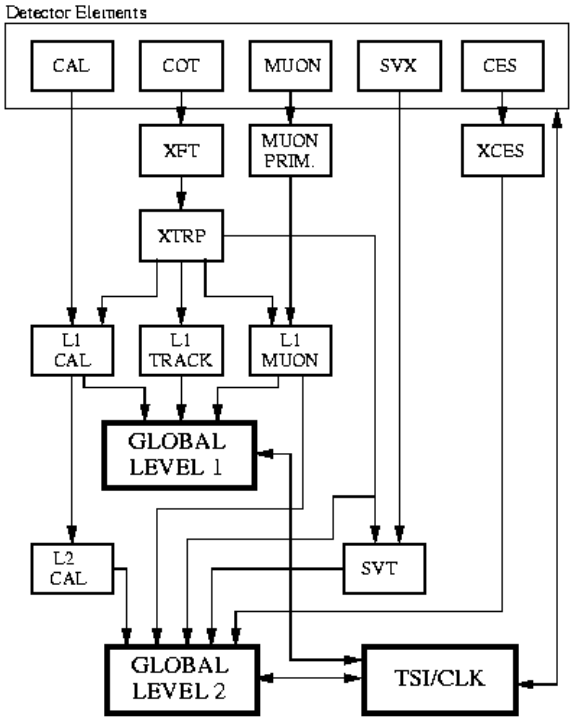

Figure 2.12: block diagram of the CDF Run II Trigger System.

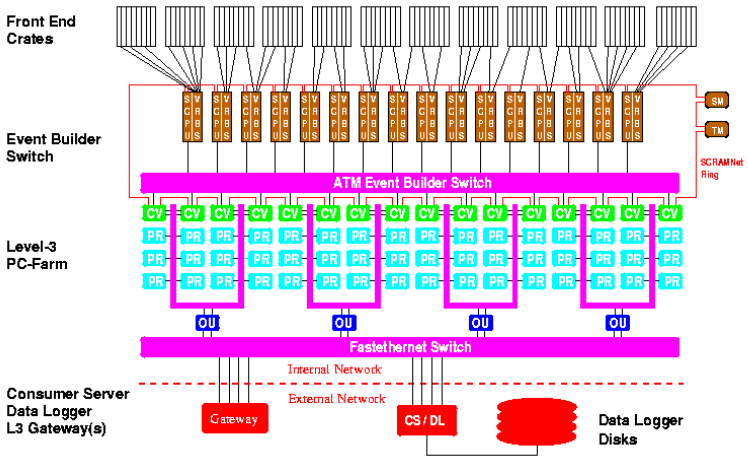

Figure 2.13: scheme of the event Builder and L3 filtering. Data from the front end crates pass through ATM switches to the converter nodes. Here, the events are assembled and passed to the processor nodes. The accepted events are passed to output nodes which send them to the Consumer Server and Data Logging systems (CS/DL).

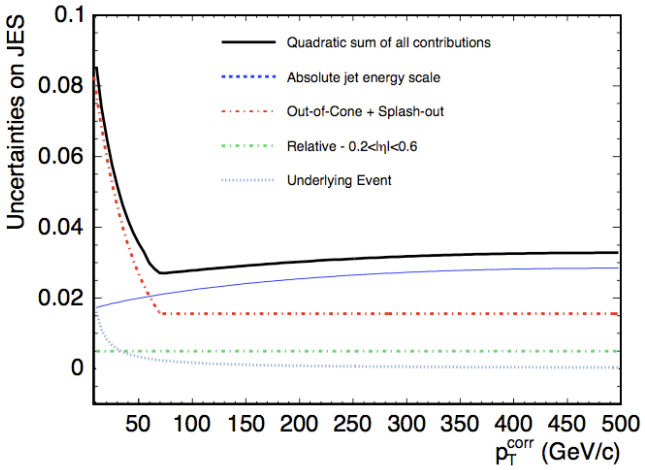

Figure 2.14: systematic uncertainties to the jet energy response as a function of the corrected P_T(jet) in the rapidity region $0.2 < |\eta| < 0.6$.

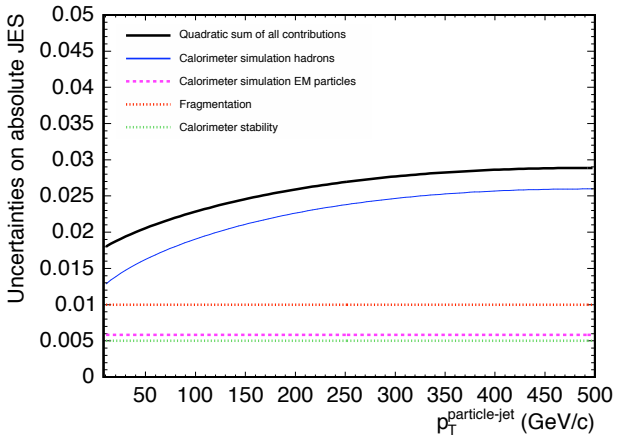

Figure 2.15: systematic uncertainty on the absolute jet energy scale due to the calorimeter calibration and simulation. The solid line shows the total uncertainty and the other lines show individual contributions.

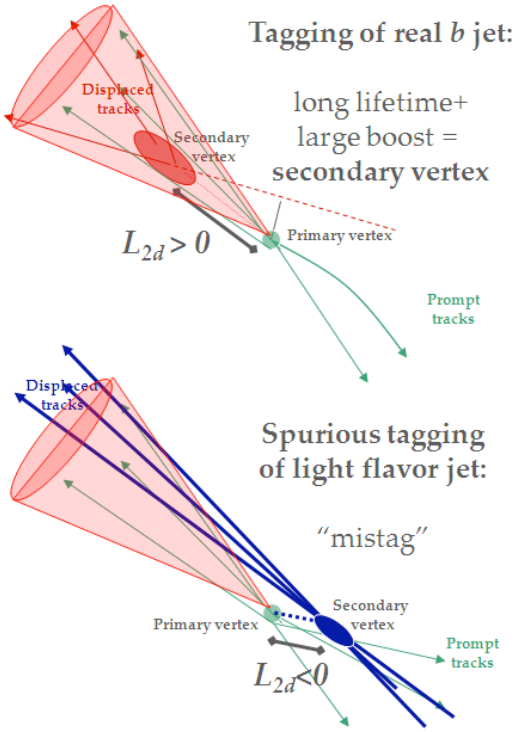

Figure 2.16: scheme of the secondary vertex reconstruction. The SecVtx algorithm searches for track vertexes inside a jet displaced from the primary vertex position, making use of the long lifetime of B hadrons. A negative tag is defined as when the identified vertex is well separated from the primary vertex, but lies on the *wrong* side of the primary vertex with respect to the jet direction.

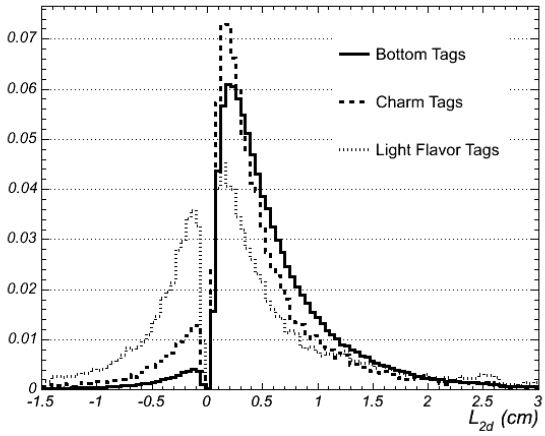

Figure 2.17: L_{2D} distribution of SecVtx-tagged jets. Distributions are taken from tt Monte Carlo.

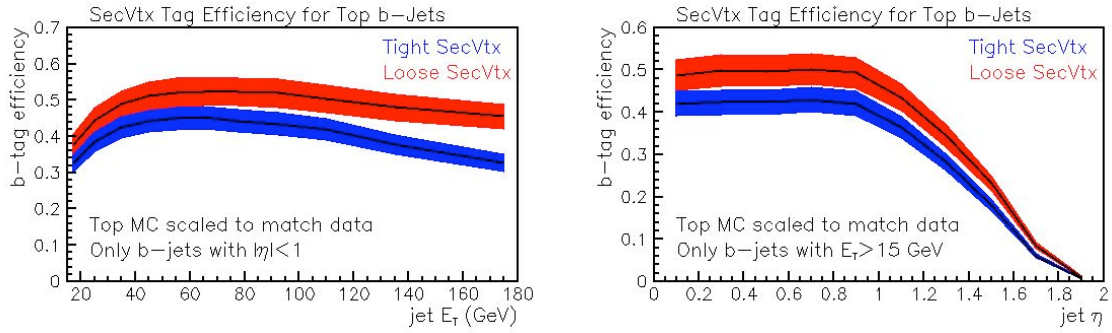

Figure 2.18: tagging efficiency for b-jets in events as a function of E_T(jet) (left) and η(jet) (right).

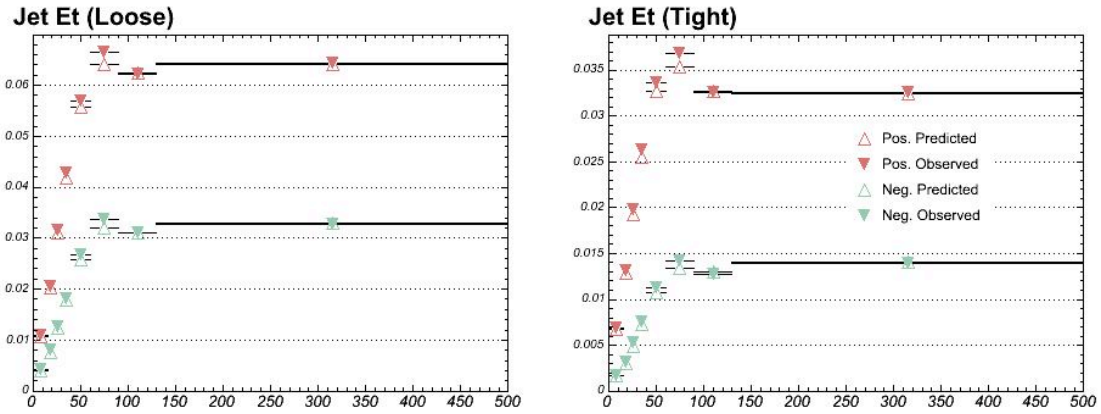

Figure 2.19: observed and predicted tag rates for the loose (left) and tight (right) SecVtx taggers as a function of E_T(jet). Events are selected with a JET100 trigger. The mistag matrix is made from events with even run number and run on odd-numbered events.

Chapter 3

Search for Gluino and Squark Production

The search is performed within the framework of minimal supergravity (mSUGRA) and assuming R-parity conservation where sparticles are produced in pairs and the LSP is stable, neutral, and weakly interacting. The expected signal is characterized by the production of multiple jets of hadrons from the cascade decays of squarks and gluinos and large missing transverse energy $\not\!\!E_T$ from the presence of two LSPs (the neutralinos $\tilde{\chi}_1^0$) in the final state. In a scenario with squark masses $M_{\tilde{q}}$ significantly larger than the gluino mass $M_{\tilde{g}}$ at least four jets in the final state are expected, while for $M_{\tilde{g}} > M_{\tilde{q}}$ dijet configurations dominate. Separate analyses are carried out for events with at least two, three, and four jets in the final state and with different requirements on the minimum $\not\!\!E_T$. The results are compared to SM background predictions from quantum chromodynamics (QCD) jets, W and Z/γ^* bosons with accompanying jets (W+jets and Z/γ^*+jets), top quark, and diboson ($WW/WZ/ZZ$) processes.

3.1 Dataset and Trigger Selection

This search is based on CDF Run II data collected between February 2002 and May 2007, corresponding to a total integrated luminosity of 2.0 fb^{-1} divided into 13 data taking periods as shown in Table 3.1.

Data are collected using a three-level trigger system that selects events with $\not\!\!E_T > 35$ GeV and at least two calorimeter clusters with E_T above 10 GeV (MET35 trigger). Table 3.2 shows in detail the trigger requirements at different levels. A change in the trigger logic has been introduced at Level 2 starting from run 195739: after this run, one of the two trigger jets has been required to be central in order to reduce beam-halo background and keep acceptable trigger rates with increasing instantaneous luminosity. This modification has no effect on the inclusive analysis since the pre-selection criteria described in Section 3.2 already requires at least a central jet per event. Starting from summer 2006, due to the improvement of the Tevatron performances and the further increase of the instantaneous luminosity, the trigger has been lumi-enabled and then dynamic prescaled. Both strategies have the purpose of avoiding the saturation of the available trigger band. In the case of the lumi-enabling, the trigger is active only with a luminosity below 190 $\times 10^{30}$ cm^{-2}s^{-1}. The

Data Period	time-range	lumi pb^{-1}
period 0	04 Feb 02 - 22 Aug 04	372
period 1	07 Dec 04 - 18 Mar 05	131
period 2	19 Mar 05 - 20 May 05	136
period 3	21 May 05 - 19 Jul 05	103
period 4	20 Jul 05 - 04 Sep 05	89
period 5	05 Sep 05 - 09 Nov 05	138
period 6	10 Nov 05 - 14 Jan 06	107
period 7	14 Jan 06 - 22 Feb 06	30
period 8	09 Jun 06 - 01 Sep 06	111
period 9	01 Sep 06 - 22 Nov 06	155
period 10	24 Nov 06 - 31 Jan 07	254
period 11	31 Jan 07 - 30 Mar 07	221
period 12	01 Apr 07 - 13 May 07	153
	tot. integr. luminosity	2000

Table 3.1: the MET35 dataset used in this analysis, divided into 13 data taking periods corresponding to a total integrated luminosity of 2.0 fb^{-1}.

Trigger Level	requirement	Prescale
L1	MET 25	1
L2	TWO-JET10 (CJET10-JET10) and L1-MET25	1
L3	MET 35	1

Table 3.2: Summary of the MET35 trigger logic used in collecting the data. In parenthesis the L2 selection after run 195721.

dynamic prescale (DPS), instead, sets the trigger prescale factor dynamically, i.e. accordingly to the instantaneous occupancy of the whole CDF trigger system. For simplicity only run sections with DPS=1 (no prescale) are considered for the inclusive search. The effect of this additional requirement is negligible: only 3 pb of data are excluded, equivalent to 0.1% of the total integrated luminosity used in the analysis.

The study of the MET35 trigger efficiency relies on events selected with high-pt muon triggers which require muons with a minimum pt in the central muon chambers and make no requirement on the calorimeter. Therefore, the high-pt muon triggers select an essentially unbiased sample with respect to the MET35 trigger selection. In addition, all pre-selection cuts described in Section 3.2 are applied to filter the events, with the exception of the minimum threshold on the $\not\!\!E_T$. Figure 3.1 presents the efficiency of the MET35 trigger path as a function of $\not\!\!E_T$. The curve reaches a plateau around $\not\!\!E_T > 70$ GeV but never comes to the 100% efficiency. After a careful investigation, this is understood in terms of saturation effect related to the measurement of the $\not\!\!E_T$ in the Level 1 trigger. In fact, the Level 1 firmware doesn't include any mechanism to protect the $\not\!\!E_T$ calculation when a trigger tower saturates. Therefore, every time this tower saturation occurs, the $\not\!\!E_T$ is miscalculated with the potential loss of high $\not\!\!E_T$ events.

A first hint of how the lost events can be recovered is visible in Figure 3.2 where the efficiency of the L1 only is shown as a function of $\not\!\!E_T$. The distribution presents clear

analogies with respect to the one involving the full trigger path in Figure 3.1 and indicates that most, if not all the event loss, is inherited from Level 1. Figure 3.3 shows the L1 efficiency and the total trigger efficiency on the $\not\!\!E_T - E_T(\text{jet}_2)$ plane, where $E_T(\text{jet}_2)$ is the transverse energy of the second leading jet. The efficiency loss concentrates in a specific region of the phase-space with very energetic jets, as expected since the saturation value for the energy deposited in a trigger tower at L1 is 128 GeV. The efficiency loss at high $E_T(\text{jet}_2)$ disappears if events with saturated towers are excluded (Figure 3.3, bottom histograms). The missing events are recovered using the JET100 dataset that selects events with the only requirement of having at least one calorimeter cluster with E_T above 100 GeV. Such requirement is fulfilled, by definition, by all the events with one or more saturated trigger towers. These events are selected and added to the MET35 dataset with the following selection criteria, implemented to avoid any double-counting:

- pass JET100 trigger
- have at least one saturated trigger tower
- do not pass L1_MET25 trigger
- pass the L2 and L3 requirements of MET35 trigger.

As a final remark, it should be noted that the miscalculation of $\not\!\!E_T$ is only a Level 1 trigger problem and does not impact neither the value of the $\not\!\!E_T$ at Level 2 and 3, nor the offline value of the $\not\!\!E_T$ used for the analysis. Moreover, with the last trigger update commissioned at the beginning of 2008 the problem was completely solved.

3.2 Event Pre-Selection

The events selected with the MET35 trigger are then required to have a primary vertex with a z position within 60 cm of the nominal interaction. Jets are reconstructed from the energy deposits in the calorimeter towers using a cone-based jet algorithm with cone radius R = 0.7, and the measured $E_T(\text{jet})$ is corrected for detector effects and contributions from multiple $p\bar{p}$ interactions per crossing at high instantaneous luminosity, as discussed in Section 2.3.1. The events are required to have at least two, three, or four jets (depending on the final state considered), each jet with corrected transverse energy $E_T(\text{jet}) > 25$ GeV and pseudo-rapidity in the range $|\eta(\text{jet})| < 2.0$, and at least one of the jets is required to be central ($|\eta(\text{jet})| < 1.1$). Finally, the events are required to have $\not\!\!E_T > 70$ GeV. As described in the previous Section, for the kinematic range in $\not\!\!E_T$ and the E_T of the jets considered in this analysis, the trigger selection is 100% efficient.

Beam-related backgrounds and cosmic rays are removed by requiring an average jet electromagnetic fraction EEMF$\geq$ 0.15 with the EEMF variable defined as:

$$\text{EEMF} = \frac{\sum_{\text{jets}} E_T(\text{jet}) \cdot f_{emf}^{jet}}{\sum_{\text{jets}} E_T(\text{jet})}, \tag{3.1}$$

where f_{emf}^{jet} is the fraction of the electromagnetic component of the jet transverse energy and the sum is performed over the leading jets of the event. In addition, the events are required to have an average charged particle fraction ECHF$\geq$ 0.15. ECHF is defined for central jets

as the averaged ratio between the momentum of the jet, computed using tracks, and the jet transverse energy:

$$\text{ECHF} = \frac{1}{N_{\text{jets}}} \sum_{\text{jets}} \frac{\sum_{\text{tracks}} P_T^{\text{track}}}{E_T(\text{jet})}, \text{ with } |\eta(\text{jet})| < 1.1 \tag{3.2}$$

where only tracks in a cone of radius 0.4 around the jet's direction, and passing the quality cuts in Table 3.3 are considered. The requirements on EEMF and ECHF reject events with anomalous energy deposition in the hadronic section of the calorimeter or energy deposits in the calorimeter inconsistent with the observed activity in the tracking system, and have no significant effect on the mSUGRA and SM Monte Carlo samples.

Track Quality Requirements
$\lvert z - z_0 \rvert < 2$ cm
$0.3 < p_T < 500$ GeV/c
$\lvert\eta\rvert < 1.5$
$d_0 < 2$ cm
Number of axial + stereo hits > 20

Table 3.3: summary of the quality requirements for tracks to be used in the calculation of the ECHF and in the definition of track isolation.

Summary of pre-selection cuts

All the pre-selection cuts are summarized as follows:

- $|V_z| < 60$ cm .
- $N_{jets} \geq 2, 3, 4$.
- $E_T(\text{jet}) \geq 25$ GeV and $|\eta(\text{jet})| < 2.0$.
- At least one of the leading jets with $|\eta(\text{jet})| < 1.1$.
- EEMF ≥ 0.15 .
- ECHF ≥ 0.15 .
- $\not\!\!E_T > 70$ GeV .

3.3 The mSUGRA Signal

The mSUGRA samples are generated using the ISASUGRA implementation in PYTHIA with $A_0 = 0$, sign(μ) $= -1$, and tan$\beta = 5$, as inspired by previous studies [64]. A total of 132 different squark and gluino masses are generated via variations of M_0 and $M_{1/2}$ in the range $M_0 < 600$ GeV/c^2 and $50 < M_{1/2} < 220$ GeV/c^2. The correspondent samples on the $M_0 - M_{1/2}$ plane are in Figure 3.4. At low tanβ, the squarks from the first two generations are

nearly degenerate, whereas the mixing of the third generation leads to slightly lighter sbottom masses and much lighter stop masses. In this analysis, stop pair production processes are not considered. The contribution from hard processes involving sbottom production is almost negligible, and is not included in the calculation of the signal efficiencies to avoid a dependency on the details of the model for squark mixing. The mSUGRA samples are normalized using NLO cross sections as determined by PROSPINO, with input parameters provided by Isajet. CTEQ61M parton distribution functions (PDFs) are used, and renormalization and factorization scales are set to the average mass of the sparticles produced in the hard interaction.

3.4 The SM Background

Sources of SM background for this analysis comprise QCD multijet events, W and Z/γ^* boson decays in association with jets, top quark and diboson (WW, WZ, and ZZ) processes. Other sources of background such as $W/Z + \gamma$ processes are negligible. Among all the SM backgrounds, the contribution from Z/γ^* and W decays with final state neutrinos constitutes an irreducible contamination to the mSUGRA signal. In the other cases the $\not\!\!E_T$ can be due to undetected leptons or mis-measured jet energies.

Samples of simulated QCD-jets, $t\bar{t}$ production, and diboson processes are generated using the PYTHIA Monte Carlo generator with Tune A. The normalization of the QCD-jets sample is extracted from data in a low $\not\!\!E_T$ region, while $t\bar{t}$ and diboson samples are normalized to next-to-leading order (NLO) predictions. Samples of simulated Z/γ^*+jets and W+jets events are generated using the ALPGEN program where exclusive subsamples with different jet multiplicities are combined, and the resulting samples are normalized to the measured Z and W inclusive cross sections. Finally, samples of single top events are produced using the MadEvent program and normalized using NLO predictions. Further details on the MC generation for SM processes are in Section 1.5.

3.5 Selection Cuts

The reduction of the SM backgrounds is the real challenge of the analysis and a number of selection cuts is applied to reject specific contributions.

Rejection of multijet QCD background

The dominant QCD-jets background with large $\not\!\!E_T$ originates from the mis-reconstruction of the jet energies in the calorimeters. In such events the $\not\!\!E_T$ direction tends to be aligned, in the transverse plane, with one of the leading jets in the event. This background contribution is suppressed by requiring an azimuthal separation $\Delta\phi(\not\!\!E_T - \text{jet}) > 0.7$ for each of the selected jets in the event. In the case of the 4-jets analysis, the requirement for the least energetic jet is limited to $\Delta\phi(\not\!\!E_T - \text{jet}) < 0.3$. Finally, in the 2-jets analysis case the events are rejected if they contain a third jet with $E_T > 25$ GeV, $|\eta| < 2.0$, and $\Delta\phi(\not\!\!E_T - \text{jet}) < 0.2$.

Electron Veto

W and Z/γ^* bosons and top quarks decay a fraction of the times into energetic electrons. To reject this contribution, the electromagnetic fraction of the transverse energy of each of the leading jets (f_{emf}^{jet}) is required to be

$$\mathrm{f_{emf}^{jet}} < 0.9. \tag{3.3}$$

Muon/Tau Veto

W and Z/γ^* bosons can also decay into muons or taus that can produce large energy imbalance in the calorimeter and contribute significantly to the total background yield. Muons and taus can be identified in the COT as isolated tracks. A track is considered isolated if the scalar sum $\mathrm{p_T}$ of all additional tracks in a cone of radius, R = 0.4, is less than 2 GeV/c where only tracks passing the quality requirements in Table 3.3 are considered. With the above definitions two different cuts are implemented to reject muon/tau contamination:

- events are rejected if the invariant mass of the two highest isolated tracks falls in $76 < \mathrm{M_{inv}} < 106$ mass window.
- events are rejected if the azimuthal angle between the highest isolated track and the $\not\!\!E_T$ is below 0.7. This cut is analogous to the cut for QCD rejection as it eliminates events where most of the $\not\!\!E_T$ is caused by an undetected muon/tau.

3.5.1 Optimization and Definition of Signal Regions

The cuts described in the previous Section are introduced to reduce specific background processes and are not optimized to enhance the SUSY signal against the remaining background. The mSUGRA signal events are characterized by isotropic (spherical) final-state topologies with large amounts of transverse energy measured in the calorimeter. Based on this consideration, three different variables are chosen to discriminate signal from background: the $\not\!\!E_T$, the transverse energies of the leading jets E_T(jets), and the sum of the energies of the leading jets $H_T = \sum_{\mathrm{jets}} E_T(\mathrm{jet})$. For each mSUGRA sample, the procedure maximizes $S/\sqrt{B}$, where S denotes the number of SUSY events and B is the total SM background. The cuts are optimized with a step-by-step procedure where the threshold on one variable at a time is studied. The final value of the energy thresholds are defined for each analysis and do not depend on the order the optimization is performed. Figure 3.5 (top) shows few examples of the $S/\sqrt{B}$ scanning as a function of the H_T and $\not\!\!E_T$ for one representative mSUGRA point with $\mathrm{M_{\tilde{q}}} \simeq \mathrm{M_{\tilde{g}}} \simeq 340$ GeV/c^2. Similar tests are performed with the transverse energies of the three leading jets. 2-D scans of $S/\sqrt{B}$ are also performed as consistency checks to evaluate the correlation between the different variables. An example of a 2-D scan on the $\not\!\!E_T$-H_T plane is in Figure 3.5 (bottom), while Table 3.4 summarizes the thresholds applied on the relevant variables according to the three different analyses.

The results from the different mSUGRA samples are then combined to define, for each final state, a single set of lower thresholds that maximizes the search sensitivity in the widest range of squark and gluino masses (see Table 3.4). As an example, for $\mathrm{M_{\tilde{q}}} \simeq \mathrm{M_{\tilde{g}}}$ and masses between 300 GeV/c^2 and 400 GeV/c^2, values for $S/\sqrt{B}$ in the range between 20 and 6 are obtained, corresponding to SUSY selection efficiencies of 4% to 12%, respectively.

[GeV]	4-jet	3-jet	2-jet
H_T	280	330	330
$\not\!\!E_T$	90	120	180
$E_T(\text{jet}_1)$	95	140	165
$E_T(\text{jet}_2)$	55	100	100
$E_T(\text{jet}_3)$	55	25	–
$E_T(\text{jet}_4)$	25	–	–

Table 3.4: definition of the signal regions for the three analyses with the summary of the optimized cuts.

3.6 Systematic Uncertainties

Systematics for expected SM backgrounds

The total systematic uncertainty on the SM estimation is a combination of the different contributions described below and summarized in Table 3.5.

- **Energy scale**: $\pm 1\sigma$ variations in the jet energy corrections are considered to account for the uncertainty on the jet energy scale. The corresponding shift in the $\not\!\!E_T$ is also included. This translates into an uncertainty on the background estimation that varies between 20% to 25% depending on the signal region considered.

- **QCD Multijet Background** As it was previously discussed, data is used to normalize the QCD Monte Carlo predictions in a region where no SUSY signal is expected. The statistical precision of the normalization of the QCD control sample is much better that 1% and considered negligible. The uncertainty on the QCD normalization is therefore totally dominated by the uncertainty on the absolute energy-scale determination. Inclusive cross section measurements [65] indicate that JES uncertainties already cover all possible deviations of the NLO pQCD predictions from the nominal data.

- **Top Production**: The top cross section uncertainty due to PDFs is taken directly from the theoretical calculation[38] and is about 10%. The uncertainty on the cross section due to the renormalization/factorization scale is negligible. Top Monte Carlo samples are produced with modified (high/low) ISR and FSR, which translates into a variation between 1% and 7% on the top background estimation, depending on the signal region.

- **Boson+jets Production**: As in the case of QCD Monte Carlo samples, the boson+jets samples are normalized to the measured inclusive Drell-Yan cross sections: we consider 1.94% and 2.2% systematic uncertainties for W and Z/γ^* cross section respectively, resulting from the sum in quadrature of statistical and systematic uncertainties as quoted in [37]. In addition, a $\pm 10\%$ effect is considered as uncertainty due to the modeling of the ISR and FSR in the MC. Remaining uncertainties on the total Boson+jets backgrounds are due to the absolute energy scale determination.

- **Diboson Production**: The diboson uncertainty due to the uncertainty on the PDF and the renormalization scale is taken from the theoretical calculation [37] and is about 10%. An additional 10% accounts for the uncertainty due to the choice of nominal value for the ISR/FSR in MC samples.

Region	JES	$\mathcal{L}$	Ren.⊕PDF	ISR/FSR	**Total**
2-jet	4.057	0.95	0.6648	2.147	4.734
(w.r.t nominal eff.)	25.62%	6%	4.199%	13.56%	30.05%
3-jet	10.8	2.224	1.699	4.544	12.05
(w.r.t nominal eff.)	29.14%	6%	4.582%	12.26%	32.36%
4-jet	16.02	2.873	1.787	2.841	16.62
(w.r.t nominal eff.)	33.45%	6%	3.732%	5.932%	34.61%

Table 3.5: systematic uncertainties on the background expected number of events for the three signal regions, in number of events and w.r.t. the total background expectations.

Signal

As for the SM background, the total systematic uncertainty on the estimation of the mSUGRA yields is a combination of different effects as listed below. Table 3.6 displays their relative contributions and the total systematic uncertainty for three representative signal points.

- **Energy scale**: $\pm 1\sigma$ variations in the jet energy corrections are considered to account for the uncertainty on the jet energy scale. The corresponding shift in the $\not{E}_T$ is also included. This translates into an uncertainty on the signal efficiency that varies between 10 to 15 % compared to the nominal efficiencies.

- **ISR/FSR**: systematic uncertainty on the expected signal events related to the modeling of the initial and final state radiation in the Monte Carlo are considered. For each point in the mSUGRA mass plane, additional samples are generated with modified amount of initial and final state radiation with respect to the nominal value. This translates into an uncertainty on the signal efficiency that varies between 3% to 5% compared to the nominal efficiencies.

- **Renormalization scale**: The default value of the renormalization scale in PROSPINO is set as explained in Section 1.5.3. To investigate the effects from a variation of the renormalization scale on the PROSPINO cross section the value of μ is set to $\mu * 2$ and $\mu/2$. The uncertainty on the cross section varies between 17% and 23%, depending on the mSUGRA point.

- **PDF**: the Hessian method [27] is employed to calculate the uncertainty on the theoretical cross section due to the choice of the PDFs. According to the prescription of the CTEQ group, the 1σ up/down variation of the PDFs parameters leads to a new set of 40 different PDFs (20 for $+1\sigma$, 20 for $-\sigma$). Different cross sections are computed using each of the 40 PDFs and the uncertainty associated with the PDF uncertainty is computed following this procedure:

– For each eigenvalue we check if the +1 σ and -1 σ variations of the eigenvalue have produced a positive and negative shift respectively. If that is the case, then the positive and negative systematic uncertainties are given by the following formula: $\mathrm{d}X_{\pm}^2 = \sum_i^{20}(X_{\pm}^i - X_{\mathrm{CTEQ6.1M}})^2$. Here, X is the quantity you are interested in.

– If the +1 σ and -1 σ PDFs for a given eigenvalue result on just a positive shift with respect to the nominal value, only the largest uncertainty contributes to $\mathrm{d}X_+$. There is no contribution to $\mathrm{d}X_-$ from this eigenvalue.

– If the +1 σ and -1 σ PDFs for a given eigenvalue result on just a negative shift with respect to the nominal value, only the largest uncertainty contributes to $\mathrm{d}X_-$. There is no contribution to $\mathrm{d}X_+$ from this eigenvalue.

This translates into an uncertainty on the theoretical cross section that varies between 20 and 34 %, depending on the mSUGRA point. Following CTEQ group indications, we consider that the PDF variations correspond to a 90% confidence level (CL) and the resulting uncertainties are scaled down by a factor 1.64.

Region	Samples	JES	$\mathcal{L}$	Ren.⊕PDF	ISR/FSR	**Total**
2-jet	$M_{\tilde{q}}$=366.9 $M_{\tilde{g}}$=406.4	1.406%	0.49%	0.08997%	0.3991%	1.544%
	(w.r.t nominal eff.)	17.21%	6%	1.102%	4.886%	18.91%
3-jet	$M_{\tilde{q}}$=360.2 $M_{\tilde{g}}$=346	1.193%	0.4778%	0.3163%	0.2124%	1.341%
	(w.r.t nominal eff.)	14.99%	6%	3.973%	2.667%	16.84%
4-jet	$M_{\tilde{q}}$=463.3 $M_{\tilde{g}}$=288.7	0.8319%	0.317%	0.2797%	0.3241%	0.9879%
	(w.r.t nominal eff.)	15.75%	6%	5.294%	6.135%	18.7%

Table 3.6: systematic uncertainties on the selection efficiency for some mSUGRA signal samples representative of the 2-, 3-, and 4-jet analyses. The upper numbers are the absolute uncertainties on the efficiencies, and the lower numbers the relative variation to the nominal efficiency values.

3.7 Control Regions

A number of control samples in data are considered to test the validity of the SM background predictions, as extracted from simulated events. The samples are defined by reversing the logic of some of the selection criteria described above. Three different types of control regions are identified:

- *QCD-dominated region*: at least one of the leading jets is required to be aligned with the $\not\!\!E_T$. This corresponds to reverting the QCD rejection cut and the resulting sample is dominated by QCD with negligible contamination from other background sources. Figure 3.6 shows the comparison between data and MC along $\not\!\!E_T$ and H_T spectra in the QCD enhanced region for the three different analyses.

- *EWK/Top-dominated region (muons/taus)*: since muons and taus are identified via the presence of isolated tracks, a muon/tau-enriched sample is selected by requiring one isolated track in the event to be along the $\not\!\!E_T$ direction ($\Delta\phi(\mathrm{trk}, \not\!\!E_{\mathrm{T}})$ <0.7), or two isolated tracks with invariant mass in the Z mass window range (76 < M(inv) < 106

GeV/c^2). The $\not\!\!E_T$ and H_T distributions of MC events in this muon dominated control region are compared to data in Figure 3.7.

- *EWK/Top-dominated region (electrons)*: electron vetoes are reversed with at least one of the leading jets required to have a high electromagnetic fraction EMF > 0.9. Most of the events selected with this requirement have a high probability of containing at least one electron in the final state. Therefore, this sample is dominated by electroweak processes such as W and Z/γ^* bosons or t quarks decaying into electrons and jets. Figure 3.8 shows the $\not\!\!E_T$ and H_T distributions for both data and MC in the electron dominated control region.

An additional control sample is defined by applying all the 2-jet analysis final cuts, but releasing the final threshold on both $\not\!\!E_T$ and H_T. Such N-2 distributions are shown in Figure 3.9.

Data and MC are in good agreement within the systematic uncertainties in all the control regions and MC samples give a reliable description of the SM expectation in the kinematic region of interest.

3.8 Results

Figure 3.10 shows the measured H_T and $\not\!\!E_T$ distributions compared to the SM predictions after all final selection criteria are applied. For illustrative purposes, the Figure indicates the impact of a given mSUGRA scenario. The measured distributions are in good agreement with the SM predictions in each of the three final states considered. In Table 3.7, the observed number of events and the SM predictions are presented for each final state. A global χ^2 test, including correlations between systematic uncertainties, gives a 94% probability.

Table 3.8 lists the relative contributions of all the different SM backgrounds after the final selections. In the 2-jet analysis, the dominant contribution to the total background comes from W+jets decays, while QCD is the most important contamination in the 3-jet analysis. Finally, top decays are the main background in the 4-jet signal region.

Events in 2.0 fb^{-1}	Observed	**Total + systematics**
4-jet	45	48 ± 17
3-jet	38	37 ± 12
2-jet	18	16 ± 5

Table 3.7: observed number of events for the for the 2-, 3-, and 4-jet analyses in 2.0 fb^{-1} of CDF II data, compared with the expected number of events for the SM Background.

3.9 Exclusion Limit

Since no significant deviation from the SM prediction is observed, the results are translated into 95% CL upper limits on the cross section for squark and gluino production in different regions of the squark-gluino mass plane, using a Bayesian approach [67] and including statistical and systematic uncertainties as described in Appendix B. For the latter, correlations

samples	2-jet	3-jet	4-jet
QCD	4.37±2.01	13.34±4.67	15.26±7.60
top	1.35±1.22	7.56±3.85	22.14±7.29
$Z/\gamma^* \to \nu\nu$+jets	3.95±1.09	5.39±1.74	2.74±0.95
$Z/\gamma^* \to ll$+jets	0.09±0.04	0.16±0.11	0.14±0.08
$W \to l\nu$+jets	6.08±2.15	10.69±3.84	7.68±2.85
WW/WZ/ZZ	0.21±0.19	0.35±0.17	0.49±0.34
tot SM	16±5	37±12	48±17

Table 3.8: relative contributions of the individual SM background processes estimated from Monte Carlo for the 2-, 3-, and 4-jet analyses. Correspondent systematic uncertainties are also indicated.

between systematic uncertainties on signal efficiencies and background predictions are taken into account, and an additional 6% uncertainty on the total luminosity is included. For each mSUGRA point considered, observed and expected limits are computed separately for each of the three analyses. For each of the mSUGRA points in the squark-gluino mass plane, the selection providing the best expected limit is used for the nominal result. Figure 3.11 shows the observed and expected 95% C.L. upper limits as a function of squark and gluino masses, compared to mSUGRA predictions, in four regions within the squark-gluino mass plane. Cross sections in the range between 0.1 pb and 1 pb are excluded by this analysis, depending on the masses considered. The observed numbers of events in data are also translated into 95% CL lower limits for squark and gluino masses, for which the uncertainties on the theoretical cross sections are included in the limit calculation, and where the three analyses are combined in a similar way as for the cross section limits. The excluded region in the squark-gluino mass plane is shown in Figure 3.12. In a mSUGRA scenario with $A_0 = 0$, sign(μ) $= -1$, and tan$\beta = 5$, this search excludes masses up to 392 GeV/c^2 at 95% CL in the region where gluino and squark masses are similar, gluino masses up to 280 GeV/c^2 for any squark mass, and gluino masses up to 423 GeV/c^2 for squark masses below 378 GeV/c^2. As shown in Figure 3.12, our limit significantly extends the exclusion region from Tevatron Run I, as well as indirect limits from LEP. The results of this search are compatible with the latest results from the DØ Collaboration [73] excluding masses up to 392 GeV/c^2 when gluinos and squark are mass degenerate, and gluino masses up to 327 GeV/c^2 for any squark mass. At the time of writing this document, the combination of CDF and DØ results into a Tevatron Run II exclusion limit is on going. The limits on $M_{\tilde{g}}$ and $M_{\tilde{q}}$ can be translated into limits on the M_0 and $M_{1/2}$ mSUGRA parameters at the GUT scale. Figure 3.13 shows the excluded regions in the M_0-$M_{1/2}$ plane for tan$\beta = 5$, $A_0 = 0$, and sign(μ) $= -1$. This search improves the limits from indirect searches as determined by LEP2 [72] for M_0 values between 75 and 250 GeV/c^2 and for $M_{1/2}$ values between 130 and 170 GeV/c^2.

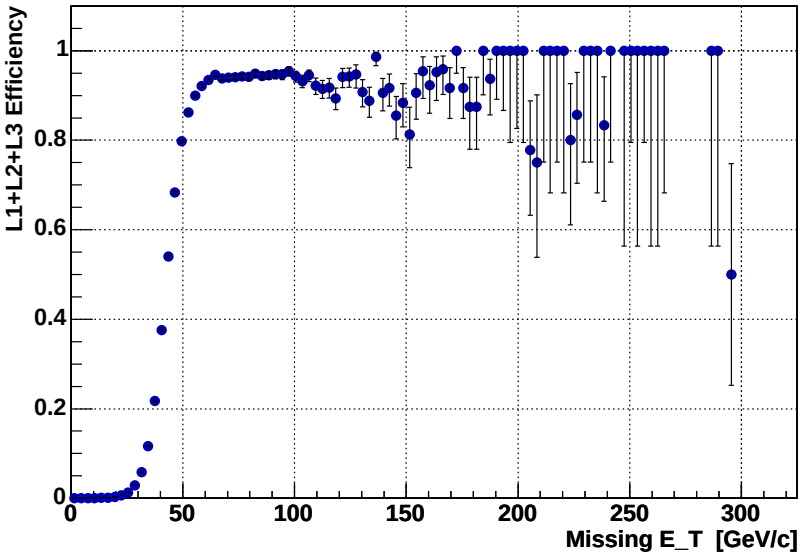

Figure 3.1: total MET35 trigger efficiency as a function of corrected $\not\!\!E_T$.

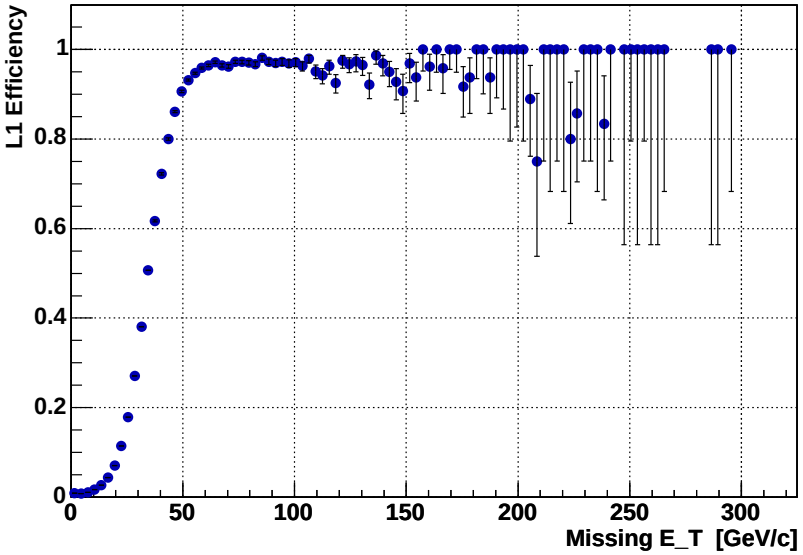

Figure 3.2: level 1 trigger efficiency as a function of corrected $\not\!\!E_T$.

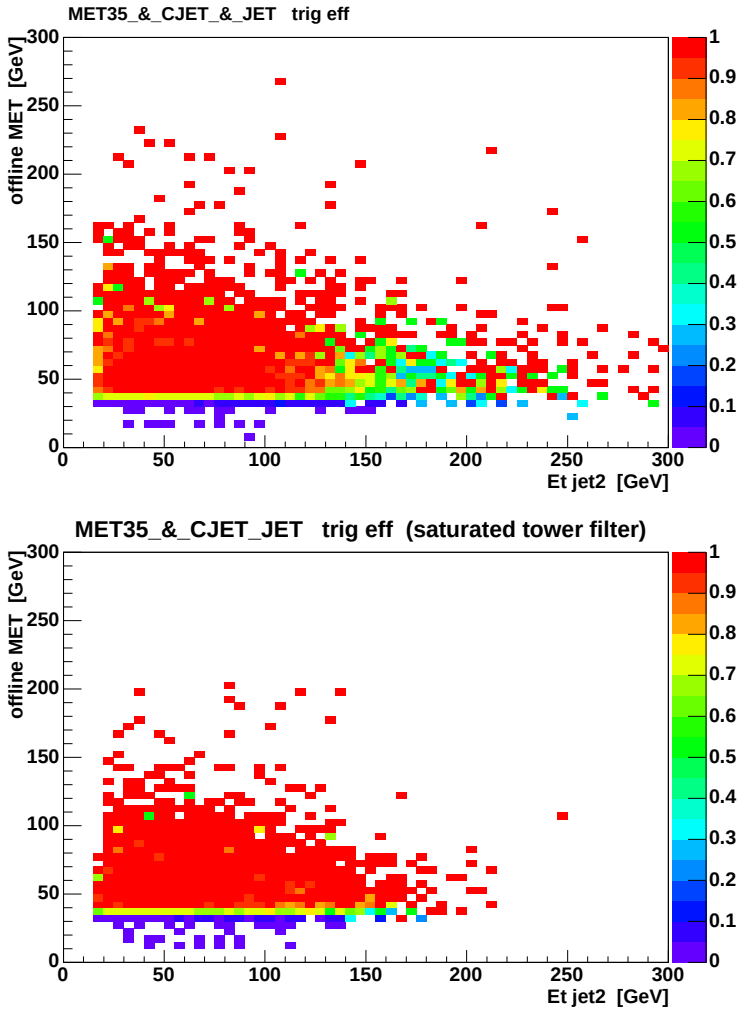

Figure 3.3: MET35 trigger efficiency on the offline $\not\!\!E_T$ - $E_T(\text{jet}_2)$ plane. top: trigger efficiency for the whole CMUP18 sample; bottom: filter on saturated tower applied.

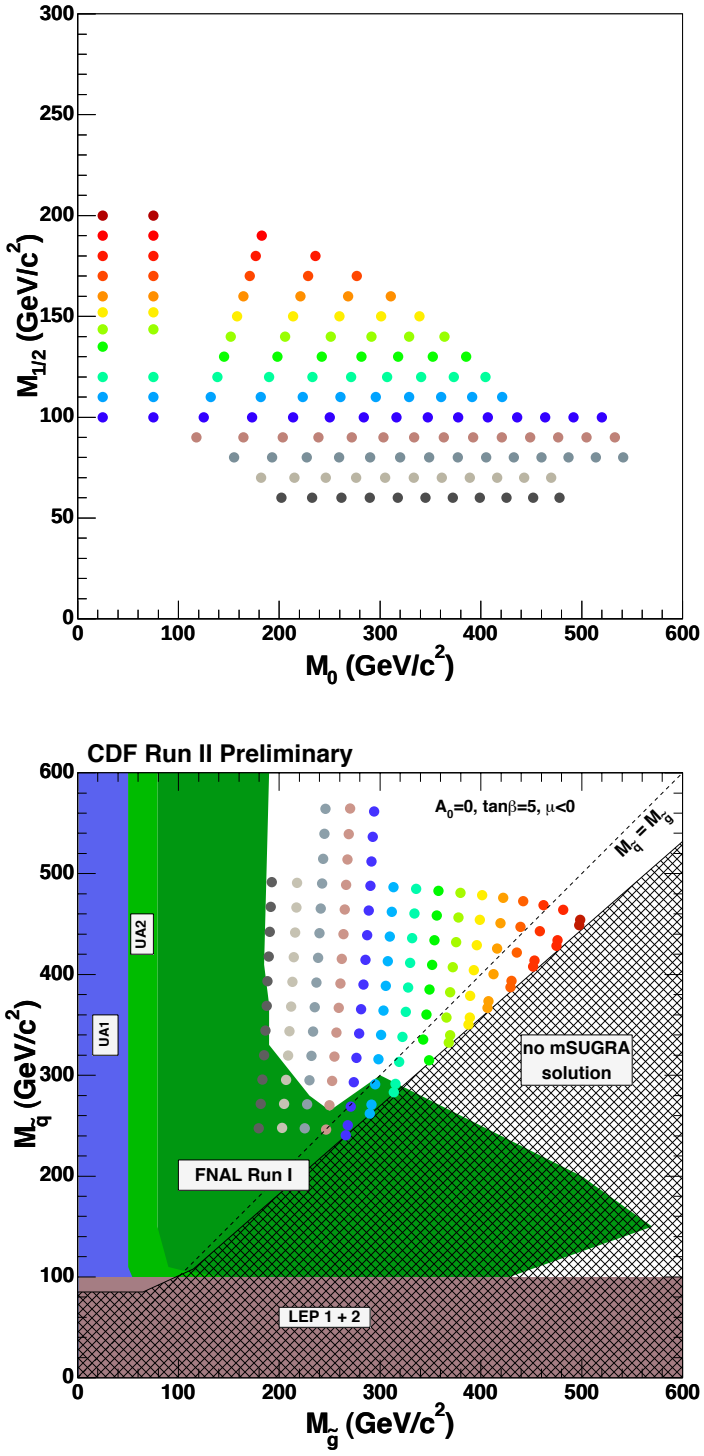

Figure 3.4: Top: representation of mSUGRA points generated with PYTHIA. The x-axis and y-axis correspond to M_0 and $M_{1/2}$ mSUGRA parameters respectively. Bottom: representation of the mSUGRA points generated with PYTHIA. The y-axis is the average pole mass of the 8 squarks of the first two generations. The x-axis corresponds to the mass of the gluino. Limits from previous analyses are shown for comparison. In the dashed region the RGE equation have no solution and the mSUGRA model is forbidden.

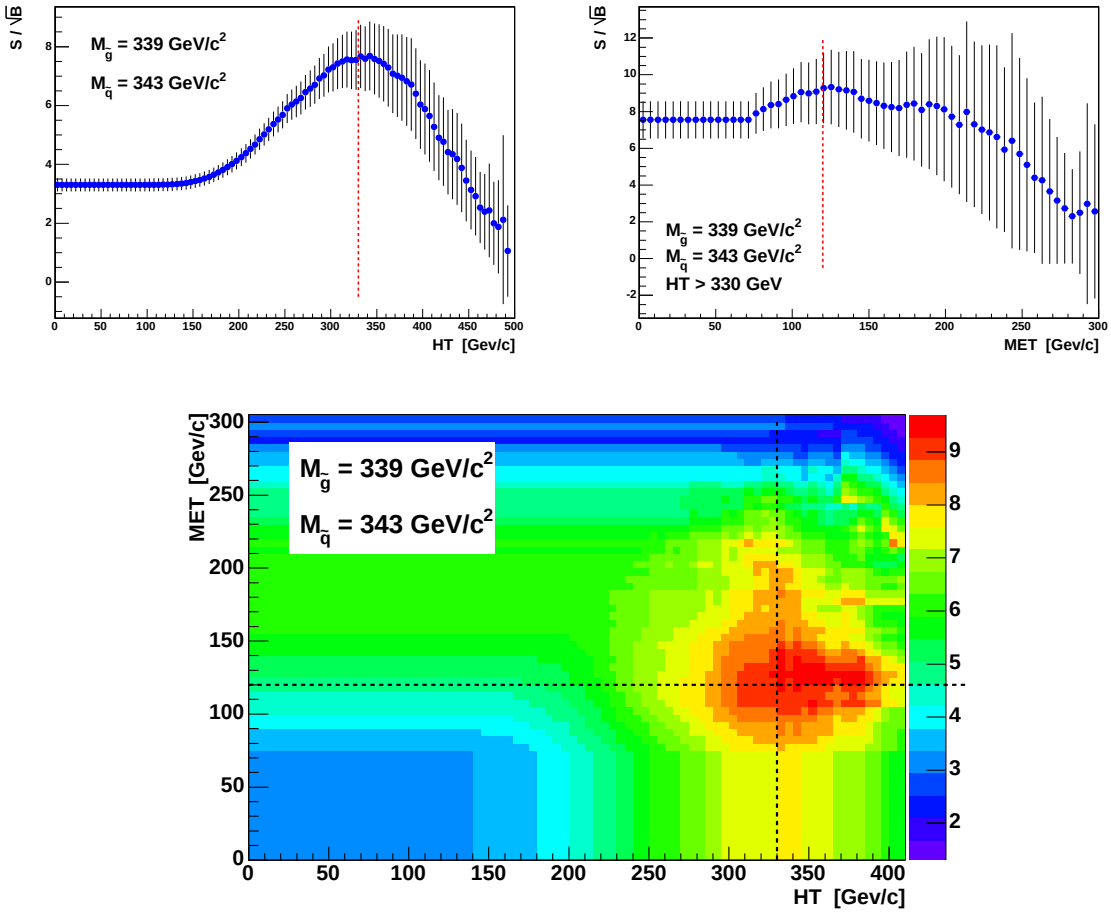

Figure 3.5: Top: $S/\sqrt{B}$ distribution for a representative mSUGRA point ($M_{\tilde{q}} \simeq M_{\tilde{g}} \simeq 340$ GeV/c^2) as a function of the final cuts on H_T(left) and $\not\!\!E_T$ (right). Bottom: $S/\sqrt{B}$ distribution for a representative mSUGRA point ($M_{\tilde{q}} \simeq M_{\tilde{g}} \simeq 340$ GeV/c^2) as a function of the final cuts on both H_T and $\not\!\!E_T$.

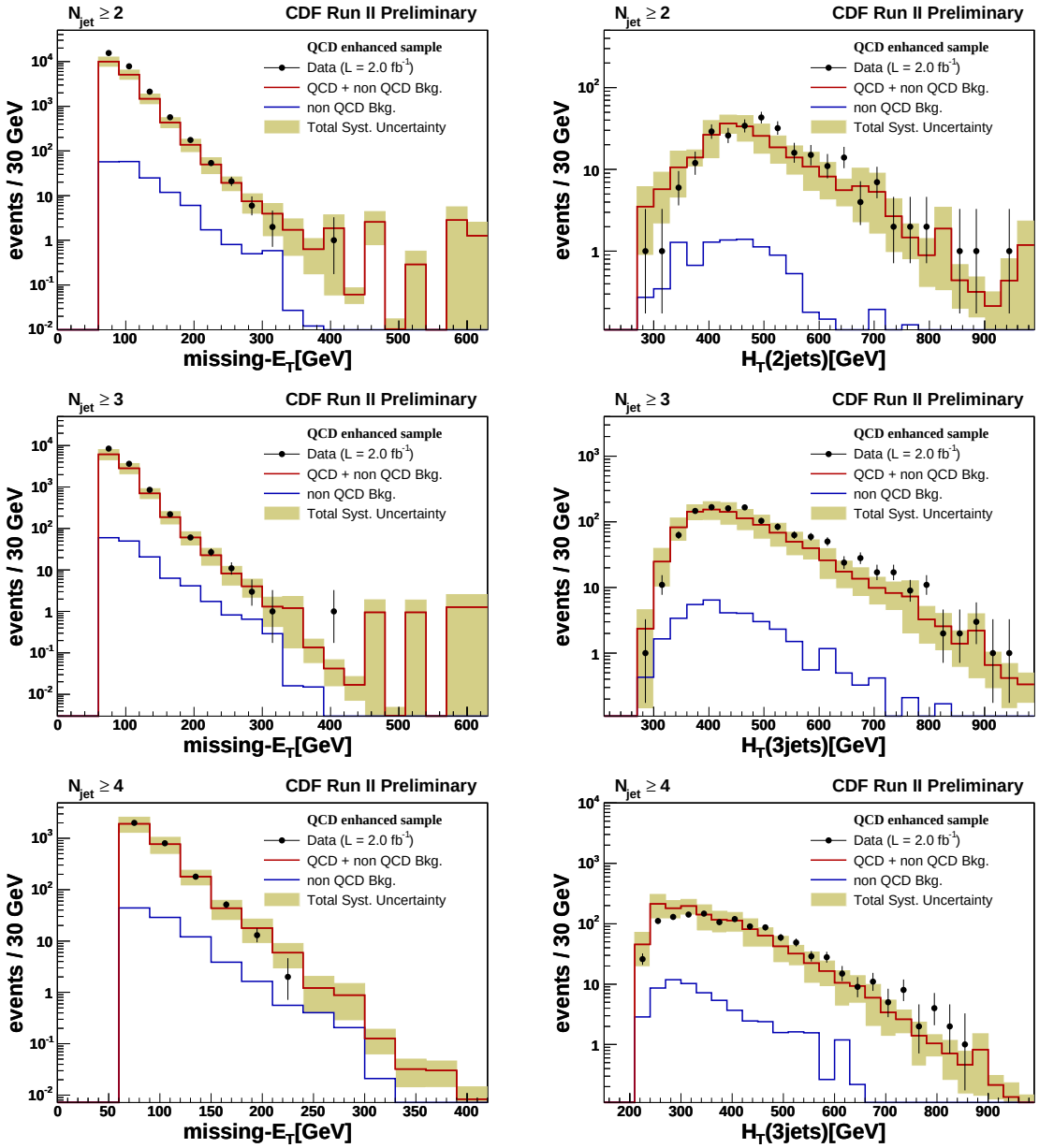

Figure 3.6: $\not\!\!E_T$ and H_T distributions in the QCD dominated control region for the 2-jet analysis (top), the 3-jet analysis (middle), and the 4-jet analysis (bottom). MC samples (red solid lines) provide a reasonable description of the data (black dots) within systematics (beige band). The blue solid line indicates the non-QCD background, including all the other contributions from bosons and top decays. Such contamination is always from one up to three order of magnitude smaller than the QCD background in this control region.

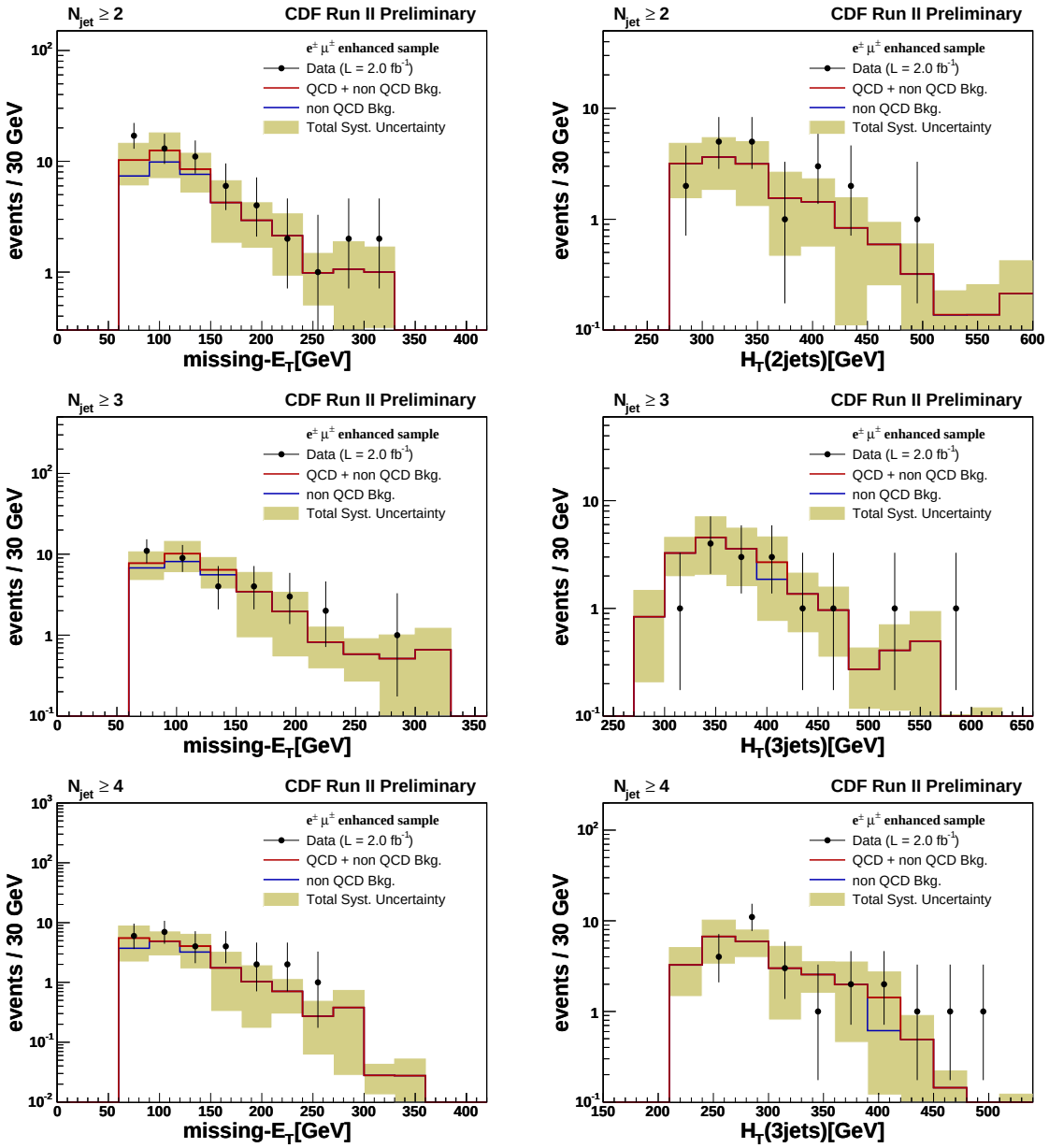

Figure 3.7: $\not\!\!E_T$ and H_T distributions in the muon dominated control region for the 2-jet analysis (top), the 3-jet analysis (middle), and the 4-jet analysis (bottom). MC samples (red solid lines) provide a reasonable description of the data (black dots) within systematics (beige band). The blue solid line indicates the non-QCD background only.

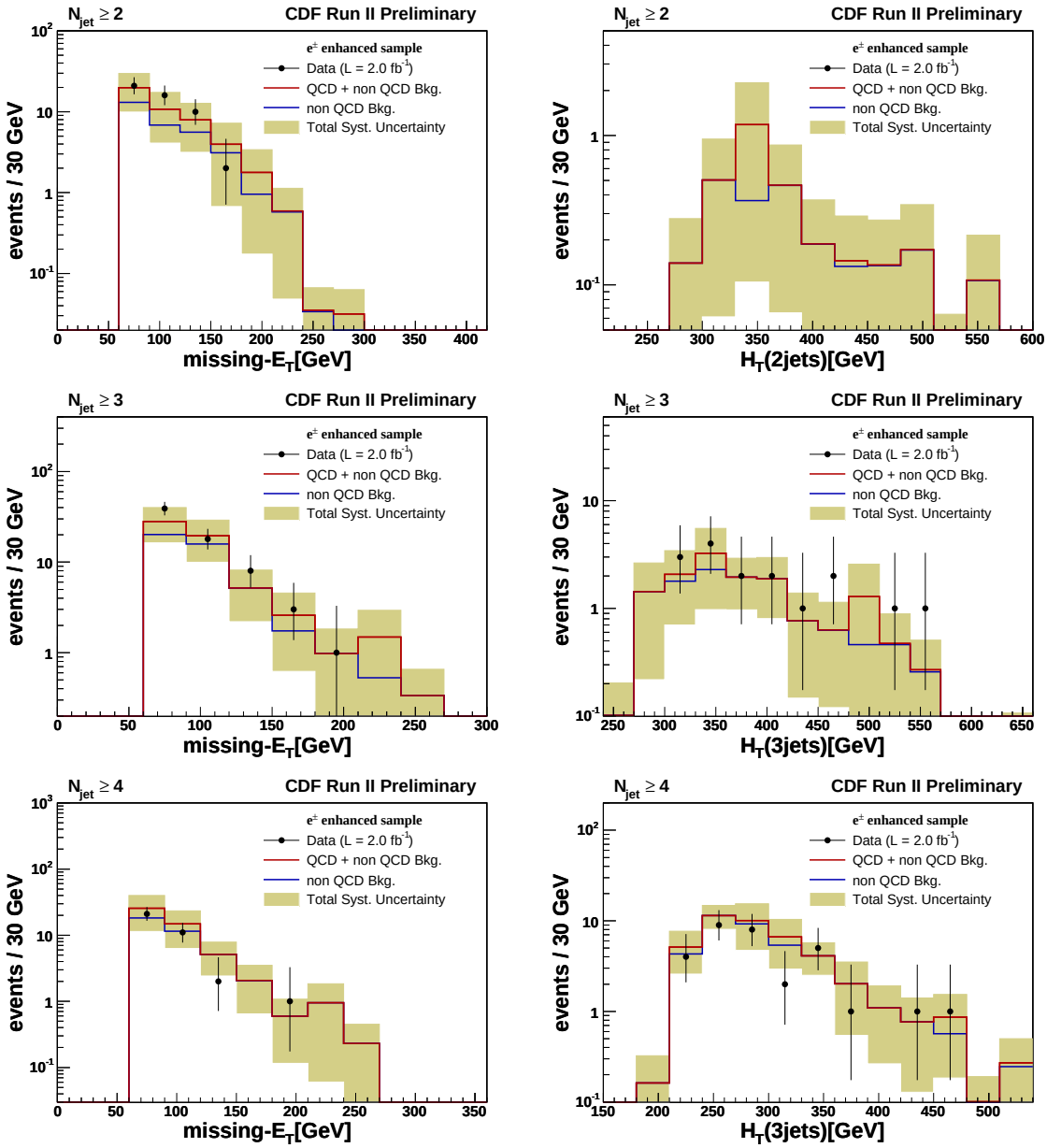

Figure 3.8: $\not\!\!E_T$ and H_T distributions in the electron dominated control region for the 2-jet analysis (top), the 3-jet analysis (middle), and the 4-jet analysis (bottom). MC samples (red solid lines) are in good agreement with data (black dots) within systematics (beige band). The blue solid line indicates the non-QCD background only.

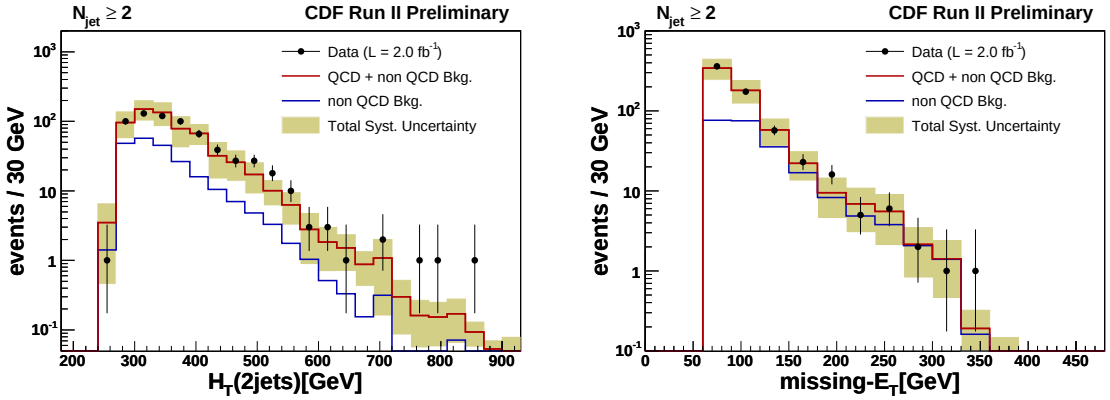

Figure 3.9: N-2 distribution for $\not\!\!E_T$ and H_T in the 2-jet analysis: all selection cuts are applied except for the final thresholds on $\not\!\!E_T$ and H_T cuts. MC samples (red solid lines) are in good agreement with data (black dots) within systematics (beige band). Non-QCD background (blue line) is also shown.

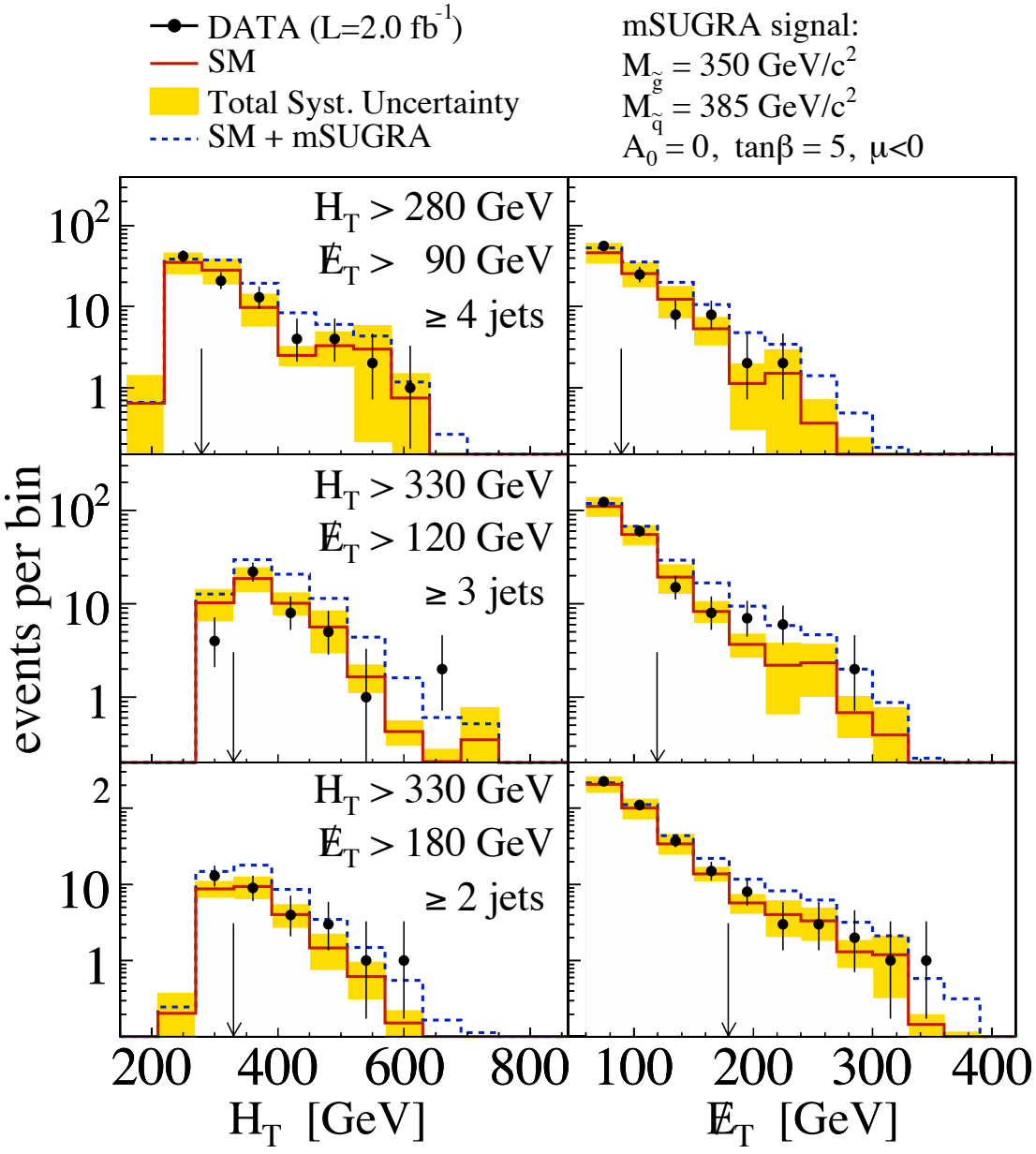

Figure 3.10: measured $\not\!\!E_T$ and H_T distributions (black dots) in events with at least two (bottom), three (middle), and four (top) jets in the final state compared to the SM predictions (solid lines) and the SM + mSUGRA predictions (dashed lines). The shaded bands show the total systematic uncertainty on the SM predictions. In these plots, all final cuts are applied except the one on the variable that is represented. The final threshold on this variable is indicated by the black arrow pointing toward the x-axis.

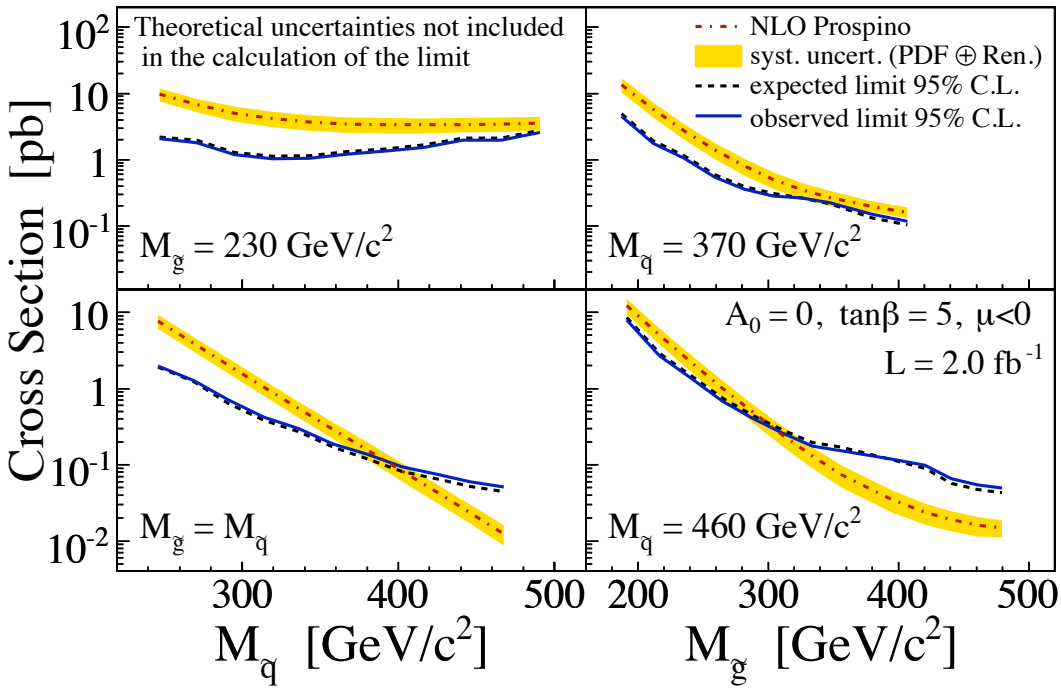

Figure 3.11: observed (solid lines) and expected(dashed lines) 95% CL upper limits on the inclusive squark and gluino production cross sections as a function of $M_{\tilde{q}}$ (left) and $M_{\tilde{g}}$ (right) in different regions of the squark-gluino mass plane, compared to NLO mSUGRA predictions (dashed-dotted lines). The shaded bands denote the total uncertainty on the theory.

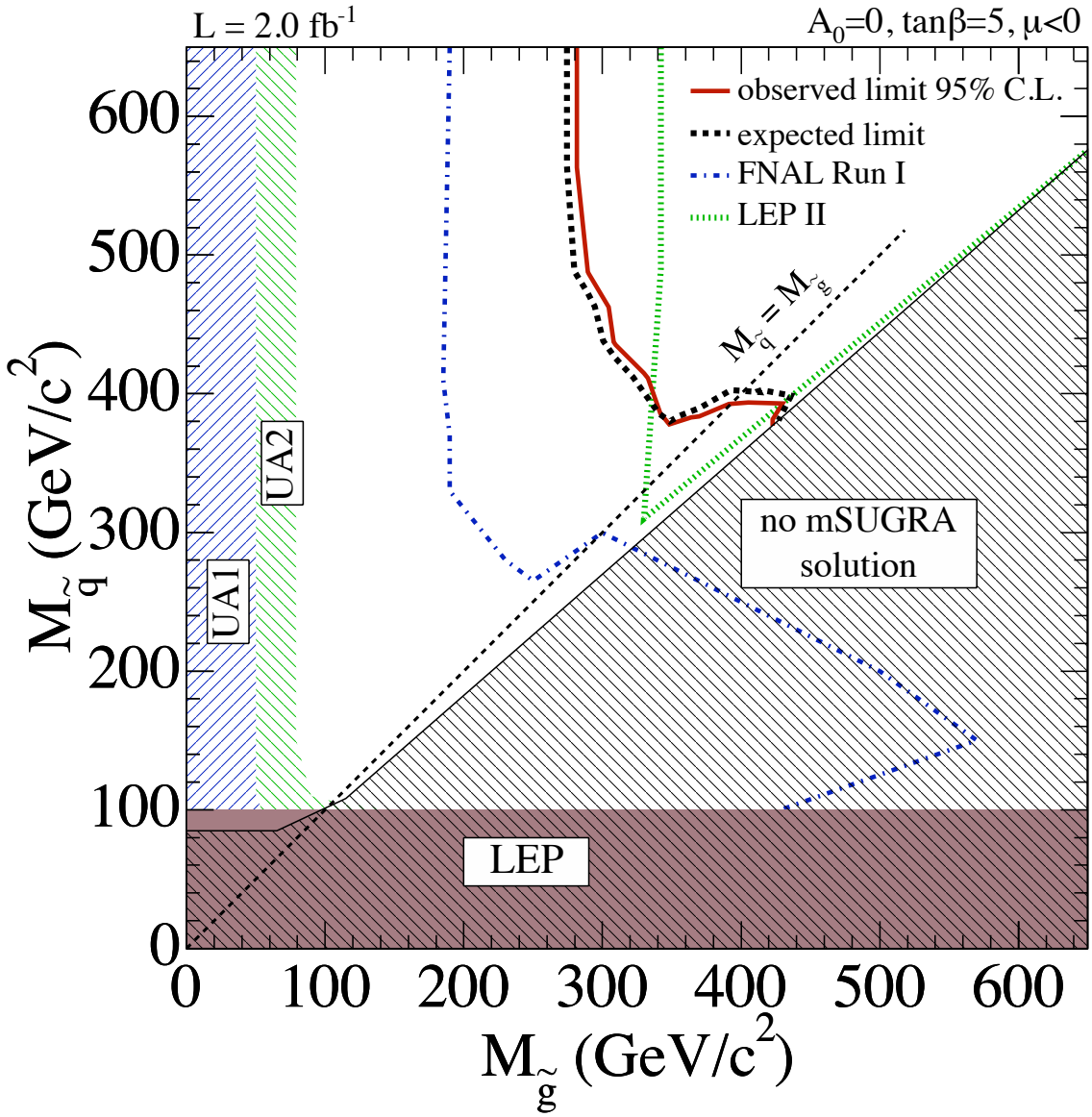

Figure 3.12: exclusion plane at 95%CL as a function of squark and gluino masses in an mSUGRA scenario with $A_0 = 0$, sign(μ) $= -1$ and tan$\beta = 5$. The observed (solid line) and expected (dashed line) upper limits are compared to previous results from SPS [71] and LEP [72] experiments at CERN (shaded bands), and from the Run I at the Tevatron [68] (dashed-dotted line).

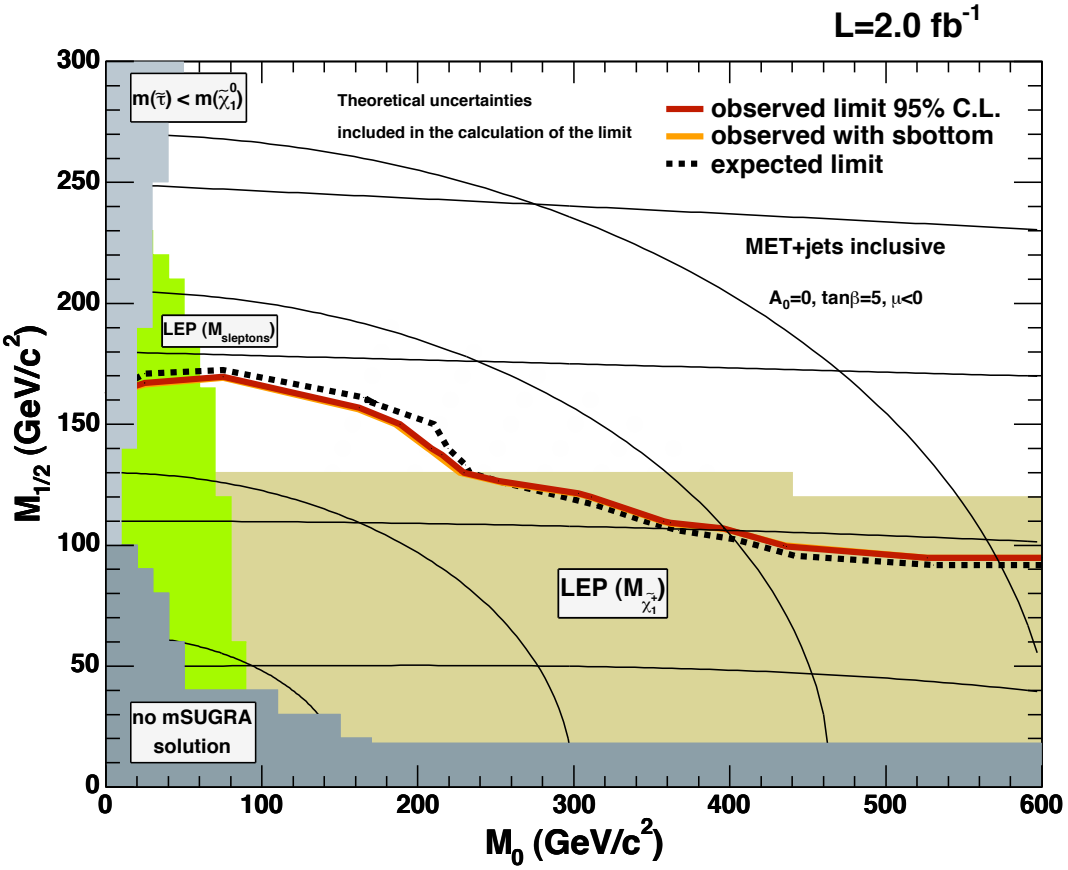

Figure 3.13: observed (solid line) and expected (dashed line) exclusion limits at 95% CL on the M_0 - $M_{1/2}$ plane. The light-grey region indicates the region where $m(\tilde{\tau}) < m(\tilde{\chi}_1^0)$. The beige and green regions are excluded by LEP2 chargino and slepton searches[72], respectively. No mSUGRA solution is found in the dark-grey region. The black lines are the iso-mass curves for gluinos (horizontal) and squarks (elliptic) corresponding to masses of 150, 300, 450 and 600 GeV/c^2.

Chapter 4

Search for Sbottom Pair Production

This analysis is a natural extension of the inclusive search presented in the previous Chapter to a SUSY scenario where the ratio of the vacuum expectation values of the two supersymmetric Higgs fields becomes large with the consequent significant mass difference between mass eigenstates in the sbottom squark sector, leading to a rather light sbottom $\tilde{b}_1$ mass state. A general MSSM model is assumed, with the conservation of R-parity and the production of the sbottoms in pairs. The SUSY mass hierarchy is assumed in order to force the sbottom to decay into a bottom quark and a neutralino (LSP). The expected signal for direct sbottom pair production is characterized by the presence of two jets of hadrons from the hadronization of the bottom quarks and large missing transverse energy $\not\!\!E_T$ from the two LSPs in the final state.

4.1 Dataset and Trigger Selection

This search is based on CDF Run II data collected between February 2002 and April 2008, corresponding to a total integrated luminosity of 2.6 fb^{-1}. Table 4.1 shows the values of the integrated luminosity for different data taking periods.

Data are collected using a three-level trigger system that selects events with at least one calorimeter cluster with E_T above 100 GeV (JET100 trigger). JET100 has been chosen in spite of a trigger based on $\not\!\!E_T$, like the MET35 trigger used for the inclusive search, for two main reasons: to avoid the prescale effect that has become more important since the end of 2007, and to avoid the trigger tower saturation problem described in Section 3.1. Details on the study of the JET100 trigger efficiency are in Section 4.3.

4.2 Event Pre-Selection

The events selected with the JET100 trigger are required to have a primary vertex with a z position within 60 cm of the nominal interaction. Jets are reconstructed from the energy deposits in the calorimeter towers using a cone-based jet algorithm with cone radius R = 0.4, and the measured E_T(jet) is corrected for detector effects and contributions from multiple $p\bar{p}$ interactions per crossing at high instantaneous luminosity, as discussed in Section 2.3.1. The events are initially selected with $\not\!\!E_T > 10$ GeV and two jets with corrected transverse energy $E_T(\text{jet}) > 25$ GeV and pseudo-rapidity in the range $|\eta(\text{jet})| < 2.0$. Events with additional

Data Period	time-range	lumi pb^{-1}
period 0	04 Feb 02 - 22 Aug 04	355
period 1	07 Dec 04 - 18 Mar 05	111
period 2	19 Mar 05 - 20 May 05	121
period 3	21 May 05 - 19 Jul 05	102
period 4	20 Jul 05 - 04 Sep 05	84
period 5	05 Sep 05 - 09 Nov 05	136
period 6	10 Nov 05 - 14 Jan 06	93
period 7	14 Jan 06 - 22 Feb 06	29
period 8	09 Jun 06 - 01 Sep 06	106
period 9	01 Sep 06 - 22 Nov 06	161
period 10	24 Nov 06 - 31 Jan 07	266
period 11	31 Jan 07 - 30 Mar 07	229
period 12	01 Apr 07 - 13 May 07	161
period 13	13 May 07 - 04 Aug 07	189
period 14	28 Oct 07 - 03 Dec 07	41
period 15	05 Dec 07 - 27 Jan 08	151
period 16	27 Jan 08 - 27 Feb 08	119
period 17	28 Feb 08 - 16 Apr 08	185
	tot. integr. luminosity	2639

Table 4.1: the JET100 dataset used in this analysis, divided into 17 data taking periods corresponding to a total integrated luminosity of 2.6 fb^{-1}.

jets with $E_T(\text{jet}) > 15$ GeV and $|\eta(\text{jet})| < 2.8$ are not considered. As for the inclusive analysis, beam-related backgrounds and cosmic rays are removed by requiring an average jet electromagnetic fraction EEMF> 0.15 and an average charged particle fraction ECHF> 0.15 .

Summary of pre-selection cuts

The pre-selection cuts are summarized below:

- $|V_z| < 60$ cm .
- number of jets per event $N_{jets} = 2$.
- $E_T(\text{jet}_{1,2}) \geq 25$ GeV and $|\eta(\text{jet}_{1,2})| < 2.0$.
- EEMF ≥ 0.15 .
- ECHF ≥ 0.15 .
- $\not\!\!E_T > 10$ GeV .

4.3 JET100 Trigger Efficiency

The efficiency of the JET100 trigger is studied as a function of the energy of the leading jet $E_T(\text{jet}_1)$ and the total missing transverse energy of the event $\not\!\!E_T$. An unbiased data sample

is selected with a combination of high-pt muon and missing-energy triggers to ensure enough statistics across the whole $\not\!\!E_T$ spectrum. In particular events with $\not\!\!E_T < 80$ GeV are selected with CMUP18/CMX18 trigger requiring a muon with a minimum pt in the central muon chambers, while events with $\not\!\!E_T > 80$ GeV are selected with the MET45 trigger requiring a minimum threshold of 45 GeV on the $\not\!\!E_T$. In the two cases the efficiency ϵ_{JET100} is defined as:

$$\begin{aligned} \not\!\!E_T < 80 \text{ GeV} : \epsilon_{JET100} &= \frac{N_{(CMUP18/CMX18 \,\&\, JET100)}}{N_{(CMUP18/CMX18)}} \\ \not\!\!E_T > 80 \text{ GeV} : \epsilon_{JET100} &= \frac{N_{(MET45 \,\&\, JET100)}}{N_{(MET45)}} \end{aligned} \tag{4.1}$$

The 80 GeV threshold is well above the MET45 turn-on and yet low enough for the muon triggers CMUP18/CMX18 to guarantee acceptable statistics. The event selection strategy is analogous to the one employed in the searches described in this Thesis and in particular all pre-selection cuts described in Section 4.2 are applied, with no lower threshold on the $\not\!\!E_T$. The scatter plot in Figure 4.1 shows the trigger turn-on in the $\not\!\!E_T - E_T(\text{jet}_1)$ plane. The uniform red region for $E_T(\text{jet}_1) > 130$ GeV represents the plateau where the JET100 trigger is fully efficient regardless of the value of the $\not\!\!E_T$. Below this energy, the shape of the trigger turn-on changes with $\not\!\!E_T$ and needs to be carefully parameterized. The black dashed line parallel to the x-axis in Figure 4.1 indicates the 80 GeV energy threshold defined to merge the CMUP18/CMX18 and MET45 datasets. The trigger efficiency is calculated for different ranges of $E_T(\text{jet}_1)$ and plotted along the $\not\!\!E_T$ in Figure 4.2: no significant discontinuity across the 80 GeV threshold is observed.

To parameterize the trigger efficiency, a typical turn-on shape is assumed with the following functional form:

$$\epsilon_{JET100}(E_T(jet_1), \not\!\!E_T) = \frac{1}{1 + e^{-a(\not\!\!E_T)\cdot(E_T + b(\not\!\!E_T))}} \tag{4.2}$$

where:

$$a(\not\!\!E_T) = \frac{1}{\delta_0 + \delta_1\sqrt{\not\!\!E_T}} \tag{4.3}$$

$$b(\not\!\!E_T) = \frac{\alpha_0 + \alpha_1 \not\!\!E_T + \alpha_2 \not\!\!E_T{}^2}{\beta_0 + \beta_1 \not\!\!E_T + \beta_2 \not\!\!E_T{}^2}. \tag{4.4}$$

Equation 4.2 is valid under the assumption that the trigger efficiency tends asymptotically to 100% with increasing $E_T(\text{jet}_1)$. The dependence on $\not\!\!E_T$ is described in terms of the coefficients a and b:

- a represents the resolution of the trigger turn-on and decreases as the inverse of the square root of the missing transverse energy (Equation 4.3).
- b indicates the turn on threshold $\epsilon(E_T = |b|) = 50\%$ and it is expressed as the ratio of two second-order polynomials (Equation 4.4).

Equation 4.2 is fitted to the trigger turn-on in different ranges of $\not\!\!E_T$ to obtain the coefficients a and b for individual $\not\!\!E_T$ values. Examples of these fits are collected in Figure 4.3. Distributions

of a and b along the $\not\!\!E_T$ spectrum are displayed in Figure 4.4 and fitted with Functions 4.3 and 4.4. To cover the differences between a (b) values and the fitted function a $\pm 5\%$ ($\pm 1\%$) offset is assumed (grey lines on the plots). Final values of α_i, β_i, and δ_i parameters, and correspondent fit errors are summarized in Table 4.2.

α_0	-113 ± 7
α_1	0.52 ± 0.17
α_2	$-5.5 \cdot 10^{-3} \pm 0.8 \cdot 10^{-3}$
β_0	1.01 ± 0.06
β_1	$-5.40 \cdot 10^{-3} \pm 1.4 \cdot 10^{-3}$
β_2	$5.9 \cdot 10^{-5} \pm 0.9 \cdot 10^{-5}$
δ_0	3.00 ± 0.08
δ_1	0.55 ± 0.1

Table 4.2: results of trigger efficiency parameterization fits. Coefficients are defined in Equations 4.3 and 4.4.

4.4 b-tagging selection

The MSSM signal is expected to contain at least two b-jets in the final state from the decay of the sbottom. b-jets are identified using the SecVtx b-tagging algorithm, based on the presence of a displaced vertex from the decay of a b hadron inside the jet. As described in Section 2.3.3, two versions of this algorithm are in use, one optimized for higher efficiency (loose), the other for higher purity (tight). In this analysis, jets are tagged according to the tight-tag requirements, while loose-tags are used for cross check purposes only. An event is b-tagged if at least one of the two leading jets is tight-tag and central ($|\eta| < 1.1$).

4.4.1 b-tagging for MC events

The contribution to the final SM prediction due to events with a light-flavor jet that is misidentified as a b-jet (mistags) is estimated from data. Therefore, regardless of the process simulated, MC events with no heavy-flavour jets[1] are rejected. For the remaining event, the final yield will be the product of the pretag yields and the tagging efficiency:

$$N_{b-tag}^{HF-MC} = \epsilon_{tag} \times N_{pretag}^{HF-MC} \tag{4.5}$$

where

$$N_{pretag}^{HF-MC} = \epsilon_{trigger} \times \epsilon_{selection} \times \sigma_{MC} \times \int \mathcal{L}\, dt \tag{4.6}$$

Since the SecVtx algorithm applied on MC events overestimates the tagging rate, a tagging scale factor k_{tag}^i must be integrated into the tagging efficiency calculation. The value of k_{tag}^i is 0.95 for heavy-flavor jets and null otherwise, and it is the same for both tight-tag and loose-tag configurations. Each event is weighted by a probability of the event being tagged

[1] a jet is heavy-flavour if the closest b or c parton is matched to the jet, i.e. if the angular distance between the jet and the parton is less than the jet cone: $\Delta R(jet - b/c) < 0.4$.

as opposed to using the Monte Carlo to count tags. With the b-tagging requirements defined above, the probability that an event is tagged is:

$$P_{event}^{tag} = 1 - \prod_{i}^{jets}(1 - k_{tag}^{i}). \tag{4.7}$$

Finally the tag efficiency is given by:

$$\epsilon_{tag} = \frac{\sum_{j}^{event} P_{j}^{tag}}{N_{pretag}} \tag{4.8}$$

The 1σ uncertainty on k_{tag}^{i} depends on whether the parent parton is a b or a c:

$$\begin{aligned} k_{tag}^{i} &= 0.95 \pm 0.05 \text{ (for } b\text{-matched jets)}, \\ k_{tag}^{i} &= 0.95 \pm 0.10 \text{ (for } c\text{-matched jets)}. \end{aligned} \tag{4.9}$$

The values of the uncertainties on the MC tag rate are based on the study in [63] and contribute to the total systematic uncertainty of the MC yields (both signal and background) in the search for direct sbottom pair production.

4.5 Further Rejection of SM Backgrounds: Selection Cuts

The list of SM backgrounds for the direct sbottom search includes: QCD di-jet processes, W and Z/γ^* boson production in association with jets, $t\bar{t}$ and single top events, diboson decays. Further rejection of specific SM backgrounds in pre-selected data is obtained with specific selection cuts. The SM QCD multijet background contribution with large $\not\!\!E_T$, due to the mis-reconstruction of the jet energies in the calorimeters, is suppressed by requiring an azimuthal separation $\Delta\phi(\not\!\!E_T - \text{jet}_{1,2}) > 0.4$ for the two jets in the event. The SM background contributions with energetic electrons from W and Z decays and reconstructed as jets in the final state are suppressed by requiring the electromagnetic fraction of the jet transverse energy to be $f_{emf}^{jet1,2} < 0.9$ In addition, events with isolated tracks with transverse momentum $p_T > 10$ GeV/c are vetoed, thus rejecting backgrounds with W or Z bosons decaying into muon or tau leptons.

summary of selection cuts

The selection cuts are summarized as follows:

- $\Delta\phi(\not\!\!E_T - \text{jet}_{1,2}) > 0.4$
- $f_{emf}^{jet1,2} < 0.9$
- No isolated tracks

4.6 The Estimation of the SM Background

Among the SM backgrounds in the analysis, the dominant contamination comes from mistags events, followed by QCD multijet events with jets originating from b-quarks in the final state. Contributions form both QCD and mistag are estimated directly from data while other backgrounds are estimated with MC techniques.

Mistags

For mistags, a data-driven multi-dimensional parameterization is employed to estimate the probability for a light-flavor jet in each event to be mistagged. As described in Section 2.3.4, the mistag rate is obtained from the ensemble of negatively tagged jets as a prediction of the light flavor jet contribution to the positive tag sample. This analysis employs the standard CDF mistag parametrization summarized in Table 2.2. On average, the mistag rate for the tight-tag selection is around 1.5%, and the probability for a light flavor jet of being mistagged increases with the transverse energy of the jet E_T and the number of good SVX tracks N_{trk}; the same probability decreases with increasing number of vertices N_{Vz} per event. Finally, the systematic uncertainty associated to the estimation of the mistag rate depends on the jet kinematics and has an average value around 8%.

QCD multijet heavy-flavour background

The second most important background contamination is due to QCD multijet processes with a heavy-flavor jet in the final state. For these processes the observed $\not\!\!E_T$ comes from partially reconstructed jets in the final state. As for the mistags, also the estimation of the QCD background is obtained with a data-driven technique. This strategy is different from what is done in the inclusive analysis where QCD background is simulated with Pythia. The choice is driven by the fact that the simulation of the necessary amount of heavy-flavor multijet events would require an impracticable amount of time and computing resources.

To estimate from data the number of QCD events surviving the b-tagging selection, a QCD dominated region is defined by inverting the $\Delta\phi(\not\!\!E_T - \text{jet}_{1,2})$ cut and relaxing the veto on the third jet in the pre-selection criteria:

- At least 1 Q12 vertex with $|V_Z| < 60\ cm$
- ECHF, EEMF > 0.15
- No isolated tracks
- At least two jets per event with $E_T > 15\ GeV$ and $|\eta| < 2.8$
- First and second leading jets are required to have $E_T > 25\ GeV$ and $|\eta| < 2.0$
- At least one of the two leading jets is required to be central ($|\eta| < 1.1$)
- One of the two leading jets is required to be collinear with the $\vec{\not\!\!E}_T$: $\Delta\phi(\not\!\!E_T - \text{jet}_{1,2}) < 0.4$
- $f_{emf}^{jet1,2} < 0.9$
- $\not\!\!E_T > 10\ GeV$

The $\not\!\!E_T$ spectrum is presented in Figure 4.5 where data are compared to non-QCD and MSSM expectation. The contributions from non-QCD backgrounds and potential MSSM signal are negligible. Because of the $\Delta\phi(\not\!\!E_T - \text{jet}_{1,2}) < 0.4$ requirement, at least one jet per event is collinear with the $\not\!\!E_T$ and none of the events falls into the signal region. These events are

used to estimate the probability p^{HF}_{QCDjet} for a heavy-flavor QCD jet to pass the b-tagging requirements:

$$p^{HF}_{QCDjet} = p^{tag}_{QCDjet} - p^{mistag}_{QCDjet} = \frac{N^{tag}_{jets} - N^{mistag}_{jets}}{N^{taggable}_{jets}} \tag{4.10}$$

where:

- N^{tag}_{jets} is the number of SecVtx tagged jets,
- N^{mistag}_{jets} is the number of mistags,
- $N^{taggable}_{jets}$ is the number of taggable[2] jets.

The probability is parametrized as a function of three variables, the jet (E_T), the number of good SecVtx tracks associated to the jet (N_{trk}), and the missing transverse energy of the event ($\not\!\!E_T$). The set of the different values of p^{HF}_{QCDjet} defines a tagging probability matrix (TPM) whose binning is defined in Table 4.3. The TPM granularity is chosen in order to be as fine as possible with acceptable occupancy in all the bins (statistical errors below 20%). This means that the QCD estimation is affected by an intrinsic uncertainty due to the finite statistic of the QCD-enhanced sample used to build the tagging probability matrix. However, even if for some bins of the TPM the statistical uncertainty is as high as 20%, the overall effect over the expected QCD yields in the signal regions is very small ($\sim 1\%$) as reported in Section 4.9. A number of tables showing TPM occupancy and relative uncertainty for all the bins are presented in Appendix A together with several figures displaying the values of p^{HF}_{QCDjet} as a function of the kinematic variables of interest.

E_T^{corr}	N_{trk}	$\not\!\!E_T$
25	2	10
50	4	20
70	5	30
90	6	40
110	7	50
120	8	60
130	10	70
140	13	
150		

Table 4.3: Final binning of the TPM matrix.

The presence of the collinear jets in the QCD dominated region can introduce a potential bias since such jets are not present in the signal regions. Therefore, the calculation of p^{HF}_{QCDjet} in Equation 4.10 is performed using, for each event, only those jets with $\Delta\phi(\not\!\!E_T - \text{jet}) > 0.4$. Another (smaller) bias is due to the presence in the QCD dominated region, but not in the signal regions, of jets going in the opposite direction of the $\not\!\!E_T$, i.e. with $\Delta\phi(\not\!\!E_T - \text{jet}) \in [\pi - 0.4, \pi]$. The choice of using these jets in the calculation of p^{HF}_{QCDjet} despite the potential

[2] A jet is *taggable* when it is central ($|\eta| < 1.1$) and contains at least two good SecVtx tracks ($N^{SVXtrk}_{jet} \geq 2$).

bias is driven by the need of having as much statistic as possible. To estimate the bias, two different estimations of the QCD background are carried out: a nominal configuration including all jets with $\Delta\phi(\not\!\!E_T - \text{jet}) \in [0.4, \pi]$ and a second one excluding those jets with $\Delta\phi(\not\!\!E_T - \text{jet}) \in [\pi - 0.4, \pi]$. Figure 4.6 shows the ratio between the two different QCD estimations along the $\not\!\!E_T$ spectrum. Similar distributions with different kinematic variables are also considered and a $\pm 10\%$ offset is seen to cover any discrepancy between the two QCD estimations.

Once defined, the coefficients in the TPM are used to weight the data events in the pretag sample, where all the selection cuts, but the tag requirement, are applied. The weighting procedure works as follows:

- a value of the probability p^{HF}_{QCDjet} is associated to each of the two jets in a pretag data event according to the values of $E_T(\text{jet})$, N_{trk}, and $\not\!\!E_T$;
- the number of QCD heavy-flavour tagged events is given by the sum $N^{HF-QCD}_{b-tag} = \sum_{events}(1 - \prod_i^{jets}(1 - p^{HF}_{QCDjet}))$, where the sum runs over all the events in the pretag sample;

The number N^{HF-QCD}_{b-tag} is finally normalized according to the assumption that the number of events in the pretag sample is given by the sum of QCD and non-QCD events (negligible signal contribution): $N_{pretag} = N^{QCD}_{pretag} + N^{non-QCD}_{pretag}$

non-QCD heavy-flavour backgrounds

Simulated event samples are used to determine detector acceptance and reconstruction efficiency and estimate the contribution from the rest of the SM backgrounds with heavy-flavor jets in the final state. Samples of simulated Z/γ^* and W + jets events with light- and heavy-flavor jets are generated using the Alpgen program interfaced with the parton-shower model from Pythia. To enhance the heavy flavor content, two different kind of samples are produced: inclusive samples with no specific flavor requirements, and exclusive samples with Z/γ^* and W decaying into heavy-flavor partons. The combination of exclusive and inclusive samples is based on the assumption that Alpgen can correctly reproduce the relative contribution of the different samples and obeys specific matching criteria to avoid any possible double counting of heavy flavor events. These criteria are detailed in [74] and involve the separation of the heavy-flavor production coming from either parton shower or matrix element. In the inclusive samples, events where matrix-element heavy-flavor quarks are matched to the same jet are vetoed. Events with heavy-flavor from the parton shower in which only one of the two heavy quarks is inside the jet cone are removed as well. In both cases the matching criteria is the same as for the b-tagging, with b/c partons to be within the jet cone ($\Delta R(jet - b/c) < 0.4$). The normalization of the boson plus jets heavy-flavor samples includes an additional factor $K_{HF} = 1.4 \pm 0.4$ that brings the predicted light- to heavy-flavor relative contributions to that observed in the data [75]. Since the relative contributions of the different exclusive and inclusive sub-samples are correctly reproduced by Alpgen, the final combined sample, after the MLM matching, the HF overlap removal, and the K_{HF} normalization, can be simply normalized to the measured Z and W inclusive cross sections [37] following the same normalization strategy used in the inclusive analysis.

The simulation of the remaining SM backgrounds follows the exact same scheme used in the inclusive analysis and described in Section 3.4 . Samples of simulated $t\bar{t}$ and diboson

($WW/ZW/ZZ$) processes are generated using Pythia Monte Carlo generator with Tune A and normalized to next-to-leading order (NLO) predictions [38][40]. Finally, samples of single top events are produced using the MadEvent program and normalized using NLO predictions [76].

4.7 The MSSM Signal

The SUSY samples are generated in the framework of MSSM as implemented in Pythia with fixed $\tilde{b}_1$ and $\tilde{\chi}_1^0$ masses and the exclusive decay $\tilde{b}_1 \to b\tilde{\chi}_1^0$. A total of 106 different samples are generated with sbottom mass $M_{\tilde{b}_1}$ in the range between 80 GeV/c^2 and 280 GeV/c^2 and neutralino mass $M_{\tilde{\chi}_1^0}$ up to 100 GeV/c^2. Figure 4.7 shows the signal samples produced in the sbottom-neutralino mass plane. The samples are normalized to NLO predictions, as implemented in PROSPINO2, using CTEQ6.6 parton distribution functions (PDFs) and renormalization and factorization scales set to $M_{\tilde{b}_1}$. The production cross section depends on $M_{\tilde{b}_1}$ and varies between 50 pb and 0.01 pb as the sbottom mass increases as shown in Figure 4.8 . Further details on MC production and normalization for SUSY events are in Section 1.5.3 .

4.8 Optimization and Definition of Signal Regions

An optimization is performed with the aim of maximizing the sensitivity to a SUSY signal across the sbottom-neutralino mass plane. For each of the 106 signal samples considered, the procedure maximizes $S/\sqrt{B}$, where S denotes the number of SUSY events and B is the total SM background. Several kinematic variables are involved in the optimization: $\not\!\!E_T$, $E_T(\text{jet}_{1,2})$, and the sum between the $\not\!\!E_T$ and $H_T = E_T(\text{jet}_1) + E_T(\text{jet}_2)$. Variables are optimized one by one, and the sequence is varied to check that $S/\sqrt{B}$ is not dependent on the order in which the optimization is performed. The optimal thresholds slightly change from point to point since the kinematic of the events in the MSSM signal is strictly dependent on the mass hierarchy of the simulated sample. In general, as the difference $\Delta M = M_{\tilde{b}_1} - M_{\tilde{\chi}_1^0}$ increases, the optimal energy thresholds increase. As for the inclusive analysis, different sets of cuts are defined for best sensitivity across the whole $M_{\tilde{b}_1} - M_{\tilde{\chi}_1^0}$ plane. In this case, the results from the different MSSM samples are combined to define two single sets of thresholds (see Table 4.4) that maximize the search sensitivity in the widest range of sbottom and neutralino masses at low ΔM ($\Delta M \lesssim 90$ GeV/c^2) and high ΔM ($\Delta M \gtrsim 90$ GeV/c^2), respectively. As an example, for $M_{\tilde{\chi}_1^0} = 70$ GeV/c^2 and $M_{\tilde{b}_1}$ in the range from 150 GeV/c^2 to 250 GeV/c^2, values for $S/\sqrt{B}$ between 10 and 2.5 are obtained, corresponding to SUSY selection efficiencies of 3% to 10%. Graphic examples of $S/\sqrt{B}$ scans for two MSSM points representative of the low and high ΔM regions are in Figure 4.9 and 4.10, respectively. Distributions of $S/\sqrt{B}$ are displayed as a function of $\not\!\!E_T$, $E_T(\text{jet}_1)$, $E_T(\text{jet}_2)$, and H_T for two representative MSSM sample with $M_{\tilde{b}_1} = 123$ and $M_{\tilde{\chi}_1^0} = 90\ GeV/c^2$ and with $M_{\tilde{b}_1} = 193$ and $M_{\tilde{\chi}_1^0} = 70\ GeV/c^2$.

After identifying the optimal energy thresholds, additional variables are investigated. In particular, an increased threshold on $\Delta\phi(\not\!\!E_T - \text{jet}_2)$ from 0.4 to 0.7 is found to further improve the signal significance in both the signal regions. Figure 4.11 shows the distributions of $S/\sqrt{B}$ as a function of $\Delta\phi(\not\!\!E_T - \text{jet}_2)$ for low and high ΔM.

Variable	low ΔM	high ΔM
$\not{E}_T$	60	80
$E_T(\text{jet}_1)$	80	90
$E_T(\text{jet}_2)$	25	40
H_T	–	300
$\Delta\phi(\not{E}_T - \text{jet}_1)$	0.4	0.4
$\Delta\phi(\not{E}_T - \text{jet}_2)$	0.7	0.7

Table 4.4: Summary of the final thresholds for the two signal regions optimized as described in Section 4.8.

4.9 Systematic Uncertainties

A detailed study of systematic uncertainties was carried out for both SM background and MSSM signal.

Systematics for expected SM backgrounds

Different sources of systematic uncertainty are taken into account in the determination of the SM predictions for low and high ΔM configurations.

- The uncertainty on the SM background predictions is dominated by the determination of the b-jet mistag rates (Section 2.3.4), which propagates into an uncertainty in the SM prediction between 13% and 11% as ΔM increases.

- The uncertainty on the K_{HF} value applied to the boson + jets heavy-flavor samples translates into a 11% uncertainty in the SM predictions.

- The dependence on the amount of initial-state and final-state radiation in the Monte Carlo generated samples for top, boson + jets and diboson contributions introduces a 6% uncertainty on the SM predictions.

- Other sources of uncertainty on the predicted SM background are: a 3% uncertainty due to the determination of the b-tagging efficiency in the Monte Carlo simulated samples; a 3% uncertainty from the uncertainties on the absolute normalization of the top quark, diboson, W , and Z Monte Carlo generated processes; and a 2.5% uncertainty as result of a 3% uncertainty on the JES.

- Uncertainties related to trigger efficiency and the heavy-flavor QCD multijet background contribute less than 1% to the final uncertainty.

Table 4.5 presents the summary of uncertainties on the SM predictions. The different sources of systematic uncertainty are added in quadrature. The total systematic uncertainty on the SM predictions varies between 19% and 18% as ΔM increases.

syst	low ΔM	high ΔM
mistags	13.4%	11.4%
K_{HF}	10.8%	11.0%
TPM matrix	1.4%	1%
tag K-factor	3.4%	3.5%
ISR/FSR	5.6%	5.8%
PDF $\oplus$ REN	2.6%	2.7%
JES	2.4%	1.0%
trig eff	1.5%	0.9%
total (no lumi)	18.8%	17.5%
lumi	6.0%	6.0%

Table 4.5: summary of the systematic uncertainties on SM background expected yields.

Systematics for expected MSSM signal

In the case of the MSSM signal, various sources of uncertainty in the predicted cross sections at NLO, as determined using PROSPINO2, are considered:

- The uncertainty due to PDFs is computed using the Hessian method [27] and translates into a 12% uncertainty on the absolute predictions.
- Variations of the renormalization and factorization scale by a factor of two change the theoretical cross sections by about 26%.
- Uncertainties on the amount of initial- and final-state gluon radiation in the MSSM Monte Carlo generated samples introduce a 10% uncertainty on the signal yields.
- The 3% uncertainty on the absolute jet energy scale translates into a 9% to 14% uncertainty on the MSSM predictions.
- Other sources of uncertainty include: a 4% uncertainty due to the determination of the tagging scale factor for MC events, and a 2% to 1% uncertainty due to the uncertainty on the trigger efficiency.

The total systematic uncertainty on the MSSM signal yields varies between 30% and 32% as ΔM increases. Table 4.6 presents the resulting uncertainties for three representative points in the plane.

4.10 Control Regions

As for the inclusive analysis, different control regions are defined to cross check the background prediction separately for each of the signal regions. The samples are defined by reversing the logic of some of the pre-selection and selection criteria in order to enhance the contamination of particular SM processes.

syst	low ΔM	high ΔM
JES	8.7%	14%
ISR/FSR	10%	10%
PDF	12%	11%
REN	26%	25%
tag K-factor	3.7%	4.3%
trig eff	2.4%	1.3%
tot (no lumi)	30%	32%
lumi	6.0%	6.0%

Table 4.6: summary of the systematic uncertainties on MSSM signal efficiency for two signal points Representative of both the signal regions. Masses are set to $M_{\tilde{\chi}_1^0} = 70$ and $M_{\tilde{b}_1} = 153$ for low ΔM and to $M_{\tilde{\chi}_1^0} = 80$ and $M_{\tilde{b}_1} = 183$ for high ΔM.

- **Low $\not\!\!E_T$ region:** the final cut on $\not\!\!E_T$ is inverted to enhance the contribution of heavy-flavor QCD multijet and mistags.
- **Loose-not-tight tag region:** only jets that pass the loose tag requirements but not the tight tag requirements are selected to enhance the contribution from mistags.
- **Low $E_T(\mathbf{jet}_2)$:** the selection criteria on the second jet transverse energy is inverted to enhance the contribution of electroweak processes. For consistency, and to allow for a minimum statistics, no selection on H_T is made. As a consequence, the additional control regions is defined for high ΔM only:
  - $E_T(\text{jet}_1) > 90$ GeV
  - $25 < E_T(\text{jet}_2) < 40$ GeV
  - $\not\!\!E_T > 80$ GeV.

  No Low $E_T(\text{jet}_2)$ control region is possible for low ΔM selection because the threshold $E_T(\text{jet}_2) < 25$ GeV is already at its minimum. Note that in the inclusive analysis, two lepton-dominated control regions are defined inverting the vetoes on muons and electrons, respectively. The same strategy has been tried for the exclusive search as well, but the statistics in the resulting samples is compatible with zero.

Figures 4.12 through 4.16 show the comparison between data and SM predictions for relevant kinematic distributions. A general good agreement is found in all the control samples. Table 4.7 shows the total number of events in the control regions for different ΔM, compared to SM predictions including total uncertainties. The detailed composition of the SM backgrounds in all the control regions are collected in Table 4.8, Table 4.9, and Table 4.10.

4.11 Results

In this Section, the final numbers of observed events in data and expected SM background are presented for a total integrated luminosity of 2.6 fb^{-1}. Table 4.11 compares the expected SM

low ΔM		
control region	data	SM prediction
low $\not\!\!E_T$	60376	58358 ± 5599
loose-not-tight	81	89 ± 21
second jet E_T	-	-
high ΔM		
	data	SM prediction
low $\not\!\!E_T$	60287	58251 ± 5583
loose-not-tight	25	32 ± 8
second jet E_T	42	35 ± 10

Table 4.7: comparison between data and SM predictions in the different control regions for high and low ΔM selections.

SM contribution (events)	Low ΔM	High ΔM
Mistags	34751	34691
QCD	23588	23535
Top	8.7	13.3
$Z \rightarrow \nu\nu$	2.7	5.0
Z/γ^*+jets	0.2	0.3
W+jets	6.9	9.6
Diboson	0.8	0.9

Table 4.8: individual SM background contributions for high and low ΔM selections including total uncertainty in the case of low-$\not\!\!E_T$ control region.

SM contribution (events)	Low ΔM	High ΔM
Mistags	67.9	23.7
QCD	1.5	0.3
Top	4.1	1.6
Z$\rightarrow \nu\nu$	7.7	3.5
Z/γ+jets	0.14	0.06
W+jets	6.5	2.1
Diboson	1.2	0.44

Table 4.9: individual SM background contributions for high and low ΔM selections including total uncertainty in the case of loose-no-tight tag control region.

SM contribution (events)	High ΔM
Mistags	14.4
QCD	0.21
Top	3.5
Z$\rightarrow \nu\nu$	8.9
Z/γ+jets	0.15
W+jets	7.05
Diboson	1.1

Table 4.10: individual SM background contributions for the high ΔM selection including total uncertainty in the case of $E_T(\text{jet}_2)$-reversed control region. Note that no control region for low ΔM is defined.

yields with the observed number of events in data and Table 4.12 gives details on the separate SM contributions. Figure 4.17 shows the H_T and $\not\!\!E_T$ distributions in the low and high ΔM signal regions. In these plots, all final cuts are applied. Both data and SM prediction are presented. For illustration purposes, a representative MSSM point per signal region is also shown. The background Monte Carlo prediction always provides a reasonable description of the data within systematics.

region	data	SM prediction
low ΔM	139	133.8 ± 25.2
high ΔM	38	47.6 ± 8.3

Table 4.11: Number of events in data for each analysis compared to SM predictions, including statistical and systematic uncertainties summed in quadrature.

SM contribution	Low ΔM	High ΔM
Mistags	51.4 ± 17.9	18.5 ± 5.4
QCD	7.6 ± 1.8	1.6 ± 0.2
Top	21.2 ± 3.2	7.8 ± 1.2
Z$\rightarrow \nu\nu$	27.7 ± 8.6	10.9 ± 3.4
Z/γ+jets	0.5 ± 0.2	0.11 ± 0.04
W+jets	22.3 ± 7.2	7.3 ± 2.4
Diboson	3.1 ± 0.5	1.4 ± 0.2

Table 4.12: Individual SM background contributions for high and low ΔM signal regions including statistical and systematic uncertainties summed in quadrature.

4.12 Exclusion Limit

Since no excess with respect to the Standard Model predictions is observed in the data, results are translated into a 95% CL exclusion limits on the direct sbottom pair production cross section. In this analysis, the same Bayesian approach [67] employed in the inclusive search for squarks/gluinos is used (see Appendix B for further details).

For each of the 106 MSSM points in the sbottom-neutralino mass plane, two expected limits are extracted, according to the high and low ΔM selections. For a given MSSM point, the selection that gives the best expected limit is then used to calculate the observed limit. All the systematic uncertainties on signal and background described in Section 4.9 are used in the limit calculation with the exception of the theoretical uncertainties on the MSSM NLO cross section. The correlations between signal and background uncertainties are also considered. Figure 4.18 shows the expected and observed 95% CL limit on the production cross section as a function of the sbottom mass, for a constant neutralino mass of 70 GeV/c^2, compared to NLO predictions. Cross sections down to ~ 0.1 pb are excluded at 95% CL for the range of masses considered. As for the inclusive search, the exclusion limits on the production cross sections are translated into exclusion limits on sbottom and neutralino masses. In this case, the theoretical uncertainties on the NLO cross section for the MSSM signal (PDF and renormalization scale) are directly included into the calculation. Figure 4.19 shows the expected and observed exclusion regions in the sbottom-neutralino mass plane. Sbottom masses up to 230 GeV/c^2 are excluded at 95% CL for neutralino masses in the range 40-80 GeV/c^2. This analysis improves previous CDF results [25] and DØ results [78] obtained with ~ 300 pb by ~ 40 GeV/c^2 and ~ 10 GeV/c^2, respectively. Our results are also compatible with the latest exclusion limits obtained with 4.1 fb^{-1} of data by the DØ Collaboration [79] that exclude sbottom masses below 250 GeV/c^2 for any neutralino with $M_{\tilde{\chi}_1^0} < 70$ GeV.

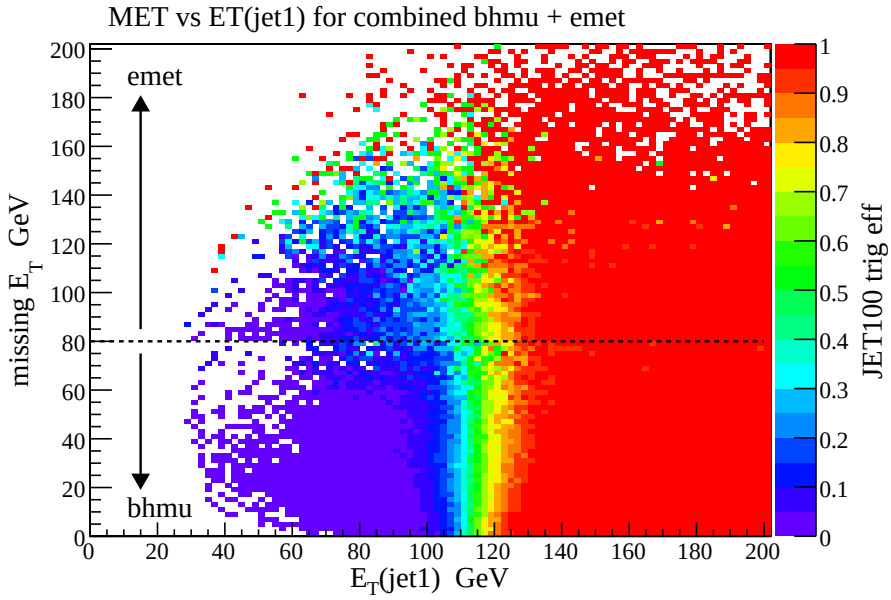

Figure 4.1: JET100 turn on as a function of $E_T(jet_1)$ and $\not\!\!E_T$. Combination of CMUP18/CMX18 and MET45 triggers provides enough statistics up to $\not\!\!E_T \sim 200$ GeV. Events are selected as specified in Section 4.2 with no minimum threshold on $\not\!\!E_T$.

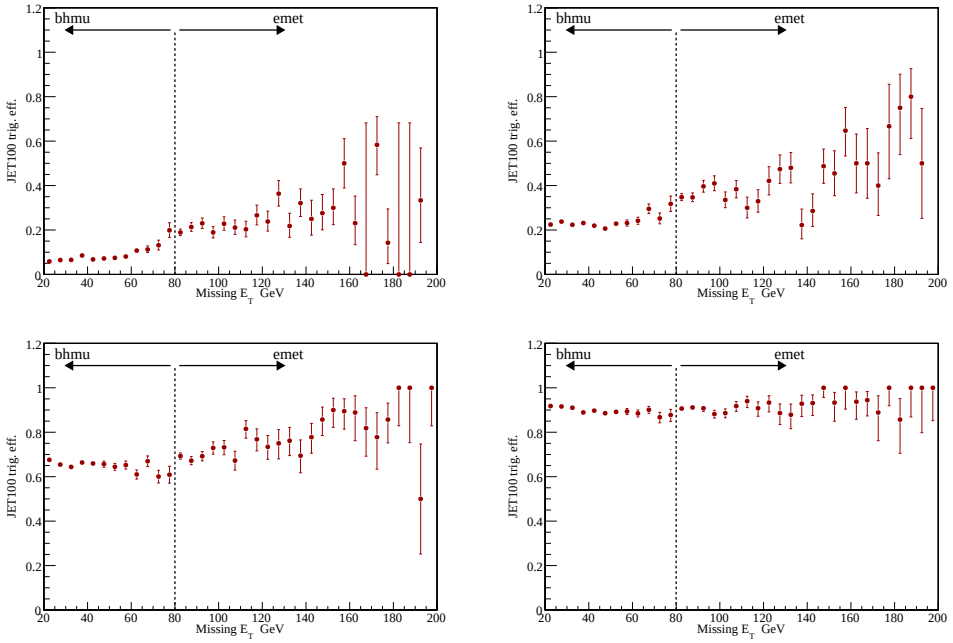

Figure 4.2: JET100 trigger efficiency as a function of $\not\!\!E_T$ in different ranges of $E_T(\text{jet}_1)$: $100 < E_T(\text{jet}_1) < 105$ (top-left), $110 < E_T(\text{jet}_1) < 115$ (top-right), $120 < E_T(\text{jet}_1) < 125$ (bottom-left), $130 < E_T(\text{jet}_1) < 135$ (bottom-right). No discontinuity is observed at 80 GeV passing from CMUP18/CMX18 to MET45 selection. Events are selected as specified in Section 4.2 with no minimum threshold on $\not\!\!E_T$.

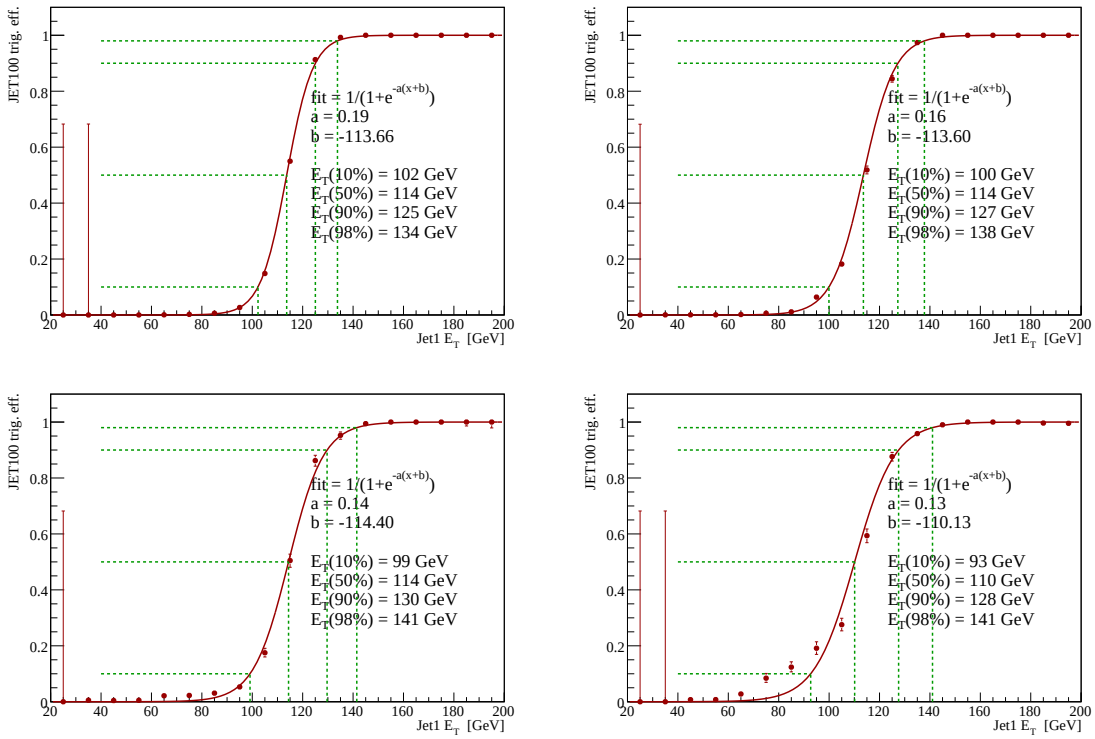

Figure 4.3: JET100 trigger efficiency as a function of $E_T(\text{jet}_1)$ in different ranges of $\not{E}_T$: $10 < \not{E}_T < 11$ (top-left), $29 < \not{E}_T < 31$ (top-right), $49 < \not{E}_T < 51$ (bottom-left), $88 < \not{E}_T < 91$ (bottom-right). Equation 4.2 is fitted to the distributions to obtain the coefficients a and b for individual $\not{E}_T$ values (black line). Events are selected as specified in Section 4.2 with no minimum threshold on $\not{E}_T$.

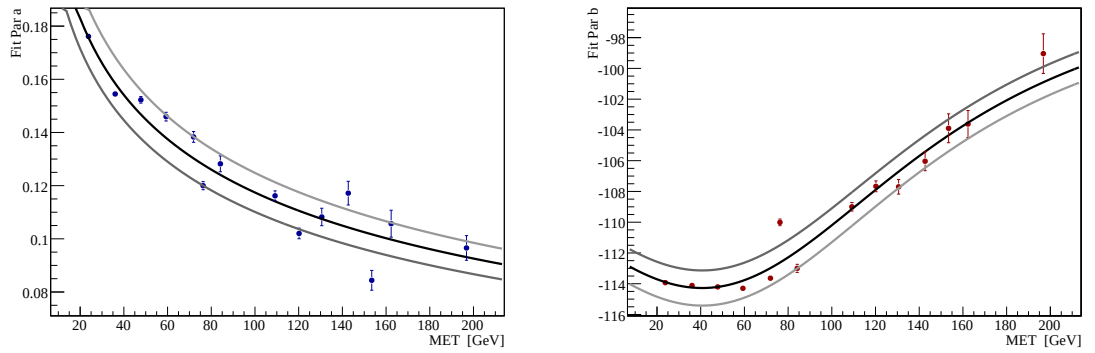

Figure 4.4: distribution of a (left) and b (right) coefficients as a function of $\not{E}_T$. Equations 4.3 and 4.4 are fitted to the distributions (black lines). The grey lines below and above the the nominal fits include almost all the points and represent the assigned uncertainties ($\pm 5\%$ for a and $\pm 1\%$ for b). Events are selected as specified in Section 4.2 with no minimum threshold on $\not{E}_T$.

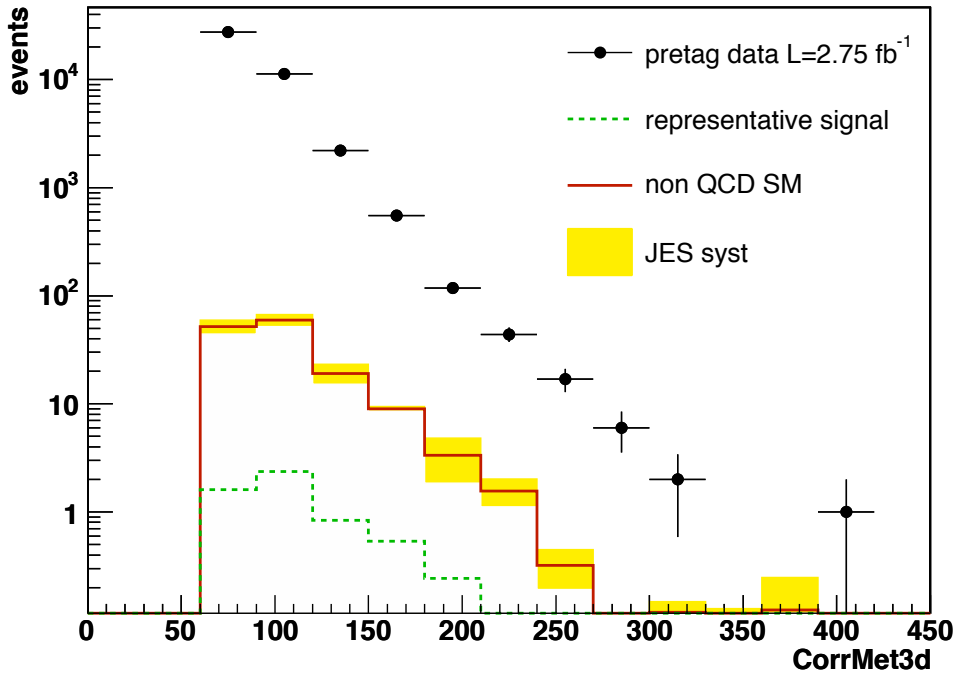

Figure 4.5: distribution of $\not\!\!E_T$ in a QCD dominated region where at least one of the two leading jets is required to have $\Delta\phi(\not\!\!E_T - \text{jet}) < 0.4$. Events are selected according to the cuts described in Section A. For $\not\!\!E_T > 70\ GeV$ there are 41890 data events, ~ 145 non-QCD events, and ~ 6 signal events from a representative MSSM sample. Contributions from non-QCD and MSSM are therefore considered as negligible.

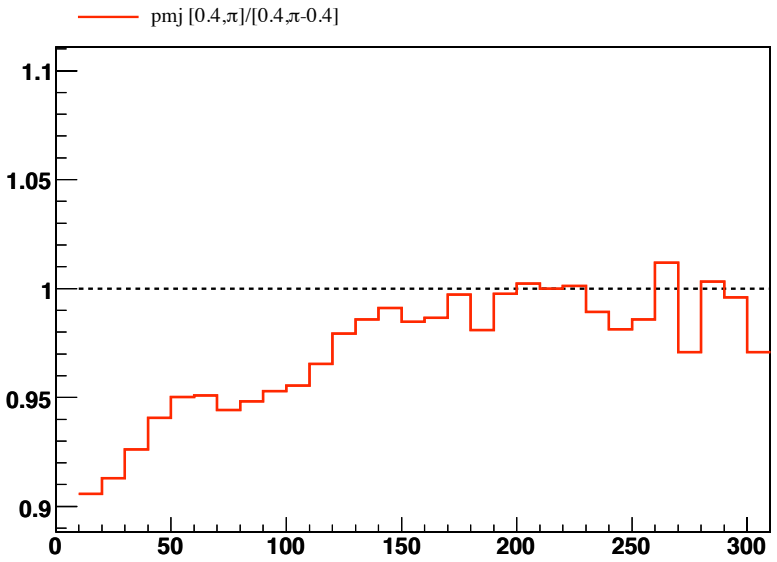

Figure 4.6: ratio between the $\not\!\!E_T$ distributions of two different QCD estimation: one with the nominal TPM ($0.4 < \Delta\phi(\not\!\!E_T - \text{jet}) < \pi$) and the other using jets with $\Delta\phi \in [0.4, \pi - 0.4]$.

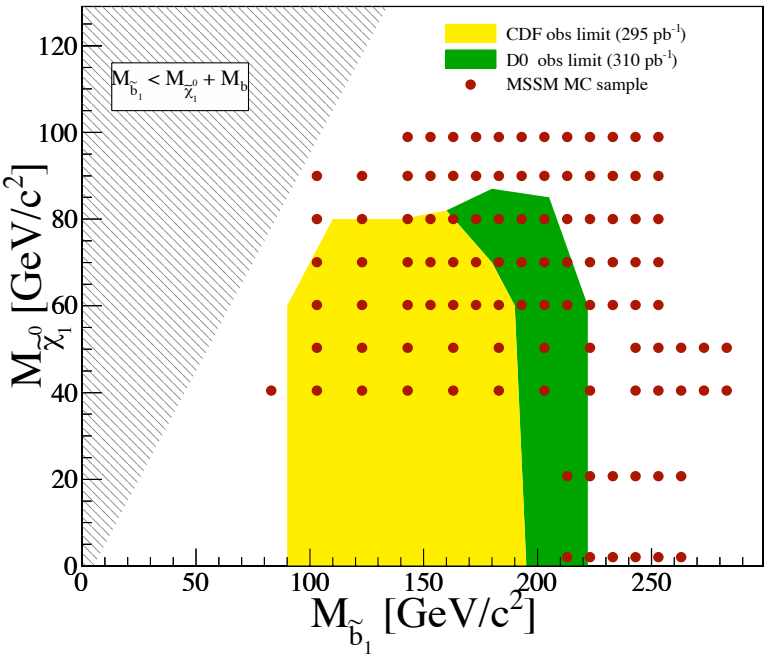

Figure 4.7: MSSM Monte Carlo production on sbottom-neutralino mass plane. Each point corresponds to a different MC sample with given masses. The dashed zone represents the previous limit from CDF Run II. The region above the diagonal is kinematically forbidden.

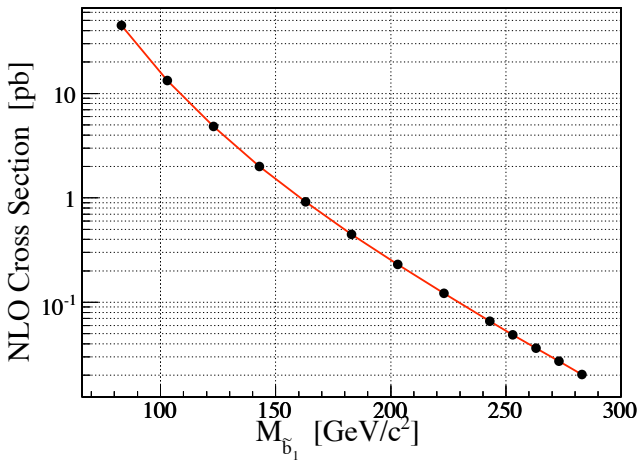

Figure 4.8: sbottom production cross section as a function of the sbottom mass according to NLO PROSPINO2 calculation. The cross section does not depend on the neutralino mass.

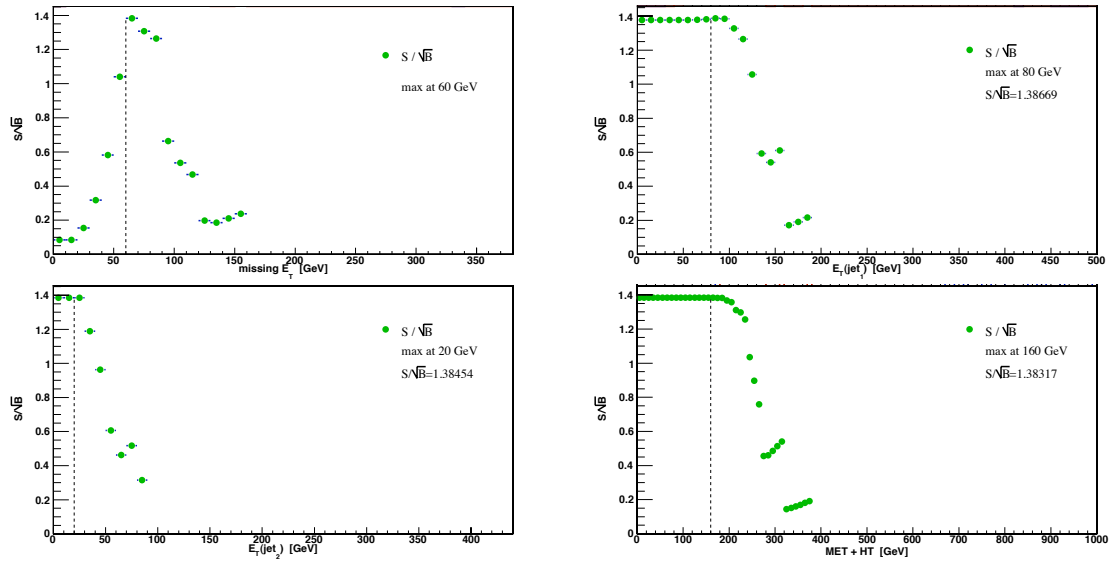

Figure 4.9: Values of $S/\sqrt{B}$ for different minimum thresholds on the four optimization variables: $\not\!\!E_T$ (top-left), $E_T(\text{jet}_1)$ (top-right), $E_T(\text{jet}_2)$ (bottom-left), and H_T (bottom-right) in the Low ΔM signal region. For the $\not\!\!E_T$ distribution the pre-selection cuts are applied: $S/\sqrt{B}$ peaks with $\not\!\!E_T > 60\ GeV$. For the $E_T(\text{jet}_1)$ distribution events are selected with pre-selection cuts and $\not\!\!E_T > 60\ GeV$: $S/\sqrt{B}$ has a maximum at $E_T(\text{jet}_1) > 80\ GeV$. These final cuts on $\not\!\!E_T$ and E_T are then applied for the $E_T(\text{jet}_2)$ distribution peaking at $E_T(\text{jet}_2) > 25\ GeV$. Finally, after applying also the cut on $E_T(\text{jet}_2)$, there is no optimal threshold on $H_T + \not\!\!E_T$.

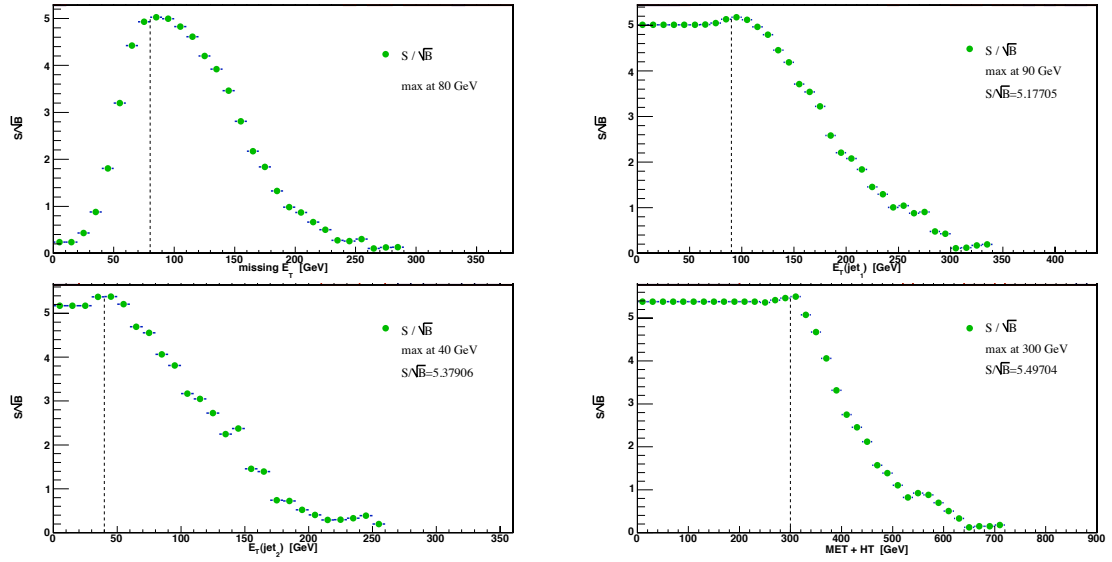

Figure 4.10: Values of $S/\sqrt{B}$ for different minimum thresholds on the four optimization variables: $\not\!\!E_T$ (top-left), $E_T(\text{jet}_1)$ (top-right), $E_T(\text{jet}_2)$ (bottom-left), and H_T (bottom-right) in the Low ΔM signal region. For the $\not\!\!E_T$ distribution the pre-selection cuts are applied: $S/\sqrt{B}$ peaks with $\not\!\!E_T > 80\ GeV$. For the $E_T(\text{jet}_1)$ distribution events are selected with pre-selection cuts and $\not\!\!E_T > 80\ GeV$: $S/\sqrt{B}$ has a maximum at $E_T(\text{jet}_1) > 90\ GeV$. These final cuts on $\not\!\!E_T$ and E_T are then applied for the $E_T(\text{jet}_2)$ distribution peaking at $E_T(\text{jet}_2) > 40\ GeV$. Finally, after applying also the cut on $E_T(\text{jet}_2)$, the optimal threshold on $H_T + \not\!\!E_T$ is $300\ GeV$.

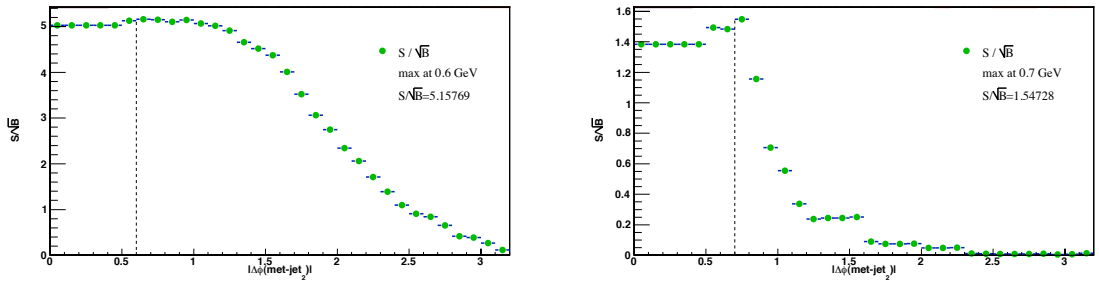

Figure 4.11: minimum threshold on the azimuthal separation $\Delta\phi(\not\!\!E_T - \text{jet}_2)$ between the $\not\!\!E_T$ and the direction of the second leading jet in the low (bottom) and high (top) ΔM regions.

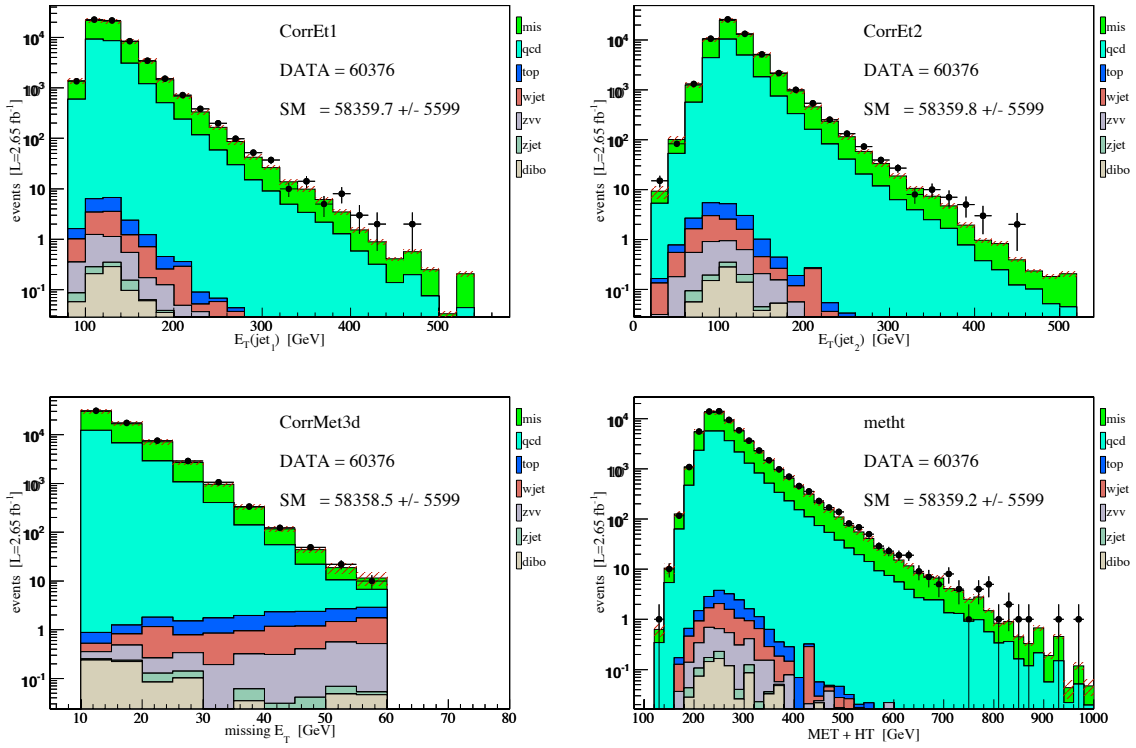

Figure 4.12: From top to bottom, clockwise: $E_T(\text{jet}_1)$, $E_T(\text{jet}_2)$, $\not\!\!E_T$, and $\not\!\!E_T + H_T$ distributions in the low $\not\!\!E_T$ control region for the low ΔM selection. Data are compared to SM predictions with total systematic uncertainties.

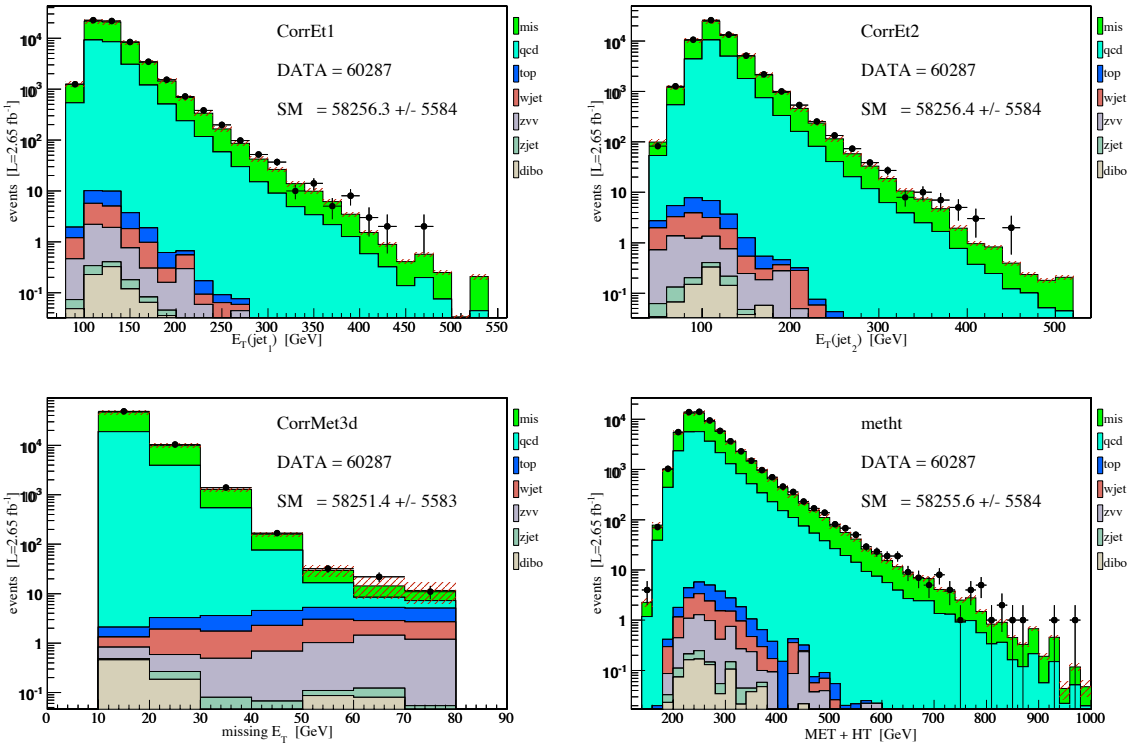

Figure 4.13: From top to bottom, clockwise: $E_T(\text{jet}_1)$, $E_T(\text{jet}_2)$, $\not\!\!E_T$, and $\not\!\!E_T + H_T$ distributions in the low $\not\!\!E_T$ control region for the high ΔM selection. Data are compared to SM predictions with total systematic uncertainties.

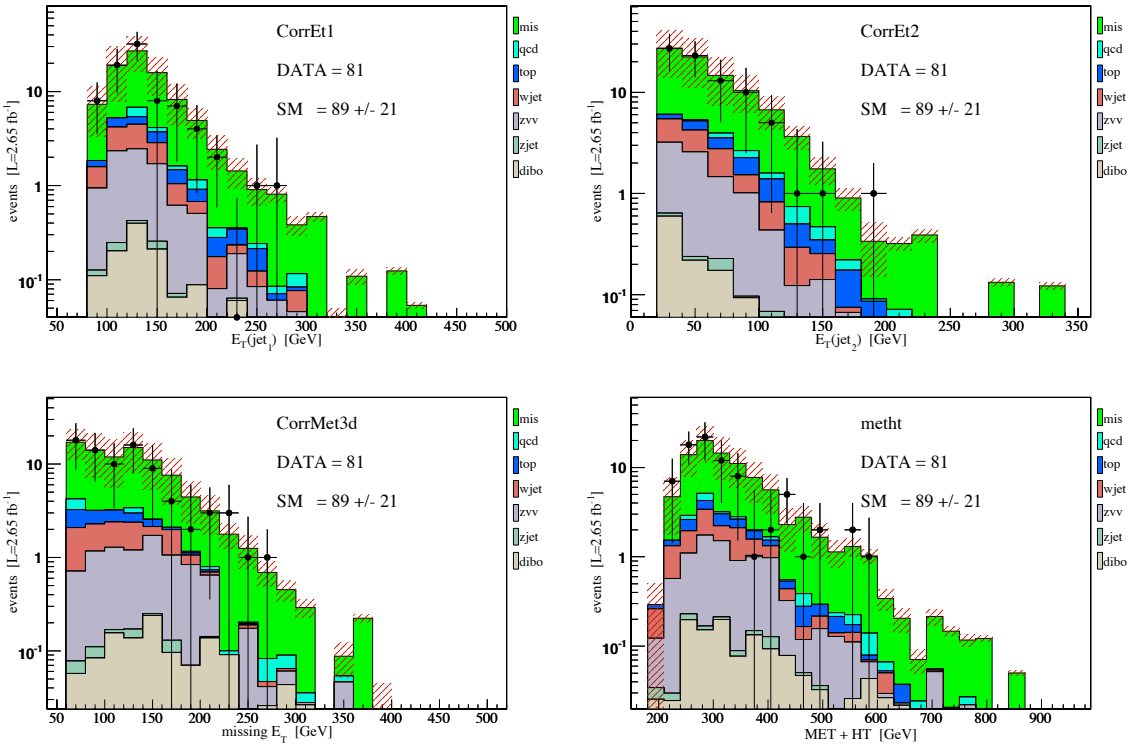

Figure 4.14: From top to bottom, clockwise: $E_T(\text{jet}_1)$, $E_T(\text{jet}_2)$, $\not\!\!E_T$, and $\not\!\!E_T + H_T$ distributions in the loose-not-tight tag control region for the low ΔM selection. Data are compared to SM predictions with total systematic uncertainties.

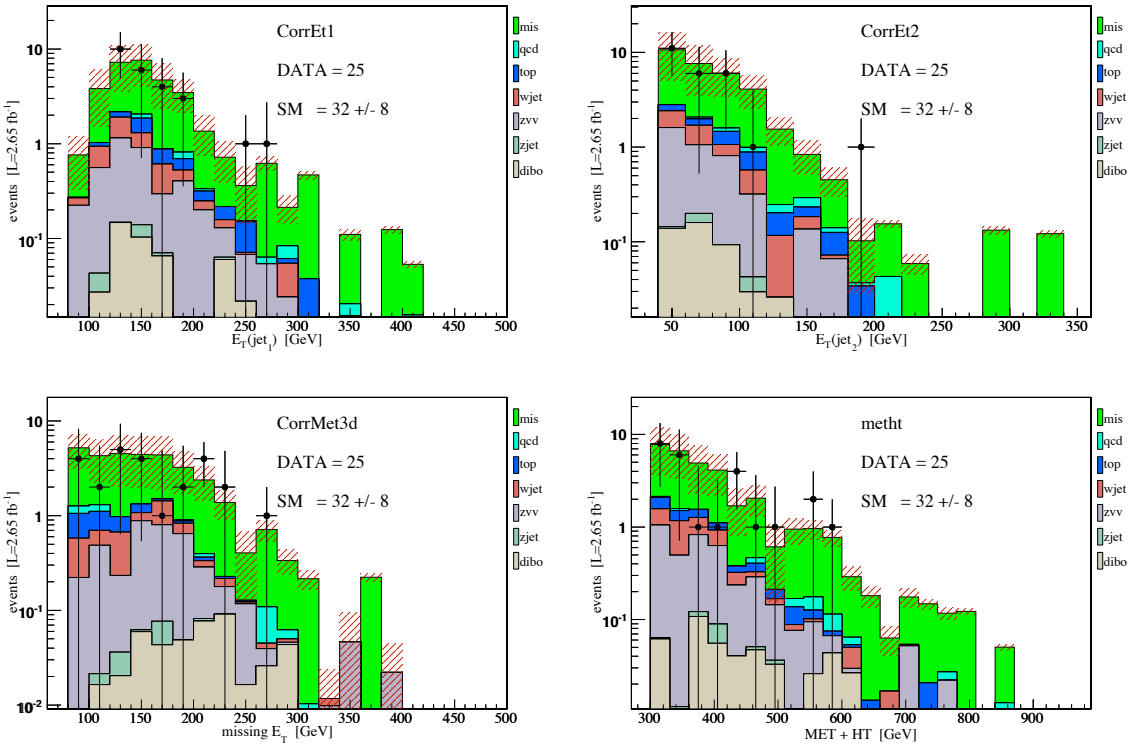

Figure 4.15: From top to bottom, clockwise: $E_T(\text{jet}_1)$, $E_T(\text{jet}_2)$, $\not\!\!E_T$, and $\not\!\!E_T + H_T$ distributions in the loose-not-tight tag control region for the high ΔM selection. Data are compared to SM predictions with total systematic uncertainties.

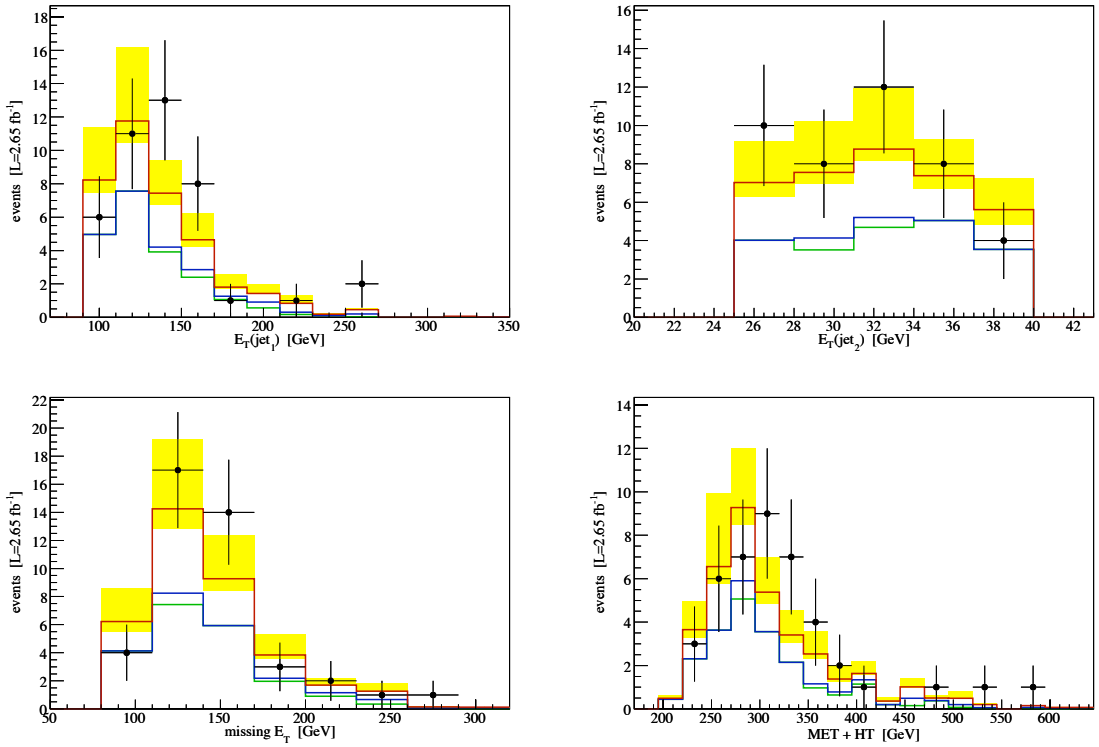

Figure 4.16: from top to bottom, clockwise: $E_T(\text{jet}_1)$, $E_T(\text{jet}_2)$, $\not\!\!E_T$, and $\not\!\!E_T + H_T$ distributions in the $E_T(\text{jet}_2)$ reversed control region for the high ΔM selection. Data are compared to SM predictions with total systematic uncertainties.

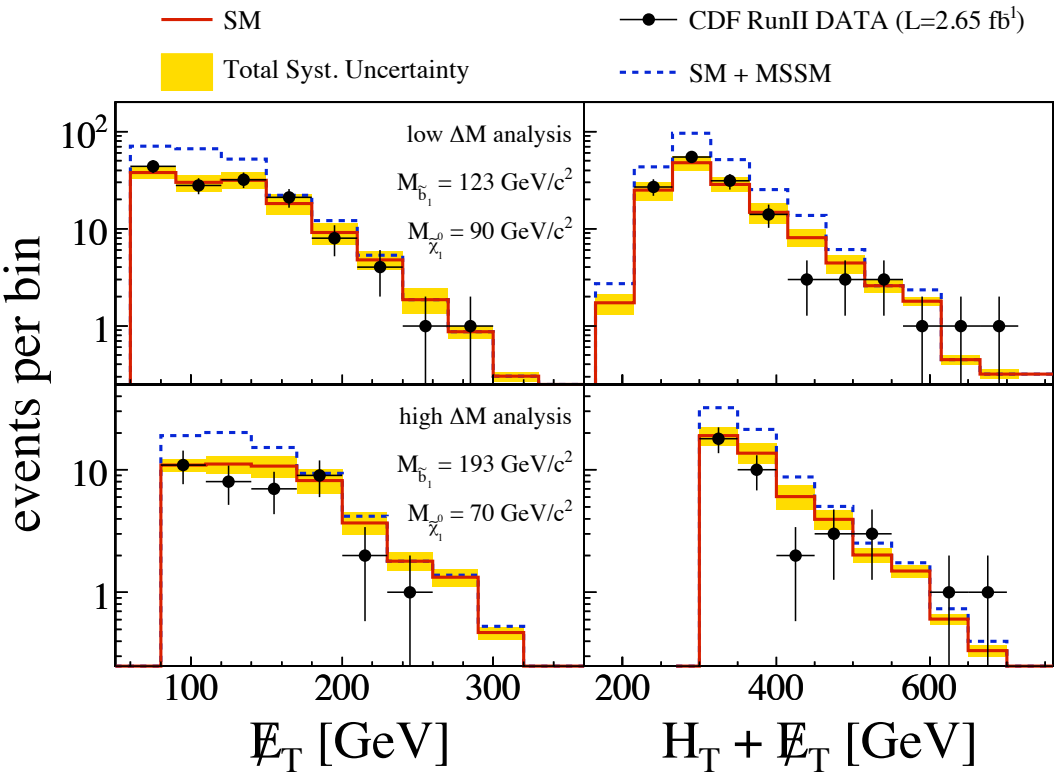

Figure 4.17: distributions of measured $\not\!\!E_T$ and $H_T + \not\!\!E_T$ distributions (black dots) for low ΔM (top) and high ΔM analyses (bottom), compared to the SM predictions (solid lines) and the SM+MSSM predictions (dashed lines). The shaded bands show the total systematic uncertainty on the SM predictions.

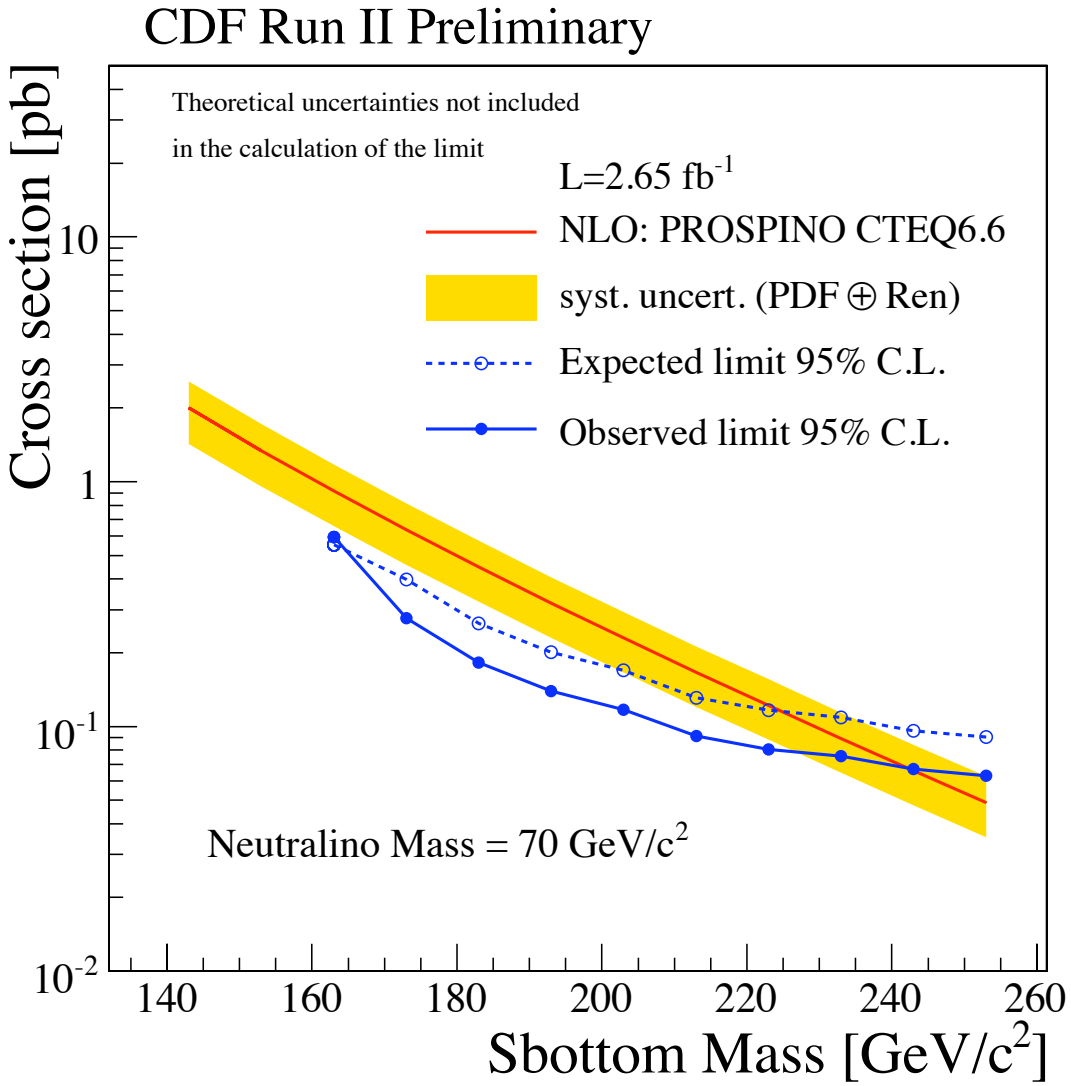

Figure 4.18: observed (solid lines) and expected (dashed lines) 95% CL upper limits on the inclusive squark and gluino production cross sections as a function of $M_{\tilde{b}_1}$ for a neutralino mass of 70 GeV/c^2 compared to NLO mSUGRA predictions (dashed-dotted lines). The yellow band denotes the total uncertainty on the theory.

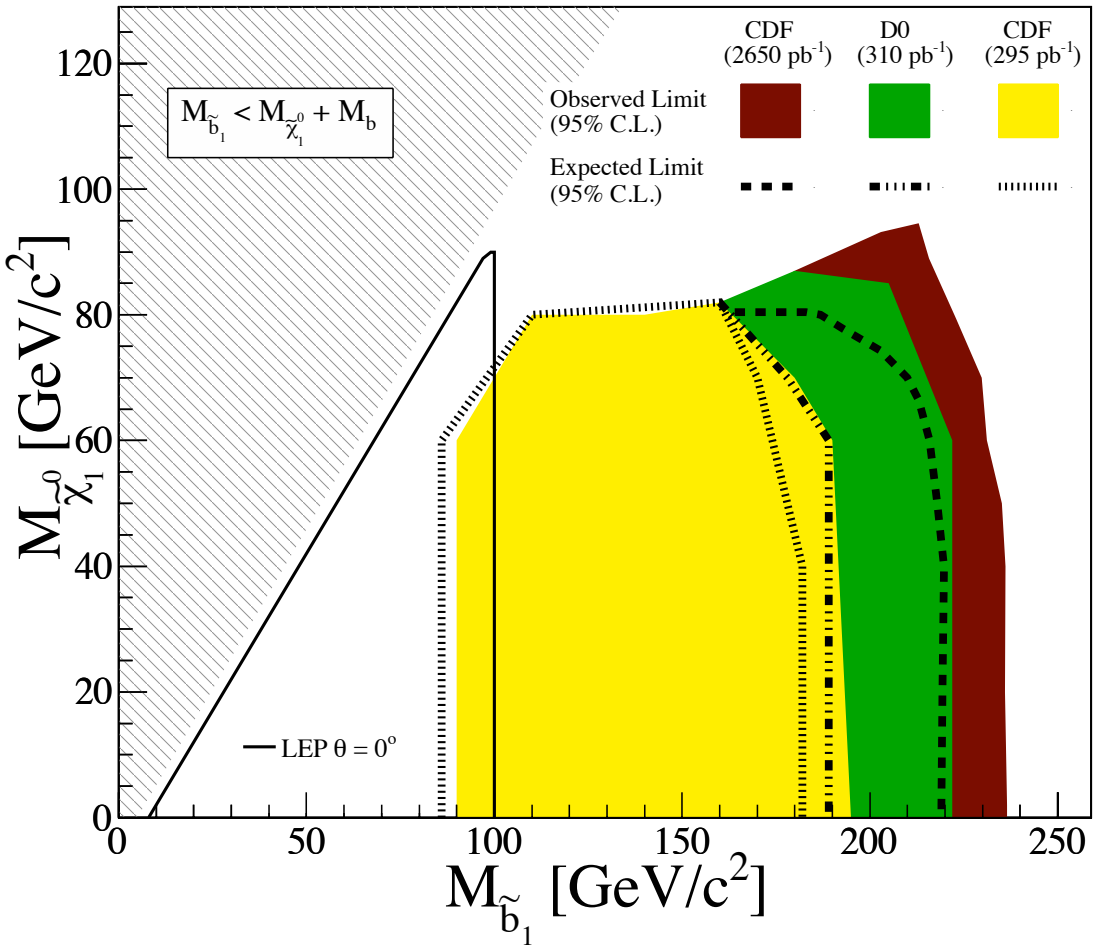

Figure 4.19: exclusion plane at 95% CL as a function of sbottom and neutralino masses. The observed and expected limits from this analysis are compared to previous results from CDF and D0 experiments at the Tevatron in Run II, and from LEP experiments at CERN. The hatched area indicates the kinematically prohibited region in the plane.

Chapter 5

Conclusions

This thesis reports on two searches for the production of squarks and gluinos, supersymmetric partners of the Standard Model (SM) quarks and gluons, using the CDF detector at the Tevatron $\sqrt{s} = 1.96$ TeV $p\bar{p}$ collider.

An inclusive search for squarks and gluinos pair production is performed in events with large $\not\!\!E_T$ and multiple jets in the final state, based on 2 fb^{-1} of CDF Run II data. The analysis is performed within the framework of minimal supergravity (mSUGRA) and assumes R-parity conservation where sparticles are produced in pairs. The expected signal is characterized by the production of multiple jets of hadrons from the cascade decays of squarks and gluinos and large missing transverse energy $\not\!\!E_T$ from the lightest supersymmetric particles (LSP). The measurements are in good agreement with SM predictions for backgrounds. The results are translated into 95% confidence level (CL) upper limits on production cross sections and squark and gluino masses in a given mSUGRA scenario. An upper limit on the production cross section is placed in the range between 1 pb and 0.1 pb, depending on the gluino and squark masses considered. The result of the search is negative for gluino and squark masses up to 392 GeV/c^2 in the region where gluino and squark masses are close to each other, gluino masses up to 280 GeV/c^2 regardless of the squark mass, and gluino masses up to 423 GeV/c^2 for squark masses below 378 GeV/c^2. These results are compatible with the latest limits on squark/gluino production obtained by the DØ Collaboration and considerably improve the previous exclusion limits from direct and indirect searches at LEP and the Tevatron.

The inclusive search is then extended to a scenario where the pair production of sbottom squarks is dominant. The new search is performed in a generic MSSM scenario with R-parity conservation. A specific SUSY particle mass hierarchy is assumed such that the sbottom decays exclusively as $\tilde{b}_1 \to b\tilde{\chi}_1^0$. The expected signal for direct sbottom pair production is characterized by the presence of two jets of hadrons from the hadronization of the bottom quarks and $\not\!\!E_T$ from the two LSPs in the final state. The events are selected with large $\not\!\!E_T$ and two energetic jets in the final state, and at least one jet is required to be associated with a b quark. The measurements are in good agreement with SM predictions for backgrounds. The results are translated into 95% CL exclusion limits on production cross sections and sbottom and neutralino masses in the given MSSM scenario. Cross sections down to 0.1 pb are excluded for the sbottom mass range considered. Sbottom masses up to 230 GeV/c^2 are excluded at 95% CL for neutralino masses below 70 GeV/c^2. This analysis increases the previous CDF limit by more than 40 GeV/c^2.

The sensitivity of both the inclusive and the exclusive search is dominated by systematic

effects and the results of the two analyses can be considered as conclusive for CDF Run II. With the new energy frontier of the newly commissioned Large Hadron Collider in Geneva, the experience from Tevatron will be of crucial importance in the developing of effective strategies to search for SUSY in the next era of particle physics experiments.

Bibliography

[1] H. E. HaberandG. L. Kane, *Phys. Rep.* **117**, 75 (1985).

[2] J. WessandB. Zumino, *Phys. Lett.* **49B**, 52 (1974);
H. Georgi, H. Quinn, and S. Weinberg, *Phys. Rev. Lett.* **33** 451 (1974).

[3] P. W. Higgs, *Phys. Lett.*, **12** 132 (1964).

[4] ALEPH, DELPHI, L3 and OPAL Collaborations, *Phys. Lett.* **B565** 61 (2003) arXiv:hep-ex/0306033.

[5] LEP ALEPH, DELPHI, L3, and OPAL Collaborations, arXiv:hep-ex/0712.0929 (2007).

[6] CDF and DØ Collaborations arXiv:hep-ex/0903.4001v1 (2009).

[7] L. Susskind, *Phys. Rev.* **D20** 2619 (1979).

[8] L. Maiani, *Proc. Summer School on Particle Physics*, Gif-sur-Yvette, 1979 (IN2P3, Paris, 1980) p.3;
G't Hooft et al., eds. *Recent Developments in Field Theories* (Plenum Press, new York (1980);
E. Witten, *Nucl. Phys.* **B188** 513 (1981);
R.K. Kaul, *Phys. Lett.* **B109** 19 (1982).

[9] H. E. Haber, *Recent Directions in Particle Theory, Proceedings of the 1992 Theoretical Advanced Study Institute in Elementary Particle Physics*, ed. J. Harvey and J. Polchinski (World Scientific, Singapore, 1993) pp. 589-686.

[10] D. Gross and R.Jackiw, *Phys. Rev.* **D6** 477 (1972);
C. Bouchiat, J. Iliopoulos and P. Meyer, *Phys. Lett.* **B38** 519 (1972);
H. Georgi and S. Glashow, *Phys. Rev.* **D6** 429 (1972);
L. Alvarez-Gaume and E. Witten, *Nucl. Phys.* **B234** 269 (1983).

[11] J.F. Gunion, H. E. Haber, G. Kane, S. Dawson, *The Higgs hunter's guide*, Addison Wesley (1990) Chapter 4.

[12] S. Dawson, arXiv:hep-ph/9712464.

[13] S. Dimopoulos and H. Georgi, *Nucl. Phys.* **B193** 150 (1981);
N. Sakai, *Z. Phys.* **C11** 153 (1981);
P. Fayet, *Phys. Lett.* **B69** 489 (1977).

[14] S. Weinberg, *Phys. Rev.* **D26** 287 (1982);
N. Sakai and T. Yanagida, *Nucl. Phys.* **B197** 533 (1982);
S. Dimopoulos, S. Raby, and F. Wilczek, *Phys. Lett.* **B112** 133 (1982);
J. Ellis, D. Nanoupoulos and S. Rudaz, *Nucl. Phys.* **B202** 43 (1982).

[15] G. Farrar and P. Fayet, *Phys. Lett.* **B76** 575 (1987);
F. Zwirner, *Phhys. Lett.* **132B** 103 (1983);
L. Hall and M. Suzuki, *Nucl. Phys.* **B231** 419 (1984);
J. Ellis, G. Gelmini, C. Jarlskog, G. Ross, and J. Valle, *Phys. Lett.* **B150** 142 (1985);
G. Ross and J. Valle, *Phys. Lett.* **B151** 375 (1985);
S. Dawson, *Nucl. Phys.* **B261** 297 (1985);
S. Dimopoulos and L. Hall, *Phys. Lett.* **B207** 210 (1988).

[16] C. Carlson, P. Roy, and M. Sher, *Phys. Lett.* **B357** 99 (1995).

[17] G. Bhattacharyya, arXiv:hep-ph/9608415.

[18] D. J. H. Chung, L. L. Everett, G.L. Kane, S. F. King, J. Lykken and Lian-Tao Wang, *Phys. Rept.* **407** (2005) 1.

[19] H. P. Nilles, *Phys. Rep.* **110**, 1 (1984);
A.H. Chamseddine, R. Arnowitt, and P. Nath *Phys. Rev. Lett.* **49** 970 (1982);
R. Barbieri, S. Ferrara, and C. A. Savoy *Phys. Lett.* **B119** 343 (1982);
L.J. Hall, J. Lykken, and S. Weinberg *Phys. Rev.* **D27** 2359 (1983) .

[20] L.E. Ibez and C. Lpez, *Nucl. Phys.* **B233** 511 (1984);
L.E. Ibez and C. Lpez, *Nucl. Phys.* **B256** 218 (1985).

[21] H. Baer, C. Chen, F. Paige, X. Tata, G.L. Kane, C. Kolda, L. Roszkowski, J.D. Wells, *Phys. Rev.* **D54** 5866 (1996).

[22] M. Carena, S. Pokorski, M. Olechowski, C.E.M. Wagner, *Nucl. Phys.* **B426** 269 (1994), arXiv:hep-ph/9402253.

[23] W. Beenakker, R. Hpker, M. Spira and P. M. Zerwas, *Nucl. Phys.* **B492** 51 (1997), arXiv:hep-ph/9610490.

[24] T.Aaltonen et al., (CDF Collaboration), *Phys. Rev. Lett.* **102** 221801 (2009)

[25] T.Aaltonen et al., (CDF Collaboration), *Phys. Rev.* **D76** 072010 (2007).

[26] J. Pumplin, D.R. Stump, J. Huston, H.L. Lai, P. Nadolsky, and W.K. Tung, *J. High Energy Phys.* **07**, 012 (2002). (arXiv:hep-ph/0201195).

[27] D. Sutmp, J. Huston, J. Pumplin, and W. Tung, hep-ph/0303013.
A.D. Martin, R. G. Roberts, W. J. Stirling, and R.S. Thorne, hep/ph-0211080.
J. Pumplin, D. Stump, R. Brock, D. Casey, and J. Huston, hep-ph/0101032.

[28] M. Bengtsson, T. Sjstrand, *Z. Phys.* **C37** 465 (1988).

[29] B. Andersson, G. Gustafson and B. Söderberg, *Z. Phys.* **C20** 317 (1983), *Nucl. Phys.* **B264** 29 (1986).
B. Andersson, G. Gustafson, G. Ingelman and T. Sjöstrand, *Phys. Rep.* **97** 33 (1983).

[30] B.R. Webber, *Nucl. Phys.* **B238** 492 (1984).

[31] D. Amati and G. Veneziano, emphPhys. Lett. **B83** 87 (1979);
A. Bassetto, M. Ciafaloni and G. Marchesini, *Phys. Lett.* **B83** 207 (1979);
G. Maschesini, L. Trentadue and G. Veneziano, *Nucl. Phys.* **B181** 335 (1980).

[32] T. Sjöstrand et al. *Computer Phys. Commun.* 135 (2001)

[33] Michelangelo Mangano et. al., *JHEP* **0307** (2003) 001, hep-ph/0206293.

[34] F. Paige and S. Protopopescu, in *Supercollider Physics*, p. 41, ed. D. Soper (WorldScientific, 1986).

[35] T. Affolder et al. (CDF Collaboration), *Phys.Rev.* **D65**, 092002 (2002).

[36] R. Brunet al., *Tech. Rep.* **CERN-DD/EE/84-1**, 1987;
GEANT Detector Description and Simulation Tool CERN Program Library Long Writeup W5013 (1993).

[37] A. Abulencia et al. (CDF Collaboration), *J. Phys. G: Nucl. Part. Phys.* **34**, 2457 (2007).

[38] M. Cacciari et al., *High Energy Phys.* **0404**, 068 (2004).

[39] J. Alwall, et al., JHEP 09, 028 (2007), arXiv:0706.2334.

[40] J. Campbell and R. K. Ellis, *MCFM: A Monte Carlo for FeMtobarn processes at Hadron Colliders. Phys. Rev.* **D60**, 113006 (1999).

[41] G.L. Kane and J.P. Leveille, *Phys. Lett.* **B112** 227 (1992);
P.R. Harrison and C.H. Llewellyn Smith, *Nucl. Phys.* **B223** 542 (1983);
E. Reya and D.P. Roy, *Phys. Rev.* **D32** 645 (1985);
S. Dawson, E. Eichten and C. Quigg, *Phys. Rev.* **D31** 1581 (1985);
H. Baer and X. Tata, *Phys. Lett.* **B160** 159 (1985).

[42] W. Beenakker, R. Höpker, M. Spira and P.M. Zerwas, *Phys. Rev. Lett.* **74** 2905 (1995);
W. Beenakker, R. Höpker, M. Spira and P.M. Zerwas, *Z. Phys.* **C69** 163 (1995).

[43] W. Beenakker, R. Höpker, and M. Spira, *PROSPINO: A Program for the Production of Supersymmetric Particles in Next-To-Leading Order QCD.*

[44] C.W.Schmidt, The Fermilab 400-MeV Linac Upgrade, FERMILAB-CONF-93-111 (1993).

[45] Fermilab Beam Division, *Run II Handobook*, http://www-bd.fnal.gov/runII/index.html .

[46] D. Acostaet al. (CDF Collaboration), *Phys. Rev.* **D71**, 032001 (2005).
R. Blair et al. (CDF-II Collaboration), *The CDF-II detector: Technical design report*, FERMILAB-PUB-96-390-E (1996).

[47] A. Sill et al., *Nucl. Instrum. Meth.* **A447**, (2000) 1-8 .

[48] T.Affolder et al., *Nucl. Instrum. Meth.* **A526** (2004) 249.

[49] D. Acosta et al., *Nucl. Instrum. Meth.* **A518**, (2004) 605.

[50] L. Balka et al., *Nucl. Instrum. Meth.* **A267**, (1988) 272.

[51] S. Bertolucci et al., *Nucl. Instrum. Meth.* **A301**, (1988) 267.

[52] G. Apollinari et al., *Proceedings of the Fourth International Conference on Calorimetry in High Energy Physics, World Scientific, Singapore*, p. 200, (1994).

[53] S. Kuhlmann et al., *Nucl. Instrum. Meth.* **A518**, (2004) 39-41.

[54] G. Apollinari et al., *Nucl. Instrum. Meth.* **A412**, (1998) 515-526.

[55] F. Abe et al., *Phys. Rev. Lett.* **73**,(1994) 2662.

[56] M. Albrow et al., *Nucl. Instrum. Meth.* **A431** (1999) 104.

[57] C. M. Ginsburg, The CDF Collaboration, FERMILAB-CONF-03/386-E *Published Proceedings International Europhysics Conference on High-Energy Physics* (HEP 2003), *Aachen,Germany*, July 17-23, 2003.

[58] D. Acosta et al. (CDF Collaboration), *The CDF Cherenkov luminosity monitor*, *Nucl. Instrum. Meth.* **A461**, (2001) 540.

[59] CDF-7446 Lum. Group, *Luminosity Uncertainty for Run II up until August 2004*; S. Klimenko et al., FERMILAB-FN-0741 (2003); D. Acosta *et al.*, *Nucl. Instrum. Meth.* **A494**, (2002) 57.

[60] F. Abe et al. (CDFCollaboration), *Phys. Rev.* **D45**, 1448 (1992).

[61] A. Bhatti et al., *Nucl. Instrum. Methods* **A566**, 375 (2006);
CDF Collaboration, *Run2 JES summary*, hep-ex/0510047.

[62] A. Ivanov, E. Halkiadakis, A. Hocker, P. Tipton, *A Study of Missin E_T resolution in the $Z \to \mu\mu$ Sample CDF internal note* 6462 (2003).

[63] D. Acosta et al. (CDF Collaboration), *Measurement of the $t\bar{t}$ production cross section in $p\bar{p}$ collisions at $\sqrt{s} = 1.96$ TeV using lepton + jets events with secondary vertex b-tagging*, *Phys. Rev.* **D71** (2005) 052003.

[64] B. C. Allanachet al., *Eur. Phys. J.* **C25**, 113 (2002).

[65] A. Abulencia et al., *Phys. Rev. Lett.* **96** 122001 (2006).

[66] T. Aaltonen et al. (CDF Collaboration), *Phys. Rev. Lett.* **100**, 102001 (2008).

[67] R. Cousins, *Am. J. Phys.* **63**, 398 (1995).

[68] B. Abbott et al. (DØ Collaboration), *Phys. Rev. Lett.* **83** 4937 (1999). T. Affolder et al. (CDF Collaboration), *Phys. Rev. Lett.* **88** 041801 (2002).

[69] C. Albajar et al. (UA1 Collaboration), Phys. Lett. **B198** 261 (1987).

[70] S. Albachi et al. (UA2 Collaboration), Phys. Lett. **B235** 363 (1990).

[71] C. Albajar et al. (UA1 Collaboration), *Phys.Lett.* **B198**, 261 (1987); J. Alitti et al. (UA2 Collaboration), *Phys.Lett.* **B**, 363 (1990).

[72] The LEP-SUSY working group: *http://lepsusy.web.cern.ch/lepsusy/*

[73] V.M. Abazov et al., The DØ Collaboration, *Phys. Lett.* **B**, 660, 449 (2008).

[74] Daniel Joseph Sherman, (Harvard U.), *Ph.D. Thesis* FERMILAB-THESIS-2007-82, (2007).

[75] D. Acosta et al. (CDF Collaboration), *Phys. Rev.* **D71**, 052003 (2005).

[76] T. Aaltonen et al., The CDF Collaboration, *Phys. Rev. Lett.* **101** 252001 (2008).

[77] T. Aaltonen et al., The CDF Collaboration, *Phys. Rev. Lett.* **103**, 221801 (2009), Fermilab-Pub-09-341-E., arXiv: 0907.0810 .

[78] V.M. Abazov et al., The DØ Collaboration, *Phys. Rev. Lett.* **97**, 171806 (2006).

[79] V.M. Abazov et al., The DØ Collaboration, *Conference Note* **5931**, (2009).

[80] Joel Heinrich, et al., arXiv:physics/0409129v1 (2004).

[81] J. Pumplin, D.R. Stump, J. Huston, H.L. Lai, P. Nadolsky, W.K. Tung, arXiv:hep-ph/0201195; JHEP 0207 012 (2002).

Appendix A

Tagging Probability Matrix for Heavy Flavour QCD Multijet

This Appendix is an extension of Section 4.6 where the data-driven technique used to estimate the contribution of QCD multijet events in the exclusive analysis is described. Tables from A.1 to A.8 display all the occupancies of the TPM bins and the correspondent statistical uncertainties. Figures A.1 through A.7 show the values of the TPM coefficients as a function of the kinematic variables of interest.

HF tag prob	$\not{E}_T$						
$2 \leq N_{trk} < 4$	10 - 20	20 - 30	30 - 40	40 - 50	50 - 60	60 - 70	70 - 1000
25< et <50	0.7%	0.81%	1%	1.3%	1.4%	1.7%	1.8%
50< et <70	0.73%	0.84%	1%	1.4%	1.5%	1.9%	1.5%
70< et <90	0.61%	0.66%	0.75%	0.96%	0.9%	0.91%	0.89%
90< et <110	0.42%	0.43%	0.56%	0.72%	0.58%	0.72%	0.96%
110< et <120	0.3%	0.34%	0.4%	0.42%	0.43%	0.68%	0.54%
120< et <130	0.29%	0.22%	0.33%	0.45%	0.38%	0.73%	0.79%
130< et <140	0.23%	0.27%	0.25%	0.32%	0.26%	0.27%	0.43%
140< et <150	0.28%	0.21%	0.24%	0.12%	0.055%	0.21%	0.77%
150< et <1000	0.2%	0.2%	0.19%	0.13%	0.27%	0.27%	0.3%

stat uncert	$\not{E}_T$						
$2 \leq N_{trk} < 4$	10 - 20	20 - 30	30 - 40	40 - 50	50 - 60	60 - 70	70 - 1000
25< et <50	2.2%	2.3%	3%	4.3%	6%	7.9%	6.8%
50< et <70	3.5%	3.7%	4.8%	6%	7.7%	8.9%	9.9%
70< et <90	3.9%	4%	5%	6.5%	9.9%	15%	15%
90< et <110	3.5%	3.9%	5.3%	7.7%	13%	17%	16%
110< et <120	4.1%	4.6%	6.4%	10%	17%	21%	31%
120< et <130	4.6%	5.3%	6.6%	9.4%	16%	20%	24%
130< et <140	6.1%	6.1%	8.1%	11%	19%	25%	29%
140< et <150	7.3%	7.9%	9.6%	16%	29%	33%	21%
150< et <1000	6.3%	5.9%	6.7%	9.3%	11%	15%	13%

Table A.1: TPM $\not{E}_T$ and E_T bin contents (top) and relative statistical uncertainty (bottom) for $2 \leq NT < 4$.

HF tag prob	$\not\!\!E_T$						
$N_{trk} = 4$	10 - 20	20 - 30	30 - 40	40 - 50	50 - 60	60 - 70	70 - 1000
25< et <50	1.6%	1.9%	2.2%	2.8%	3.4%	3.7%	4.1%
50< et <70	1.7%	1.9%	2.3%	3.2%	3.6%	4.6%	3.7%
70< et <90	1.5%	1.6%	2.2%	2.1%	2.3%	2.3%	2.4%
90< et <110	1.1%	1.2%	1.6%	1.6%	1.8%	2.1%	1.5%
110< et <120	0.85%	0.86%	0.96%	1.2%	1.2%	1.6%	2.3%
120< et <130	0.85%	0.78%	0.81%	0.86%	1.2%	2%	1.4%
130< et <140	0.64%	0.73%	0.75%	0.67%	0.99%	0.95%	1.7%
140< et <150	0.68%	0.64%	0.58%	0.83%	0.77%	0.71%	1.5%
150< et <1000	0.81%	0.57%	0.58%	0.7%	0.52%	0.62%	1%

stat uncert	$\not\!\!E_T$						
$N_{trk} = 4$	10 - 20	20 - 30	30 - 40	40 - 50	50 - 60	60 - 70	70 - 1000
25< et <50	1.7%	1.8%	2.4%	3.4%	4.8%	6.4%	5.4%
50< et <70	2.5%	2.7%	3.5%	4.3%	5.5%	6.5%	6.9%
70< et <90	2.7%	2.7%	3.2%	4.7%	6.8%	10%	10%
90< et <110	2.4%	2.6%	3.6%	5.6%	8.3%	12%	13%
110< et <120	2.8%	3.2%	4.6%	7%	11%	16%	14%
120< et <130	3%	3.4%	4.7%	7.4%	11%	14%	18%
130< et <140	4.1%	4.2%	5.6%	8.5%	11%	18%	16%
140< et <150	5.1%	5.2%	6.9%	9.2%	15%	24%	17%
150< et <1000	3.9%	4%	4.6%	5.7%	8.4%	11%	8.4%

Table A.2: TPM $\not\!\!E_T$ and E_T bin contents (top) and relative statistical uncertainty (bottom) for $NT = 4$.

HF tag prob	$\not\!\!E_T$						
$N_{trk} = 5$	10 - 20	20 - 30	30 - 40	40 - 50	50 - 60	60 - 70	70 - 1000
25< et <50	2.1%	2.4%	3%	3.9%	5.1%	6%	5.1%
50< et <70	2.2%	2.5%	3.2%	4.2%	5.1%	5.5%	5.5%
70< et <90	2.1%	2.2%	2.8%	3%	3.7%	3.1%	4.7%
90< et <110	1.6%	1.8%	1.9%	2.2%	2.4%	2.9%	2.1%
110< et <120	1.5%	1.4%	1.6%	1.8%	2%	2.5%	2.7%
120< et <130	1.4%	1.3%	1.2%	1.5%	2.4%	2.8%	2.9%
130< et <140	1.2%	1.2%	1.3%	1.5%	1.7%	2.1%	3.2%
140< et <150	1.1%	1.3%	1.1%	1.4%	1.5%	1.6%	1.8%
150< et <1000	1.2%	1.1%	1%	1.2%	1.4%	1.2%	1.8%

stat uncert	$\not\!\!E_T$						
$N_{trk} = 5$	10 - 20	20 - 30	30 - 40	40 - 50	50 - 60	60 - 70	70 - 1000
25< et <50	1.5%	1.6%	2.1%	2.9%	3.9%	5.1%	4.9%
50< et <70	2%	2.1%	2.6%	3.4%	4.2%	5.8%	5.7%
70< et <90	2%	2%	2.5%	3.6%	4.9%	7.5%	6.7%
90< et <110	1.7%	1.9%	2.8%	4.3%	6.6%	9.5%	10%
110< et <120	2%	2.3%	3.4%	5.3%	8.1%	12%	12%
120< et <130	2.2%	2.5%	3.6%	5.4%	7.5%	11%	12%
130< et <140	2.9%	3.1%	4.1%	5.8%	8.7%	13%	11%
140< et <150	3.7%	3.7%	5%	6.9%	10%	16%	16%
150< et <1000	2.8%	2.8%	3.4%	4.2%	5.6%	7.9%	5.9%

Table A.3: TPM $\not\!\!E_T$ and E_T bin contents (top) and relative statistical uncertainty (bottom) for $NT = 5$.

HF tag prob	$\not\!\!E_T$						
$N_{trk} = 6$	10 - 20	20 - 30	30 - 40	40 - 50	50 - 60	60 - 70	70 - 1000
25< et <50	2.6%	3%	3.7%	4.7%	6.3%	6.8%	8.5%
50< et <70	2.8%	3.2%	4%	5.5%	6.5%	6.2%	7.2%
70< et <90	2.7%	3.1%	3.5%	4.2%	4.6%	5.1%	5.2%
90< et <110	2.3%	2.5%	2.8%	3.1%	3.9%	4.5%	4.6%
110< et <120	2%	2.1%	2%	2.4%	2.7%	4.7%	3.6%
120< et <130	1.8%	1.8%	1.8%	2.3%	2.2%	3.2%	4.3%
130< et <140	1.7%	1.7%	1.8%	2.3%	2.4%	2.4%	3.2%
140< et <150	1.7%	1.5%	1.8%	2%	2.6%	2.5%	2.7%
150< et <1000	1.7%	1.6%	1.6%	1.7%	1.5%	1.6%	2.6%

stat uncert	$\not\!\!E_T$						
$N_{trk} = 6$	10 - 20	20 - 30	30 - 40	40 - 50	50 - 60	60 - 70	70 - 1000
25< et <50	1.4%	1.5%	2%	2.8%	3.8%	5.1%	4.2%
50< et <70	1.7%	1.8%	2.3%	2.9%	3.8%	5.2%	5%
70< et <90	1.6%	1.6%	2.1%	2.9%	4.3%	6.2%	6.4%
90< et <110	1.4%	1.6%	2.2%	3.5%	5.1%	7.5%	7.6%
110< et <120	1.6%	1.9%	2.9%	4.5%	7%	9.3%	12%
120< et <130	1.8%	2.1%	3%	4.5%	7.1%	9.8%	10%
130< et <140	2.4%	2.5%	3.5%	4.9%	7.5%	11%	11%
140< et <150	3%	3.2%	4%	5.7%	8.1%	12%	12%
150< et <1000	2.3%	2.3%	2.7%	3.5%	5%	6.6%	5%

Table A.4: TPM $\not\!\!E_T$ and E_T bin contents (top) and relative statistical uncertainty (bottom) for $NT = 6$.

HF tag prob	$\not\!\!E_T$						
$N_{trk} = 7$	10 - 20	20 - 30	30 - 40	40 - 50	50 - 60	60 - 70	70 - 1000
25< et <50	3%	3.5%	4.1%	5.2%	6.3%	8.1%	8.8%
50< et <70	3.1%	3.7%	4.9%	6.2%	7.4%	8.9%	8.9%
70< et <90	2.9%	3.3%	4.2%	5.2%	6.6%	6.5%	6.7%
90< et <110	2.7%	2.9%	3.4%	3.6%	4.4%	3.9%	4.8%
110< et <120	2.5%	2.7%	2.9%	3.3%	4.5%	4.9%	3.4%
120< et <130	2.3%	2.5%	2.7%	2.9%	4%	3.6%	5%
130< et <140	2.2%	2%	2.2%	2.6%	3.2%	4.8%	3.4%
140< et <150	2.1%	2.2%	2%	2.2%	3%	2.5%	4.4%
150< et <1000	2.2%	2%	2%	2.1%	2%	2.7%	3.3%

stat uncert	$\not\!\!E_T$						
$N_{trk} = 7$	10 - 20	20 - 30	30 - 40	40 - 50	50 - 60	60 - 70	70 - 1000
25< et <50	1.5%	1.6%	2.1%	3%	4.2%	5.5%	4.8%
50< et <70	1.6%	1.6%	2.1%	2.8%	3.7%	4.8%	4.7%
70< et <90	1.5%	1.5%	1.9%	2.6%	3.7%	5.7%	5.7%
90< et <110	1.2%	1.4%	2%	3.1%	4.7%	7.7%	7.6%
110< et <120	1.4%	1.7%	2.5%	4.1%	5.9%	8.9%	11%
120< et <130	1.6%	1.9%	2.6%	4.2%	6.1%	9.3%	8.6%
130< et <140	2.1%	2.3%	3.2%	4.7%	6.8%	9.1%	10%
140< et <150	2.7%	2.8%	3.8%	5.5%	7.6%	12%	9.5%
150< et <1000	2%	2%	2.5%	3.2%	4.4%	5.6%	4.5%

Table A.5: TPM $\not\!\!E_T$ and E_T bin contents (top) and relative statistical uncertainty (bottom) for $NT = 7$.

HF tag prob	$\not\!\!E_T$						
$N_{trk} = 8$	10 - 20	20 - 30	30 - 40	40 - 50	50 - 60	60 - 70	70 - 1000
25< *et* <50	3.4%	3.7%	4.5%	5.9%	7.1%	9.8%	9%
50< *et* <70	3.4%	4.2%	5.2%	7.3%	8.6%	10%	11%
70< *et* <90	3.4%	4%	4.8%	6.3%	7.1%	7.4%	8.4%
90< *et* <110	3.1%	3.6%	4.3%	5%	5.8%	5.4%	6.8%
110< *et* <120	2.9%	3%	3.3%	4.2%	4.5%	5%	6.3%
120< *et* <130	2.8%	3%	3.2%	4%	4.7%	4.8%	6.4%
130< *et* <140	2.5%	2.8%	3.2%	3.1%	4.2%	3.9%	5.3%
140< *et* <150	2.5%	2.7%	2.6%	2.8%	3.4%	4.2%	5.1%
150< *et* <1000	2.7%	2.7%	2.7%	2.8%	2.8%	3.1%	4.1%

stat uncert	$\not\!\!E_T$						
$N_{trk} = 8$	10 - 20	20 - 30	30 - 40	40 - 50	50 - 60	60 - 70	70 - 1000
25< *et* <50	1.2%	1.3%	1.8%	2.6%	3.6%	4.6%	4.4%
50< *et* <70	1.2%	1.2%	1.5%	2%	2.8%	3.7%	3.8%
70< *et* <90	1%	1%	1.3%	1.8%	2.7%	4.1%	4.3%
90< *et* <110	0.81%	0.9%	1.3%	2%	3.1%	5%	4.7%
110< *et* <120	0.96%	1.2%	1.8%	2.7%	4.3%	6.2%	6.8%
120< *et* <130	1.1%	1.3%	1.9%	2.8%	4.2%	6.2%	6.4%
130< *et* <140	1.4%	1.6%	2.1%	3.3%	4.6%	6.9%	6.7%
140< *et* <150	1.8%	1.9%	2.6%	3.8%	5.4%	7.8%	7.2%
150< *et* <1000	1.3%	1.3%	1.6%	2.2%	3%	4%	3.1%

Table A.6: TPM $\not\!\!E_T$ and E_T bin contents (top) and relative statistical uncertainty (bottom) for $8 \leq NT < 10$.

HF tag prob	$\not{E}_T$						
$N_{trk} = 10$	10 - 20	20 - 30	30 - 40	40 - 50	50 - 60	60 - 70	70 - 1000
25< et <50	3.4%	4.2%	4.9%	6.7%	8.3%	10%	11%
50< et <70	3.7%	4.6%	6.1%	8.5%	11%	13%	13%
70< et <90	3.6%	4.5%	5.8%	7.3%	8.8%	10%	11%
90< et <110	3.6%	4.3%	4.9%	6.5%	7.5%	7.8%	8%
110< et <120	3.4%	3.6%	4.3%	5.1%	5.1%	7.2%	5.9%
120< et <130	3.2%	3.5%	3.8%	4.8%	5.5%	6%	7%
130< et <140	3.3%	3.7%	3.7%	3.6%	5%	4.6%	5.8%
140< et <150	3.3%	3.3%	4.4%	4.3%	5.4%	4.7%	6%
150< et <1000	3%	3.4%	3.2%	3.7%	4.1%	3.6%	4.5%

stat uncert	$\not{E}_T$						
$N_{trk} = 10$	10 - 20	20 - 30	30 - 40	40 - 50	50 - 60	60 - 70	70 - 1000
25< et <50	1.7%	1.8%	2.4%	3.4%	4.8%	6.5%	6.4%
50< et <70	1.2%	1.2%	1.6%	2.1%	2.9%	4.1%	4.3%
70< et <90	0.96%	0.91%	1.2%	1.7%	2.6%	3.8%	4.2%
90< et <110	0.71%	0.78%	1.1%	1.7%	2.8%	4.3%	4.6%
110< et <120	0.86%	1.1%	1.6%	2.5%	3.9%	5.7%	6.4%
120< et <130	0.98%	1.2%	1.7%	2.6%	3.9%	5.8%	6%
130< et <140	1.2%	1.4%	2%	3%	4.2%	6.8%	6.7%
140< et <150	1.5%	1.7%	2.2%	3.3%	4.8%	6.9%	6.6%
150< et <1000	1.1%	1.2%	1.5%	1.9%	2.6%	3.6%	2.8%

Table A.7: TPM $\not{E}_T$ and E_T bin contents (top) and relative statistical uncertainty (bottom) for $10 \leq NT < 13$.

HF tag prob	$\not\!\!E_T$						
$N_{trk} = 13$	10 - 20	20 - 30	30 - 40	40 - 50	50 - 60	60 - 70	70 - 1000
25< et <50	2.1%	3.1%	4.3%	6.7%	8.6%	12%	4%
50< et <70	3.7%	4.7%	6.2%	7.3%	10%	13%	11%
70< et <90	3.2%	4.7%	6.2%	8.1%	9.6%	13%	14%
90< et <110	3.3%	4.4%	5.6%	6.8%	8%	7.7%	9.8%
110< et <120	3.2%	3.8%	4.4%	6%	6.2%	6%	7.6%
120< et <130	3.1%	3.6%	4.8%	5.1%	5.5%	7.3%	7.1%
130< et <140	3%	3.9%	4%	4.9%	6%	5.2%	7.2%
140< et <150	3.5%	4%	3.5%	6.1%	4.2%	7.4%	6.9%
150< et <1000	2.7%	3.1%	3.5%	4.2%	4%	3.7%	5.2%

stat uncert	$\not\!\!E_T$						
$N_{trk} = 13$	10 - 20	20 - 30	30 - 40	40 - 50	50 - 60	60 - 70	70 - 1000
25< et <50	3.9%	4%	5.1%	7.6%	10%	14%	23%
50< et <70	2%	2%	2.4%	3.5%	4.9%	7%	8.6%
70< et <90	1.3%	1.2%	1.5%	2.2%	3.4%	5.1%	6%
90< et <110	0.87%	0.91%	1.3%	2%	3.3%	5.4%	5.6%
110< et <120	1%	1.2%	1.8%	2.8%	4.3%	7.2%	7.7%
120< et <130	1.1%	1.3%	1.9%	3%	4.7%	6.7%	7.4%
130< et <140	1.4%	1.5%	2.1%	3.2%	4.8%	6.9%	7.3%
140< et <150	1.6%	1.8%	2.5%	3.5%	5.5%	7.1%	7.4%
150< et <1000	1.2%	1.2%	1.5%	1.9%	2.6%	3.7%	2.8%

Table A.8: TPM $\not\!\!E_T$ and E_T bin contents (top) and relative statistical uncertainty (bottom) for $NT \geq 13$.

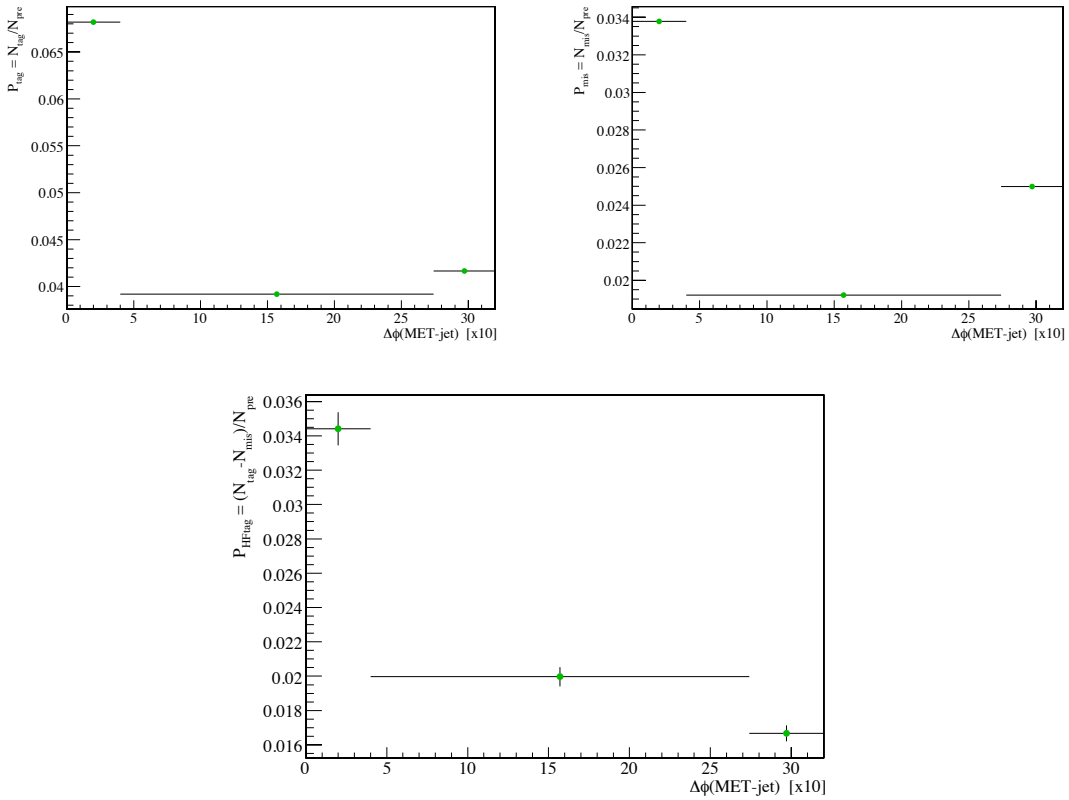

Figure A.1: distributions of the tag rate (top-left), the mistag rate (top-right), and the HF tag probability (bottom) for QCD jets as a function of $\Delta\phi(\not{E}_T - \text{jet})$. Jets with $\Delta\phi(\not{E}_T - \text{jet}) < 0.4$ have a systematically higher HF tag probability than those with $\Delta\phi(\not{E}_T - \text{jet}) > 0.4$. There is a small difference between jets with $\Delta\phi \in [0.4, \pi - 0.4]$ and jets with $\Delta\phi \in [\pi - 0.4, \pi]$. The systematic effect of including the latter in the QCD HF estimation is $\sim 10\%$ (see Section 4.6).

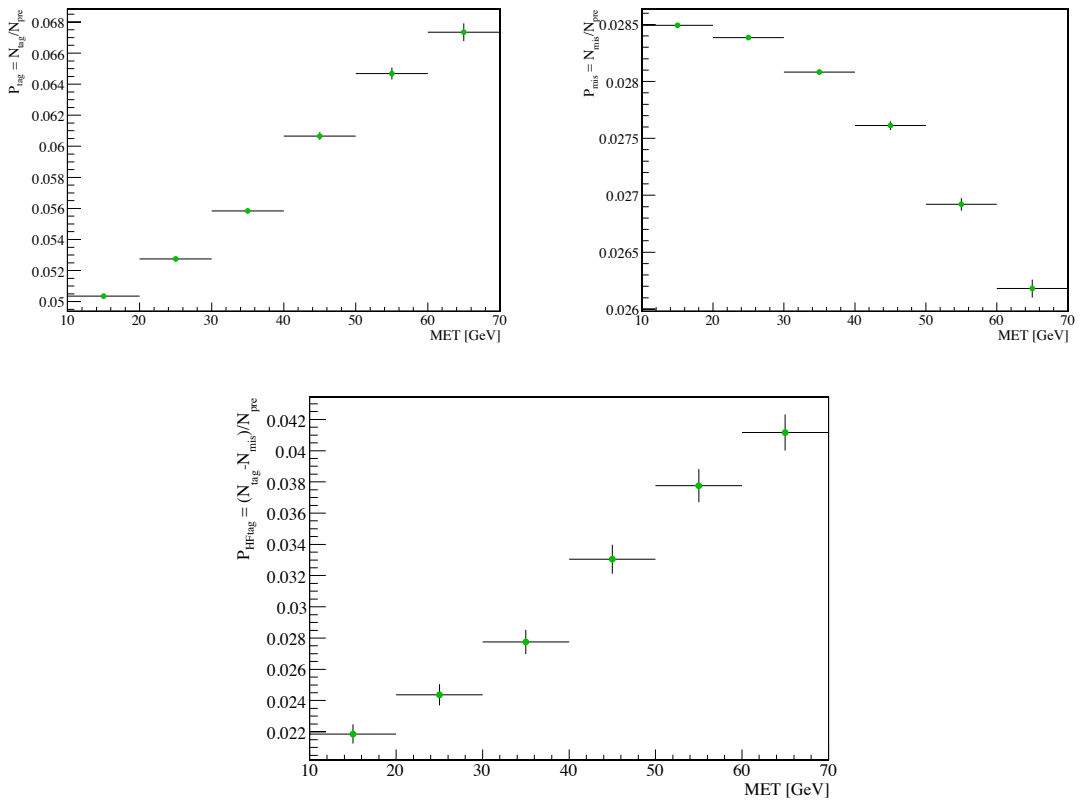

Figure A.2: distributions of the tag rate (top-left), the mistag rate (top-right), and the HF tag probability (bottom) for QCD jets as a function of $\not\!\!E_T$. Events are selected according to the cuts described in Section 4.6.

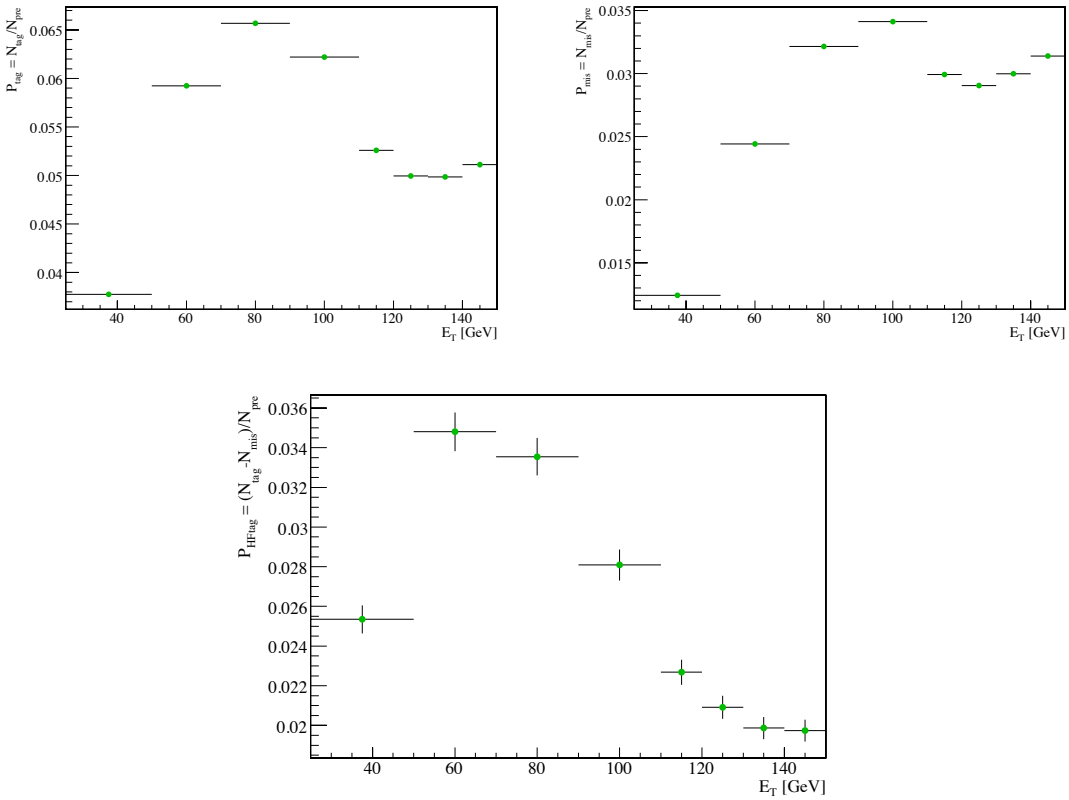

Figure A.3: distributions of the tag rate (top-left), the mistag rate (top-right), and the HF tag probability (bottom) for QCD jets as a function of E_T. Events are selected according to the cuts described in Section 4.6.

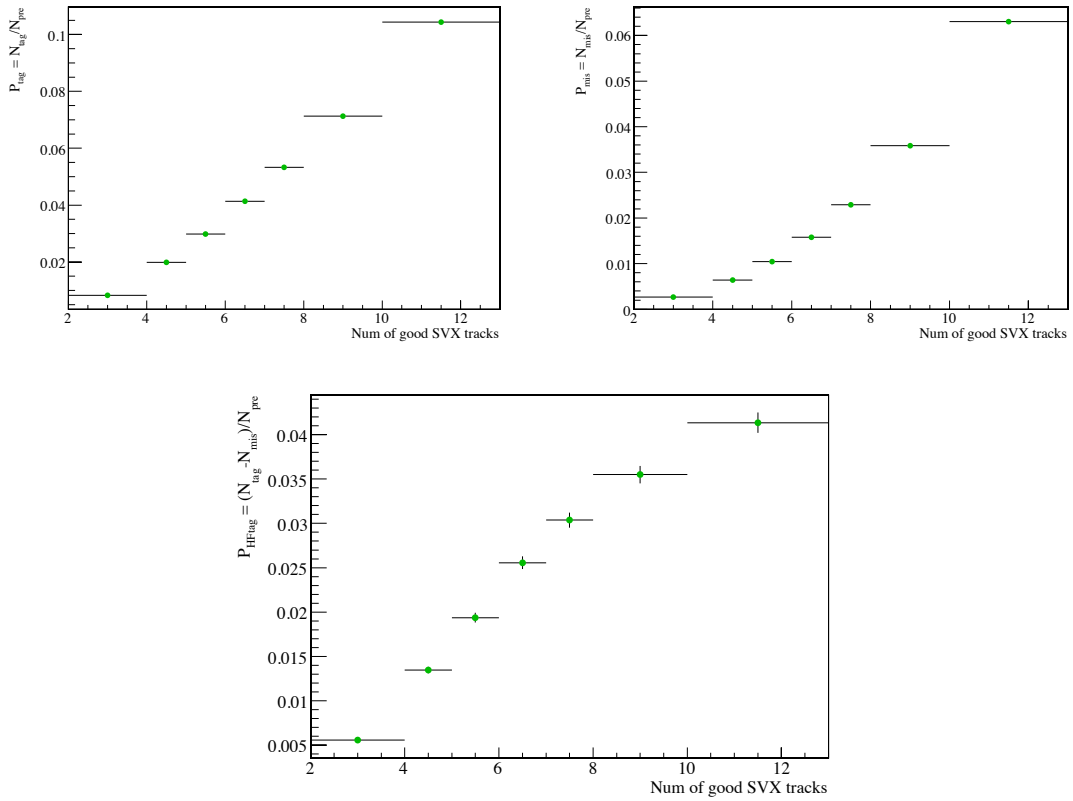

Figure A.4: distributions of the tag rate (top-left), the mistag rate (top-right), and the HF tag probability (bottom) for QCD jets as a function of N_{trk}. Events are selected according to the cuts described in Section 4.6.

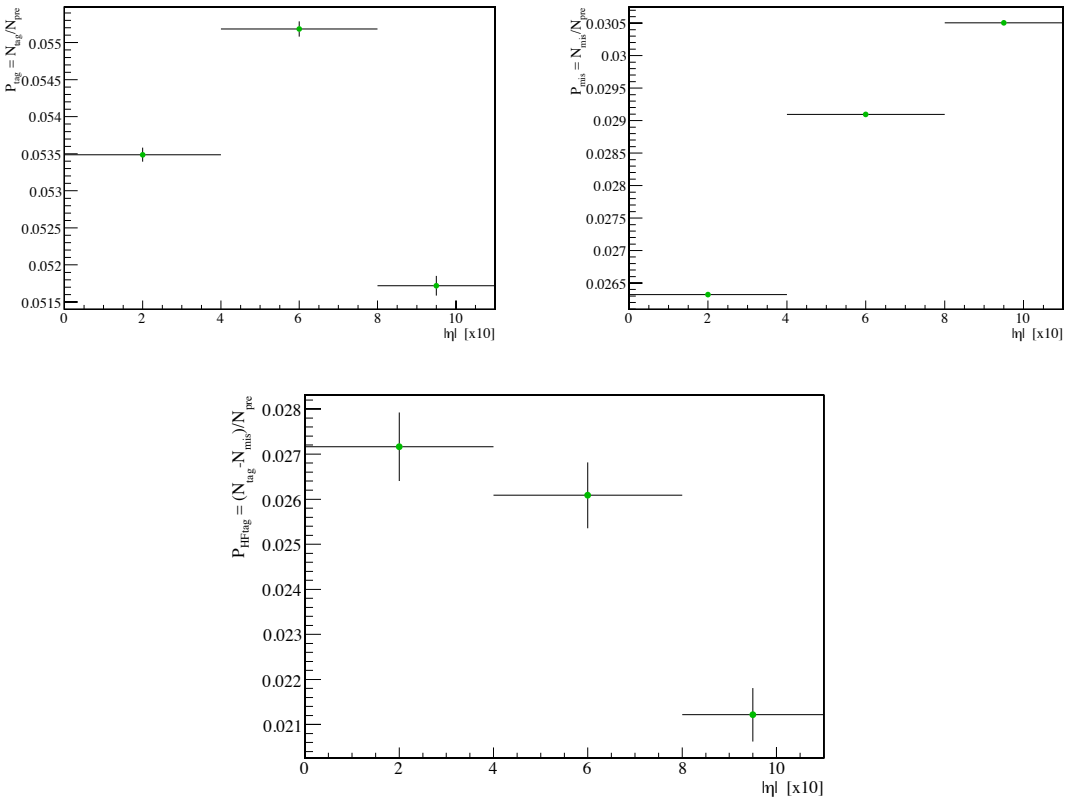

Figure A.5: distributions of the tag rate (top-left), the mistag rate (top-right) and the HF tag probability (bottom) for QCD jets as a function of $|\eta|$. Events are selected according to the cuts described in Section 4.6.

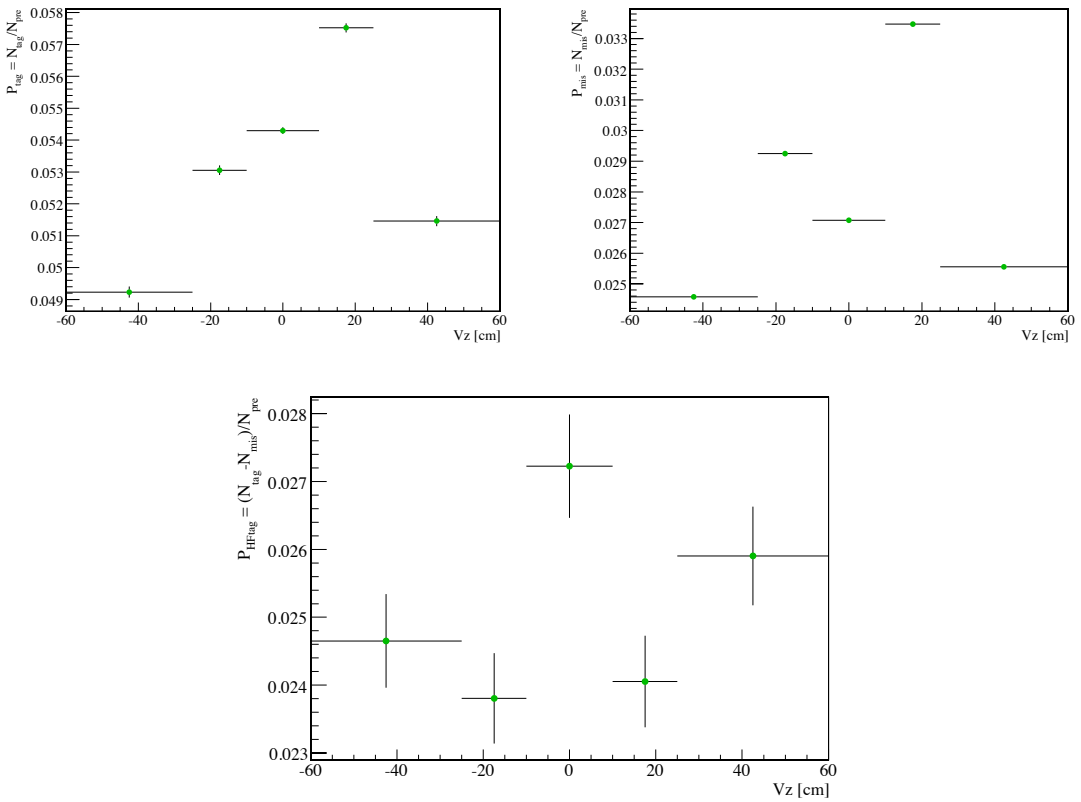

Figure A.6: distributions of the tag rate (top-left), the mistag rate (top-right), and the HF tag probability (bottom) for QCD jets as a function of V_Z. Events are selected according to the cuts described in Section 4.6.

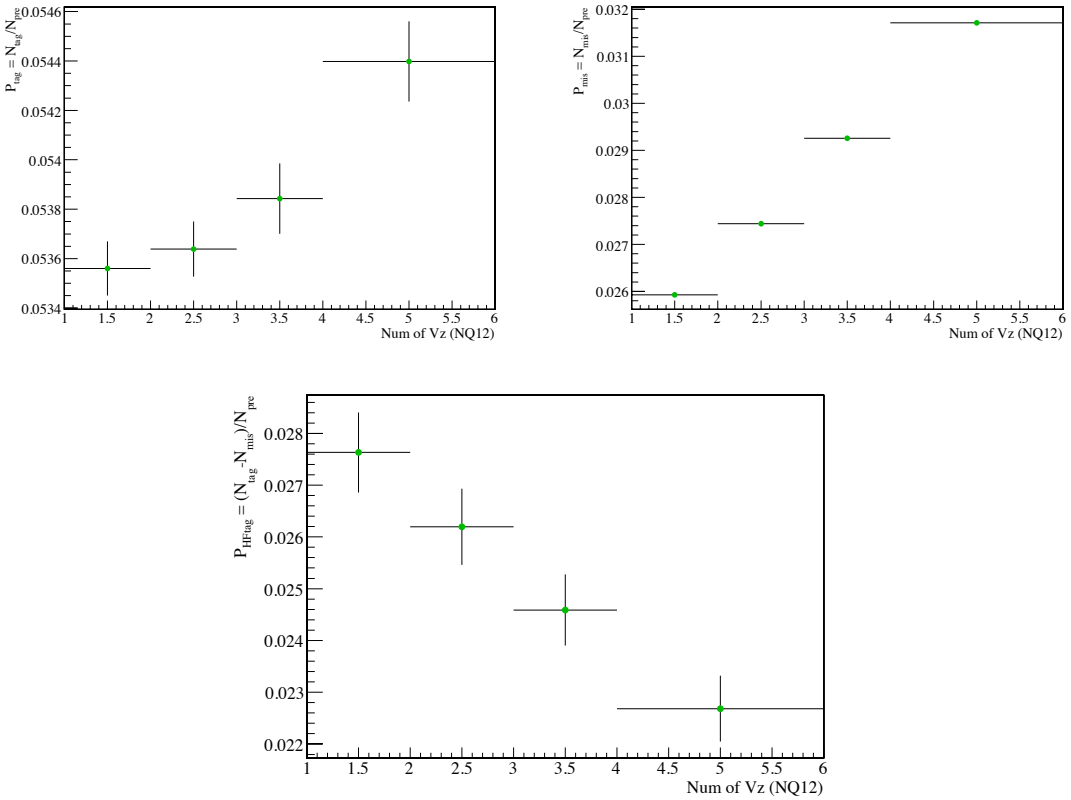

Figure A.7: distributions of the tag rate (top-left), the mistag rate (top-right) and the HF tag probability (bottom) for QCD jets as a function of N_{Vz}. Events are selected according to the cuts described in Section 4.6.

Appendix B

Bayesian Approach to the Calculation of the Limit

In a counting experiment the Poisson probability of observing n events with an expected background b and a signal acceptance ϵ is:

$$\frac{e^{-(\mathcal{L}s\epsilon+b)}(s\epsilon+b)^n}{n!}\,, \tag{B.1}$$

where $\mathcal{L}$ is the integrated luminosity and s the signal cross section. In the Bayesian approach, a prior function need to be defined. Assuming a flat function $\pi(s) = 1$ for $s \geq 0$ and $\pi(s) = 0$ for $s < 0$, the upper limit s_u at confidence level (CL) β is computed, in a finite Bayesian prior-ensemble approximation, by solving:

$$I(s_u) = (1-\beta)I(0)\,, \tag{B.2}$$

where $I(s_0)$ is the integral:

$$I(0) = \frac{1}{M}\sum_{i=1}^{M}\left[\int_{s_0}^{\infty}\frac{e^{-(\mathcal{L}s\epsilon+b)}(\mathcal{L}s\epsilon+b)^n}{n!}ds\right]\,, \tag{B.3}$$

with M being the number of random pairs of ϵ and b events in this finite approach.

This procedure is used to calculate the limit in the two analysis described in this thesis and it is described, together with the program that implements it, in the note [80]. This program allows the use of correlated and uncorrelated uncertainties into the limit calculation process as well as a choice from different random generators. Due to the fact that, in the case of mSUGRA and MSSM signals, the theoretical uncertainties on the cross sections can be very large (up to 30%), a gamma function is chosen as a random generator in order to avoid non-converging integrals.

A Poissonian fluctuation is used to calculate the expected cross section using the following formula:

$$\sigma_{exp} = \sum P(n^i_{obs}|n_{exp}) * \sigma^i_{obs}\,, \tag{B.4}$$

where σ_{obs} is the cross section upper limit with the number of observed events, n_{obs}, $P(n^i_{obs}|n_{exp})$ is the Poisson probability of observing n_{obs} events when the mean value is the number of expected background events, n_{exp}, and the sum is over all the possible values that give a

significant contribution to this Poisson fluctuation. In any case, for numbers larger or similar to 10, it is a good approximation to use $n_{obs} = n_{exp}$, instead.